THE FLORIDA STATE UNIVERSITY

COLLEGE OF ARTS AND SCIENCES

EQUATORIAL PACIFIC OCEAN VARIABILITY--
SEASONAL AND EL NIÑO TIME SCALES

by

John C. Kindle

A Dissertation submitted to the
Department of Oceanography
in partial fulfillment of the
requirements for the degree of
Doctor of Philosophy

Approved:

James J. O'Brien
Professor Directing Dissertation

David Lopez

W. Sturges

W. Sturges
Chairman, Department of Oceanography

December, 1979

ABSTRACT

A nonlinear, single-layer numerical model is used to examine the baroclinic response of the equatorial ocean to time-variable winds. The rectangular model basin extends 1,500 km south of the equator and 15,000 km zonally; open boundary conditions are employed at the southern boundary. Attention is focused on the equatorially trapped wave response to symmetric, zonal time-dependent winds. The effects of mean currents, topography, coastline variation, thermodynamics and thermohaline mixing are neglected.

In order to interpret the numerical solutions, analytic expressions for the vertical motion of the model pycnocline along the equator are derived from the linear theory of equatorial waves. Two types of wind distribution are considered: 1) a uniform wind across the entire basin and 2) a longitudinally bounded patch of wind stress within which the wind is uniform. The numerical model is used to determine some of the parameters of the analytic expressions. For problems whose linear solutions are well known, the results given by the numerical model, linear theory, and the derived analytical expressions agree very closely. The analytical expressions are also used to examine the general linear response of the equatorial ocean to time-variable winds as a function of the period of the forcing, the basin length and the stratification.

the period of the forcing, the basin length and the stratification.

Both the numerical model and the analytical expressions are utilized to examine the suggestion of Meyers that remote forcing may be responsible for the large semi-annual signal of the vertical displacement of the thermocline in the eastern equatorial Pacific Ocean. Using Meyers' computations of the long term mean and seasonal winds along the equator, the numerical model reproduces the observations of the average seasonal vertical displacement of the pycnocline at the eastern boundary. The analytical expressions reveal that equatorially trapped Kelvin waves excited between 180° and 120°W are responsible for the large semi-annual response at the eastern boundary of the model.

Numerical simulations of the anomalous El Niño event are performed by initializing the model at some stage of the average seasonal solution and, subsequently, modifying the mean winds in the central and western Pacific. The seasonal winds remain unmodified throughout the basin as well as the mean winds in the eastern half of the model ocean. Since the model runs are made over periods of years, such features as the intensification of winds prior to El Niño, the relaxation phase and the subsequent return to normal conditions are included. Discussion is focused on the effects of the magnitude, duration and timing of both the relaxation and the subsequent intensification phases. In addition to a realistic representation of the onset of El Niño, the numerical simulation is able to account for such observed features as the slow decline of sea level in the western Pacific during El Niño, the rapid recovery of the height field in the western Pacific, the occasional appearance of El Niño events in consecutive years and the rapid end to El Niño conditions
height field in the western Pacific, the occasional appearance of El Niño events in consecutive years and the rapid end to El Niño conditions

in the eastern Pacific. The occurrence of El Niño-like conditions at the eastern boundary in the year following major El Niño events is related to the duration of the anomalously weak winds in the central and western Pacific Ocean.

ACKNOWLEDGEMENTS

This work was supported by the Office of Naval Research, Ocean Science and Technology Branch, under contract N000-14-75-C0201. Partial support was provided by the International Decade of Ocean Exploration (IDOE) through the Coastal Upwelling Ecosystems Analysis (CUEA) program under Grant No. OCE78-00611. Computations were performed on the CDC Cyber 74 at Florida State University, Tallahassee, Florida.

I wish to express my gratitude to Dr. James J. O'Brien for serving as my major professor and for his encouragement, support and helpful suggestions during the course of this research. I would also like to acknowledge Drs. Ya Hsueh, Richard Iverson, David Loper and Raymond Staley for serving on my doctoral committee.

To Dr. Nobuo Suginohara I wish to express my appreciation for his review of the manuscript and for many hours of stimulating discussions. Also, I wish to thank Mr. Monty Peffley whose help was vital to the solution of many computer-system problems. The assistance rendered by Mr. Tony Busalacchi is also much appreciated.

I would like to acknowledge the assistance of Ms. Noreen O'Malley, Mrs. Sheila O'Brien and Mr. Dewey Rudd. All the draft copies and the final version of the dissertation were typed by Susan Finney to whom I am very grateful.

am very grateful.

TABLE OF CONTENTS

Table of Contents -- Continued

LIST OF TABLES

LIST OF ILLUSTRATIONS

out of the numerical solution. 35

ix

List of Illustrations -- Continued

Figure | Page

List of Illustrations -- Continued

abscissa designate the mid-points of months. The plot begins in mid-December. Positive values in (b) indicate upwelling. (Data from Meyers, 1979b). 73

List of Illustrations -- Continued

List of Illustrations -- Continued

Figure Page

ULT from long-term seasonal value durings years 4 and 5 of Case 2. The dashed line in (a) is the average seasonal solution. The relaxation of the wind is similar to Case 1 except that the time scale for the relaxation is one month. The mean

List of Illustrations -- Continued

1. INTRODUCTION

The variability of the equatorial Pacific circulation has been linked to climate anomalies throughout the tropics and higher latitude regions (e.g., Bjerknes, 1961, 1966a, 1966b, 1969, 1972; Ichiye and Peterson, 1963; Quinn and Burt, 1970; Namias, 1976; and Julian and Chervin, 1978). The most dramatic abnormal phenomena are the El Niño events during which anomalously warm surface water often extends from the Peruvian and Ecuadorian coasts to thousands of kilometers from the eastern boundary along the equator. Wyrtki (1975b) hypothesizes that the occurrence of El Niño is related to the sudden relaxation of the equatorial Trade Winds in the Central and western Pacific subsequent to a period of abnormally strong winds in that region. Wyrtki's hypothesis received theoretical support from the modelling of Hurlburt, et al., (1976) and McCreary (1976, 1977). In his analysis of the tropical Pacific circulation, Wyrtki (1973) found high correlations between El Niño events and anomalous sea level differences across the major equatorial surface currents. It is evident that the baroclinic structure of virtually the entire equatorial Pacific experiences drastic changes during El Niño. An understanding of the dynamics of such anomalous events, however, will require an understanding of the variability associated with the seasonal cycle as well. It is the purpose of this paper to explore certain aspects of both El Niño and the equatorial seasonal circulation.

to explore certain aspects of both El Niño and the equatorial seasonal circulation.

Wyrtki (1974) has provided an excellent description of the seasonal variation of the equatorial current system in the western and central Pacific. Using sea-level data over a twenty-year period at eleven equatorial stations, Wyrtki showed that the strength of the South Equatorial Current situated south of the equator tended to vary in phase with the Equatorial Undercurrent, but out of phase with both the North Equatorial Current and the North Equatorial Countercurrent. The Countercurrent is generally weakest in the spring and strongest in the fall. For a general description of the equatorial current system, see Knauss (1964).

There are no long period data records of the circulation in the eastern tropical Pacific; this is due, primarily, to the scarcity of islands in that region. Tsuchiya (1974) has examined the surface geopotential anomaly field from the EASTROPAC expedition (February 1976 to April 1968). He, too, found that the Countercurrent was weak in the spring but very strong in the fall. One of his discoveries was an observed eastern current very near the equator during the April-May period. Tsuchiya offers evidence disputing the usual interpretation of this current as the surfacing of the Undercurrent (Taft and Jones, 1974).

Both Meyers (1975) and Wyrtki, et al. (1977) have related the seasonal variation of the equatorial currents to the seasonal changes of the thermal structure in the tropical Pacific. Both studies found that vertical displacements of the thermocline account for most of the variability of the thermal structure. Attempts to explain the seasonal motion of the tropical thermocline have been only partially successful. White (1977) attempted to explain the vertical variability of the thermocline between 10°-20°W as a combination of the forced Ekman pumping

response and a free Rossby wave with an annual period. Meyers (1979a), however, shows that such a theory is not totally consistent with observations along 10°N because, in regions other than those considered by White, the data are not consistent with White's theory. Meyers finds that the free Rossby wave plays only a minor role in the vertical motion of the thermocline at 10°N but a major role at 6°N.

Efforts to explain the vertical motion of the thermocline at the equator have proven fruitless. The model of Dewitt and Leetma (1978), which is frictionally controlled at the equator, was able to simulate the observed seasonal motion of the eastern Pacific equatorial thermocline during only part of the year, but an extremely large value of vertical eddy viscosity was required to achieve this result. Meyers (1979a) also examined the seasonal motion of the equatorial thermocline by including the effects of geostrophic divergence and by using the model of Gill (1975) to estimate the vertical velocity due to Ekman pumping at the equator. The resultant analysis could not explain the seasonal vertical motion of the thermocline along the equator. The most probable cause of the inability of these works to succeed at the equator is that the effects of remote forcing were not properly included. In fact, Meyers (1979b) suggests that the semi-annual signal of the thermocline motion in the eastern equatorial Pacific is remotely forced. The dynamics governing the narrow latitudinal band in which equatorial upwelling occurs (3°S-3°N) constitute a unique physical system. The presence of equatorially trapped waves can provide a very efficient mechanism for the zonal propagation of energy along the equator. If the equator is an equatorially trapped waves can provide a very efficient mechanism for the zonal propagation of energy along the equator. If the equator is an efficient waveguide at seasonal time scales, then the effects of remote

forcing will have to be included accurately in order to account for the seasonal variability of the thermal structure in the near-equatorial regions.

Although the analytical framework for the equatorial response to time-variable winds was established by Moore (1968), most theoretical equatorial studies have focused on the transient response to suddenly imposed steady winds. Such features as the equatorial jet (Yoshida, 1959; O'Brien and Hurlburt, 1974), the Somali Current (Lighthill, 1969; Anderson and Rowlands, 1976a; Cox, 1976; Hurlburt and Thompson, 1976), El Nino (Hurlburt et al., 1976; McCreary, 1976, 1977), the Equatorial Undercurrent (Gill, 1975; McKee, 1973), the equatorial current system (Cane, 1979; Semtner and Holland, 1979; Cane and Sarachik, 1976, 1977, 1979), and the Gulf of Guinea Upwelling (Moore et al., 1978; Adamec and O'Brien, 1978) have been modelled as the transient response to a steady wind. In addition to simplifying the analytical development, the imposition of impulsive steady forcing allows an easier interpretation of the solutions in terms of the interior and boundary responses.

A notable exception to the above approaches in modelling the time-dependent equatorial ocean is that of Wunsch (1977), who examined the equatorial response to forcing with an annual period. In order to model the observations with high vertical structure found by Luyten and Swallow (1976) in the Indian Ocean, he examined the forced wave response. Since his model assumes that energy propagates vertically in only one direction, Wunsch's approach is equivalent to that used by meteorologists (Holton, 1975). Such an approach focuses on the vertical structure of a tion, Wunsch's approach is equivalent to that used by meteorologists (Holton, 1975). Such an approach focuses on the vertical structure of a particular x-y-t mode determined by the forcing rather than on the x-y-t

structure of a particular vertical mode. Wunsch is able to generate very tightly trapped Rossby waves with the correct vertical scale. A comparison of the two different approaches is given by Philander (1978).

This paper will focus on the effects of equatorially trapped waves pertinent to a single vertical mode and initiated by symmetric zonal winds which have time scales varying from a few months to several years. In Section 2 a nonlinear, reduced-gravity numerical model with a basin size corresponding to the tropical Pacific Ocean, is described. In order to integrate the model over periods of years, an open boundary condition, which permits the passage of coastal Kelvin waves and Rossby waves is applied at the southern boundary. Symmetry is used at the northern boundary which is located at the equator.

In order to interpret and understand better the numerical results, analytical expressions are derived in Section 3 for the vertical motion of the model pycnocline along the equator. These expressions, which are based on the linear theory of equatorial waves, are derived for two types of wind-stress distributions: 1) a wind which is uniform across the basin, and 2) a wind stress patch which has a rectangular pulse shape in the zonal direction and a uniform distribution in the meridional direction. In addition to delineating the effects of individual waves and their reflections, the analytical expressions are used in Part 4 to examine the fundamental properties of the periodic equatorial response as a function of the period of the forcing, the length of the basin and the stratification.

In Section 5, both the numerical model and the analytical expres-

stratification.

In Section 5, both the numerical model and the analytical expressions are used to examine the climatic seasonal variability of the equa-

torial Pacific. The forcing for these studies are the annual and semi-annual components of the mean monthly zonal equatorial winds as analyzed by Meyers (1979b). It is shown that the semi-annual component of the mean monthly vertical displacement of the thermocline at the eastern boundary is due to the excitation and subsequent propagation of equatorial Kelvin waves originating between 180° and 120°W. This supports Meyer's hypothesis (1979b) that remote forcing may be responsible for the large semi-annual signal of the thermocline displacement in the eastern equatorial Pacific.

Finally, in Section 6, numerical simulations of El Niño are performed which combine the effects of seasonal variability and the large scale changes of the wind stress in the central and western Pacific. The model is initialized at a particular point in the seasonal cycle; subsequent numerical integrations run for several years. The seasonal wind components remain unchanged throughout the basin as do the mean winds in the eastern half of the model ocean. The mean winds in the western half are modified so as to represent such features as the intensification of Trade Winds prior to El Niño, the sudden relaxation of these winds and the subsequent return to normal conditions. This allows us to investigate the longer time scale aspects of El Niño which were reported by Wyrtki (1977, 1979); it was observed that in both the 1972 and 1976 El Niño events, the initial rapid onset at the eastern boundary was followed by a year-long decline of sea level in the western Pacific and a subsequent rapid return to normal conditions near the end of that year. In addition, some major El Niño events exhibit consecutive peaks and a subsequent rapid return to normal conditions near the end of that year. In addition, some major El Niño events exhibit consecutive peaks in sea level in the eastern boundary regions separated by about a year.

This was true of the 1957-58 and 1972-73 El Niño occurrences, but not of the 1976 event. These longer time scale aspects of El Niño have not been examined theoretically. The numerical simulations described in this paper reproduce the essential features of the observations described above. Dynamical scenarios for the fundamental behavior of the equatorial Pacific Ocean during El Niño are presented and discussed.

2. THE NUMERICAL MODEL

The enormous size of the Pacific Ocean presents a formidable obstacle to the numerical modelling of its time-dependent circulation. Adequate resolution of the narrow currents and waves trapped along the boundaries and the equator requires fine horizontal grid spacing in regions which comprise an extremely small percentage of the basin's total area. In order to examine effectively the feature(s) of interest, substantial compromises may have to be made in the choice of such parameters as the dimensions of the model basin, the horizontal resolution, the length of the time integrations and the vertical resolution. Since we will 1) examine the dynamics of equatorial and coastal regions on the scale of the internal radius of deformation, 2) perform a variety of numerical experiments over time scales of years, and 3) use a basin whose dimensions approximate the true size of the tropical Pacific Ocean, the logical choice for the model equations are those given by a single layer, reduced-gravity model. Such a model represents the baroclinic mode of a two-layer system in which the ocean is assumed to be hydrostatic, incompressible and consists of two homogeneous layers of different density. The interface between the two layers represents the main pycnocline, which in the equatorial regions is very strong and shallow. The reduced-gravity model also assumes that the horizontal pressure gradient in the lower layer is so small that the layer is motionless. This is consistent with the representation of the first baroclinic mode by a

in the lower layer is so small that the layer is motionless. This is consistent with the representation of the first baroclinic mode by a

two-layer system in which the upper layer thickness is much smaller than the total depth. (For an extensive discussion on the relationship between two-layer reduced-gravity models and single-mode models, see McCreary (1977).) The validity of a two-layer approximation for the baroclinic structure in the central equatorial Pacific has been pointed out by Wyrtki, et al. (1977). Examples of the recent use of reduced-gravity models to study the equatorial circulation are McCreary (1977), Lin and Hurlburt (1978), Adamec and O'Brien (1978) and Cane (1979).

The advantages of immobilizing the lower layer of a two-layer model are 1) the elimination of the barotropic mode and 2) the simplification of the model equations. The resultant governing equations for the system are the nonlinear shallow water wave equations on an equatorial beta-plane,

$$
\begin{aligned}
u_t + uv_x + vu_y - \beta yv &= -g'h_x + A\nabla_h^2 u + \frac{\tau^x}{\rho_1(H+h')} \\
v_t + uv_x + vv_y + \beta yu &= -g'h_y + A\nabla_h^2 v + \frac{\tau^y}{\rho_1(H+h')} \qquad (1) \\
h_t + (hu)_x + (hv)_y &= 0
\end{aligned}
$$

where u and v are the upper layer velocity components, g' is the reduced gravity given by $g(\rho_2 - \rho_1)/\rho_1$, h is the thickness of the upper layer and h' is the pycnocline height anomaly (PHA), i.e., the departure of the upper layer thickness from its initial uniform thickness, H. A complete list of parameters and symbols is given in the appendix. The Cartesian coordinate system is righthanded with positive x directed eastward, and its origin is the western boundary of the model equator. The wind stress, whose components are (τ^x, τ^y), is included as a body force

distributed uniformly throughout the upper layer. The effects of thermohaline mixing and thermodynamics are neglected.

The set of equations (1) are solved in a rectangular basin as shown in Fig. 1. The eastern and southern boundaries are at 80°W and 15°S, respectively. The northern boundary for the computations is the equator; because only symmetric zonal winds are applied, the solution in the northern hemisphere is simply the mirror image of the solution south of the equator. The western boundary is at 162°E (13,000 km from the eastern boundary) in Sections 2 and 3. In order to incorporate wind-stress measurements throughout the entire equatorial Pacific, the basin is extended to 144°E for the computations in Section 5 and 6.

Boundary conditions at the eastern and western walls are no slip. Symmetry is applied at the equator. The southern boundary is open, and a variant of the boundary condition developed by Hurlburt (1974) is used there. The boundary condition yields an expression for the north-south pressure gradient at an open zonal boundary. All other meridional derivatives are set to zero except for the flux terms in the continuity equation. In the two-layer model of El Nino used by Hurlburt, et al. (1976), this condition was applied very successfully as a means to let coastal Kelvin waves and Rossby waves pass through the boundary, thereby preventing these waves from eventually interfering with solutions at the equator. The reduced-gravity version of this boundary condition is given by the simple relation:

$$h_y = (h/_x - h/_{x=0})/L_y \qquad (2)$$

$$h_y = (h/_x - h/_{x=0})/L_y \qquad (2)$$

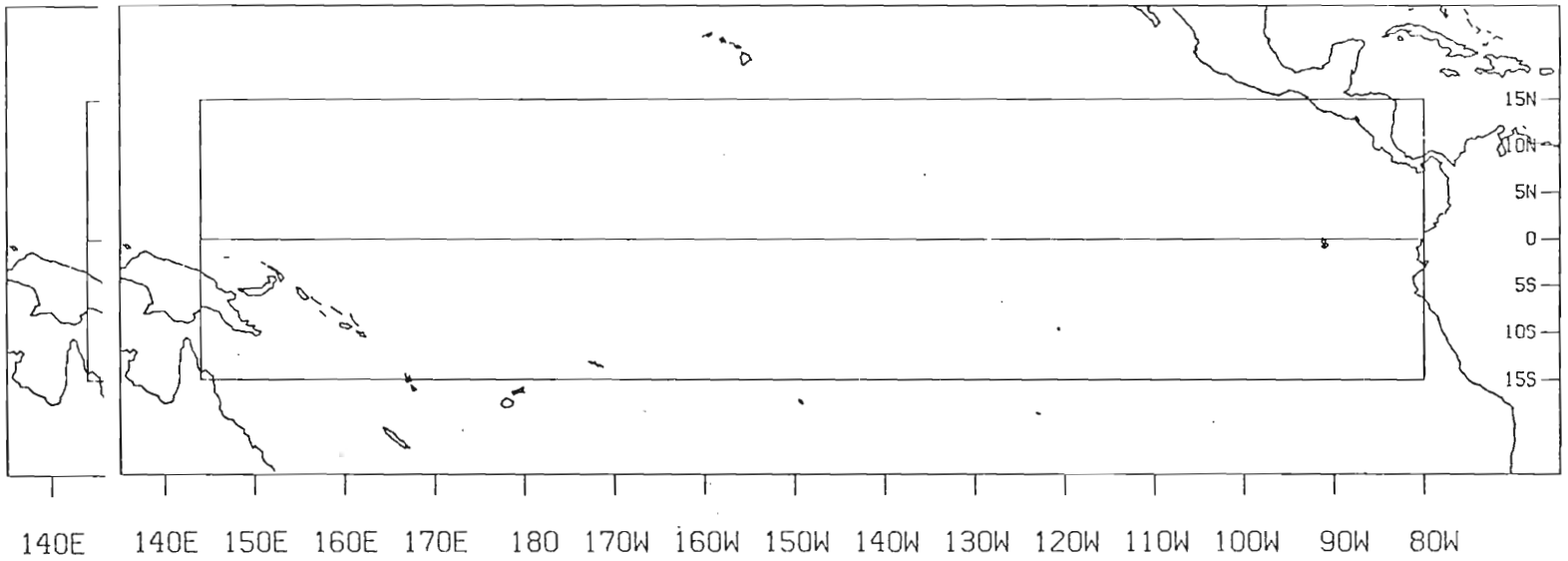

Fi Fig. 1. Comparison of model geometry in relation to tropical Pacific Ocean. The model basin ebasin extends 15,000 km zonally and ± 1,500 km meridionally. The zonal boundaries are open; the merthe meridional boundaries are solid walls.

where L_y is the distance from the boundary to the equator. The N-S pressure gradient at the S-W corner of the basin has been set to zero. Although, for time integrations greater than approximately six months, some smoothing at the boundary was required to control the build-up of "noise", the boundary condition did indeed permit the passage of incident waves with no noticeable reflection.

In order to minimize core storage requirements, the model equations are solved on a staggered grid whose spacing in the x-direction is variable. The stencil for the grid is shown in Fig. 2. The values of Δx, which change in discrete steps, vary from 20 km near the eastern and western boundaries to 150 km in the interior; the meridional grid spacing, Δy, is uniformly 25 km.

The model equations are treated explicitly using leap-frog for the time derivatives and centered-differencing for the spacial derivatives; the viscous terms, however, are lagged in time. The nonlinear advective terms are quadratic-averaged, using a slight variant of Scheme F from Grammeltvedt (1969). Unless otherwise stated, the model is started from rest using a forward time step.

In order to examine the most fundamental equatorial response to time-variable winds, the effects of bottom topography and realistic coastline configuration have been neglected. Although these features may exert a major influence on the processes discussed in this paper, our study will focus on the Pacific Ocean where such features appear to play a secondary or minimal role. There is no large scale ridge in the equatorial Pacific which seems capable of substantially altering the

play a secondary or minimal role. There is no large scale ridge in the equatorial Pacific which seems capable of substantially altering the

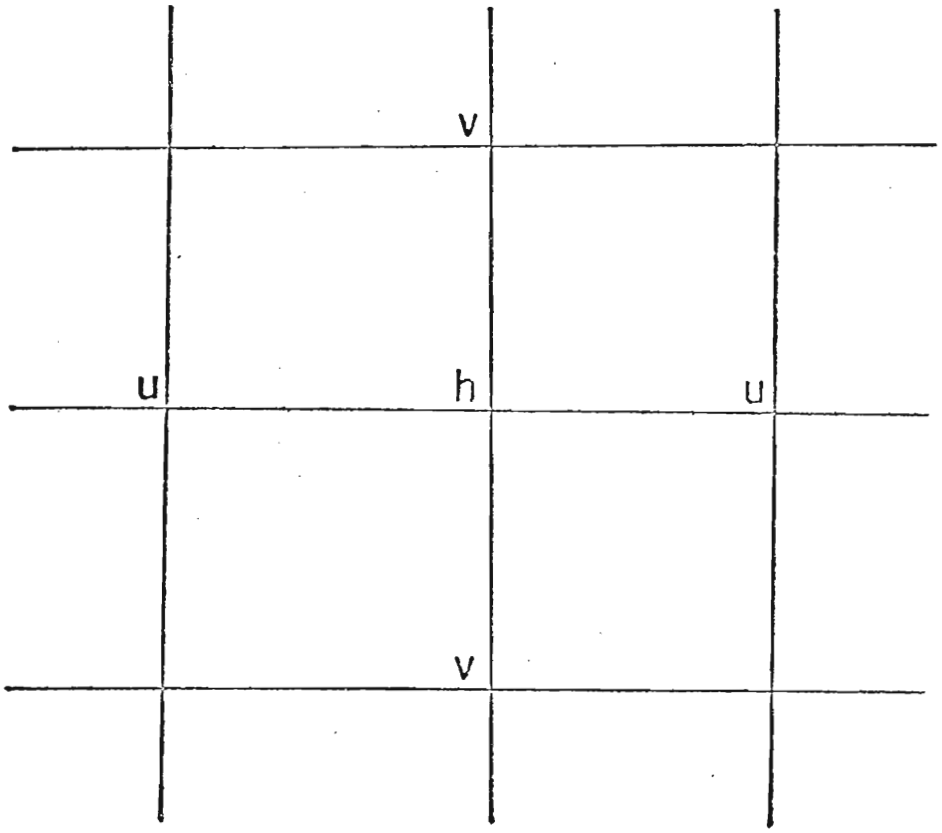

Fig. 2. Stencil for the staggered grid used in the computations. The zonal component of velocity is evaluated at the meridional boundaries; all three dependent variables are evaluated at the open boundary.

equatorially trapped, internal-wave processes derived for an ocean with a flat bottom. The effects on the equatorial waves of such ridges in the Atlantic and Indian Oceans are yet to be studied.

3. THE ANALYTICAL MODEL

In order to interpret and understand the numerical model solutions, linear theory will be used as a guide. Although the analytical framework for the equatorial response to time-variable winds has been established by Moore (1968), most theoretical studies have focused on the transient response to steady winds. In this section, general expressions for the vertical motion of the model pycnocline along the equator are derived for the case of zonal time-variable winds. Two types of wind-stress distribution are considered: 1) a wind which is uniform across the basin and 2) a wind-stress patch of arbitrary width which has a rectangular pulse distribution in the zonal direction. The expressions will include such features as the longitudinally unbounded interior response, the excitation of equatorially trapped waves and the reflections of these waves at the eastern and western boundaries.

a. Equatorial Waves

The details of equatorial wave dynamics have been reviewed extensively by Moore and Philander (1977), Philander (1978) and Beer (1978). It will suffice here to examine only the major properties of low-frequency equatorially trapped waves.

The linear, inviscid, hydrostatic, non-divergent system of equations on an equatorial β-plane may be expressed as:

tions on an equatorial β-plane may be expressed as:

$$
\begin{aligned}
u_t - \beta y v &= -P_x/\rho_o \\
v_t + \beta y u &= -P_y/\rho_o \\
P_z &= -g\rho \qquad (3) \\
u_x + v_y + w_z &= 0 \\
\rho_t + w\bar{\rho}_z &= 0
\end{aligned}
$$

where $\bar{\rho}_z$ is the mean density gradient in the vertical direction. A right-handed Cartesian coordinate system in which x is positive eastward is employed. The effects of bottom topography, horizontal variation of density and mean flow are ignored. If we follow the formulation of Gill and Clarke (1974) by expanding in terms of the vertical modes of the system, i.e.

$$
\begin{Bmatrix} u(x,y,x,t) \\ v(x,y,z,t) \\ P(x,y,z,t)/\rho_o \end{Bmatrix} = \sum_{n=1}^{\infty} \begin{Bmatrix} U_n(x,y,t) \\ V_n(x,y,t) \\ P_n(x,y,t) \end{Bmatrix} S_n(z)
$$

$$
\begin{Bmatrix} w(x,y,z,t) \\ \dfrac{g\rho(x,y,z,t)}{N^2(z)} \end{Bmatrix} = \sum_{n=1}^{\infty} \begin{Bmatrix} W_n(x,y,t) \\ h_n(x,y,t) \end{Bmatrix} F_n(z)
$$

then the equations for the vertical eigenfunctions are

$$
\frac{d^2F_n}{dz^2} + \frac{N^2(z)}{\lambda_n^2} F_n = 0 \qquad (4)
$$

$$
S_n = \frac{dF_n}{dz} \qquad (5)
$$

The resultant system of equations for the amplitudes of the eigenfunc-

$$
\frac{dF_n}{dz} \qquad (5)
$$

The resultant system of equations for the amplitudes of the eigenfunction expansions is given by

$$U_t - \beta y V = P_x$$

$$V_t + \beta y U = P_y \qquad (6)$$

$$P_t + \lambda_n^2 (U_x + V_y) = 0$$

$$\rho_t = \lambda_n^2 W \qquad (7)$$

where U, V, P, and W are amplitudes of an eigenfunction expansion in terms of $F_n(z)$ or $S_n(z)$, λ_n^2 is the eigenvalue determined from the vertical structure equations (4), and $N^2(z)$ is the Brunt-Vaisala frequency. The eigenvalue, λ_n^2, is the square of the gravity wave speed and is frequently expressed in the form $\lambda_n^2 = gH_n$, where H_n is the equivalent depth of a particular vertical mode.

The linear inviscid form of the reduced-gravity equations, (1) may be viewed as the system of equations describing the horizontal and temporal dependence of a particular baroclinic mode (6). In such a case, the equivalent depth is determined by the specification of the stratification and the upper layer depth, i.e., $H_n = (\Delta\rho/\rho_o)H$. For the equatorial oceans, the equivalent depth for the first baroclinic mode is O(50 cm) (Moore and Philander (1977)).

The system (6) is solved most easily in terms of the meridional velocity. The resulting equation is

$$V_{ttt} + \beta^2 y^2 V_t - \lambda_n^2 (\beta V_x + \nabla^2 V_t) = G_n(x, y, t) \qquad (8)$$

where G_n is the amplitude of the forcing for a given baroclinic mode. If a waveform dependence in the zonal direction is assumed, i.e., $e^{i(kx - \omega t)}$, then (8) reduces to:

If a waveform dependence in the zonal direction is assumed, i.e., $e^{i(kx - \omega t)}$, then (8) reduces to:

$$V_{yy} + \left(\frac{\omega^2}{\lambda_n^2} - \frac{\beta k}{\omega} - k^2 - \frac{\beta^2 y^2}{\lambda_n^2}\right)V = G(y) \qquad (9)$$

The solution to (9) may be expressed in terms of Parabolic-cylinder functions (Beer, 1978). However, Matsuno (1966) was the first to realize that if V is bounded as $y \to \pm \infty$, then the homogeneous solution may be written in terms of Hermite functions and the following dispersion relation is obtained:

$$\frac{\omega^2}{\lambda_n^2} - \frac{\beta k}{\omega} - k^2 = \frac{(2m+1)\beta}{\lambda_n} \qquad (10)$$

where m, which designates the particular latitudinal mode, can be any non-negative integer. The normalized Hermite functions are given by the relation:

$$\Psi_m = \frac{\exp(\frac{y^2}{2}(\lambda_n/\beta)^{\frac{1}{2}})H_m}{(\sqrt{\pi}\ 2^m\ m!)^{\frac{1}{2}}} \qquad (11)$$

where H_m is the m^{th} Hermite polynomial. The eigenfunctions for even (odd) m are symmetric (asymmetric) about the equator and have turning points given by

$$y_T = \pm \left[\frac{(2m+1)\lambda_n}{\beta}\right]^{\frac{1}{2}}. \qquad (12)$$

The turning point is the distance from the equator at which the solution changes from oscillatory to exponential in nature. Hence, as m increases, the latitudinal modes become less equatorially trapped.

Equation (10) is a dispersion relation for three types of waves: the high frequency intertia-gravity waves, the low frequency mixed Rossby-gravity wave and Rossby waves. An additional solution to (6) is the equatorial Kelvin wave which is obtained by setting the meridional velocity component identically equal to zero. For a derivation of this wave

see Moore and Philander (1977). The Kelvin wave is non-dispersive with speed λ, propagates from west to east, and is trapped within an equatorial radius of deformation of the equator. The analytic form of the zonal velocity component of the Kelvin wave is given by

$$u = F(k(x - \lambda t))\ \Psi_o \tag{13}$$

where Ψ_o is the zero-th Hermite function. The dispersion diagram for free waves on an equatorial β-plane may be found in numerous references [e.g., Philander (1978), Wunsch and Gill (1976), Cox (1976), Cane and Sarachik (1976)].

At each value of m and ω for which Rossby waves are permitted, there exist two values of wavenumber, k. Although all Rossby waves have phase velocity to the west, the wave with larger k has an eastward group velocity. For long wavelengths and low frequencies, planetary waves are non-dispersive and propagate westward at a speed $\lambda_n/(2m + 1)$. Hence, both planetary and inertia-gravity waves can propagate energy in either the westward or eastward directions.

The mixed Rossby-gravity wave (Yanai Wave)[1], which has its meridional velocity component proportional to Ψ_o, has an eastward directed group velocity, but its phase velocity can be either westward or eastward. Hence, the two most highly trapped waves (Yanai and Kelvin) propagate energy in the same direction.

For given values of λ_n and m, inertia-gravity waves are possible for values of

$$\omega^2 \geq (2m + 1)\beta\lambda_n.$$

---

for values of

$$\omega^2 \geq (2m + 1)\beta\lambda_n.$$

---

[1] Oceanographers have borrowed the name Yanai wave from meteorologists as an alternate designation of the mixed Rossby-gravity wave. The properties of this wave in the atmosphere were first observed and reported by Yanai and Maruyama (1966).

The period of inertial oscillations at the equator, which depends upon the particular vertical and latitudinal mode, is given by

$$T_i = \frac{2\pi}{[(2m + 1)\beta\lambda]^{\frac{1}{2}}}$$

where $m \geq 1$ (Moore and Philander, 1977). For the parameters used in this paper, the longest inertial period is slightly greater than six days.

The reflection properties of free waves on an equatorial β-plane were first examined by Moore (1968), in which he studied the reflected response of an incoming wave at a single frequency. At a western boundary an incoming planetary wave excites shorter scale planetary waves and either a Kelvin or Yanai wave. Each reflected wave has the corresponding symmetry of the incoming wave, and no waves are excited which have a latitudinal mode number greater than the incident wave. At an eastern boundary, however, energy is distributed over a much wider latitudinal range than the incoming Yanai or Kelvin wave. Moore showed that the eastern boundary response can be composed of an infinite series of latitudinal mode planetary waves, and that for large y, this series converges to a coastally trapped Kelvin wave propagating poleward along the eastern boundary. As in the western boundary case, the symmetry of the incident wave is preserved.

In other studies, Anderson and Rowlands (1976b) examined the eastern boundary reflection to an incident Kelvin wave of step function form. Cane and Sarachik (1977) studied the spin-up of an equatorial basin for forcing which is longitudinally independent and switched on at t = 0.

Cane and Sarachik (1977) studied the spin-up of an equatorial basin for forcing which is longitudinally independent and switched on at t = 0.

More recently, Cane and Sarachik (1979) examined the equatorial response to similar forcing in basins which are latitudinally bounded.

The contribution of the various equatorial waves to the quasi-steady solution to periodic forcing is not nearly as easy to discern as is the spin-up due to steady winds. For example, consider two cases both of which are forced by a uniform wind; in the first case the wind is steady and directed from east to west, whereas in the second case it has a period of one year. The above forcing is used to drive the numerical model described in Section 1. The parameters which are used in all cases in this section are given in Table 1. The dimensions of the basin (L_x, L_y) were chosen to approximate the size of the tropical Pacific Ocean. The choices for the remaining important free parameters, $\Delta\rho$ and H, were made with respect to such constraints as approximating the first baroclinic mode, producing a realistic representation of the depth and slope of the main thermocline across the Pacific and not permitting the interface to surface. In linear wave theory the density difference, $\Delta\rho$, and the upper layer thickness, H, combine to form a single parameter--the phase speed of the internal Kelvin wave. The expression for this phase speed is given by

$$C_k = \left(\frac{g\Delta\rho H}{\rho_o}\right)^{\frac{1}{2}} = (gH_n)^{\frac{1}{2}} \quad .$$

where C_k is the speed of internal Kelvin wave for the n^{th} baroclinic mode and H_n is the corresponding equivalent depth. The parameters in Table 1 yield a value for H_1 of 43.75 cm, which is consistent with the order of the equivalent depth for the first baroclinic mode near the equator (Moore and Philander, 1977). Because the phase speed is proportional to the square root of H_n, the model results are not highly sensitive to changes in the equivalent depth.

tional to the square root of H_n, the model results are not highly sensitive to changes in the equivalent depth.

Table 1. Model Parameters

$\Delta\rho/\rho = 2.5 \times 10^{-3}$	$L_y = \pm 1500$ km
$H = 175$ m	$A = 10^6$ cm^2 sec^{-1}
$\beta = 2.25 \times 10^{-11}$ m^{-1} s^{-1}	$g = 9.8$ m sec^{-2}
$L_x = 1.3 \times 10^4$ km	$\Delta t = 5400$ sec

In Figs. 3 and 4, the solutions for the height field are shown for the steady and periodic cases, respectively. The effects of waves in the solutions are evident by kinks in the contours and a change in the contour spacing after the wave front propagates past a particular point. In Fig. 3, the initial time rate of change of the pycnocline height anomaly (PHA) in the interior region reverses sign following the passage of the Kelvin wave from the west and intensifies after the passage of the Rossby wave from the east. Also, in agreement with linear theory, the Rossby wave takes thrice the time to cross the basin as the Kelvin wave. The effects of the reflections of each of these waves are also very conspicuous. The equivalent plot of the upper layer thickness (ULT) for the periodic wind case is shown in Fig. 4. In this case, it is most difficult to differentiate between the effects of the zonally propagating waves and the forced interior response. Hence, for time-variable forcing, a technique is required whereby the effects of the various waves may be identified and their importance assessed.

b. Interior Response

In order to identify the effects of the Kelvin waves, Rossby waves,

b. Interior Response

In order to identify the effects of the Kelvin waves, Rossby waves, and their reflections, an expression for the vertical velocity of the model equatorial pycnocline is derived. The derivation is based upon the

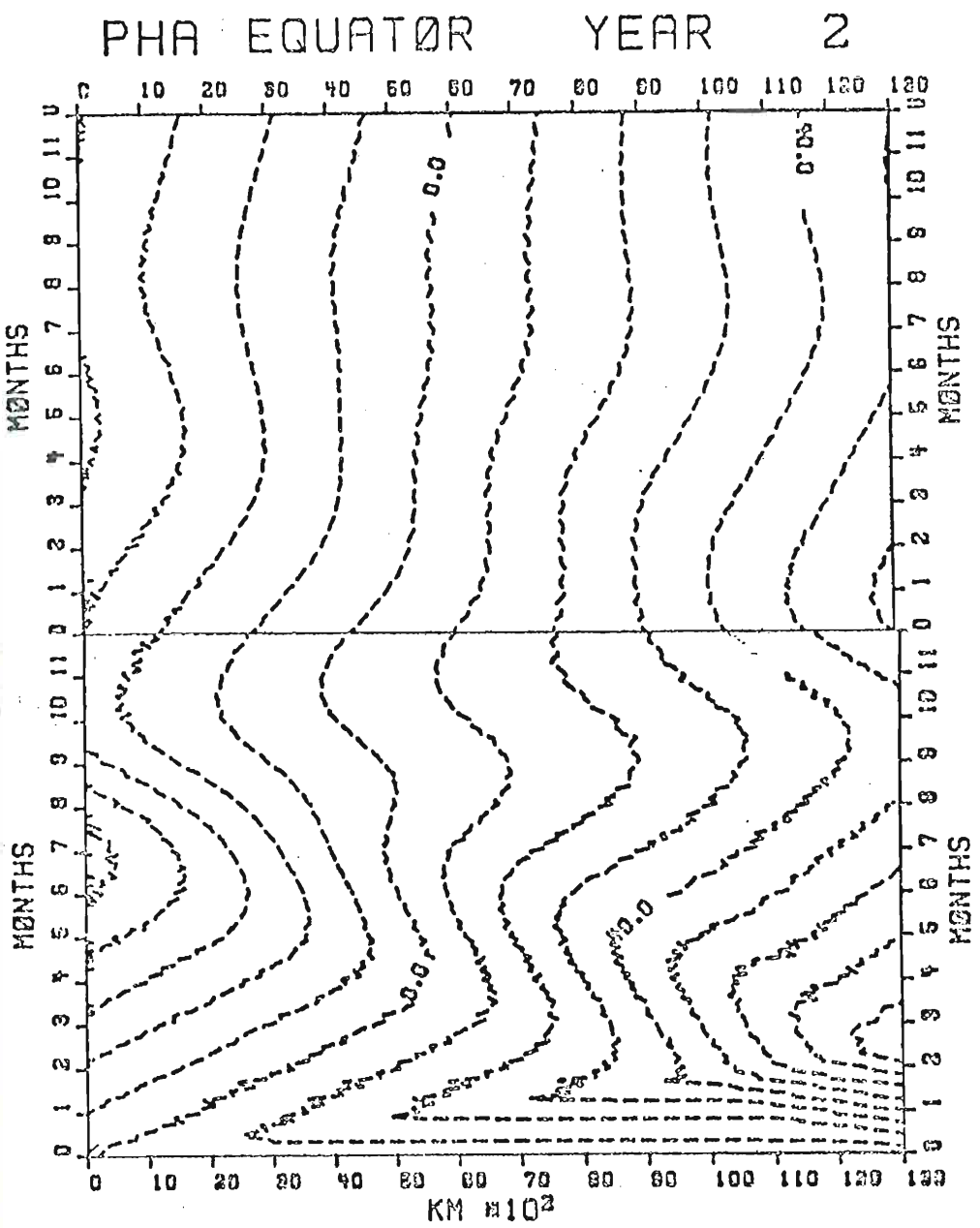

Fig. 3. The x-t section of pycnocline height anomaly for a case in which a steady, zonal, uniform wind stress is applied impulsively to an ocean initially at rest. The contour interval is 10 m. The wind stress, which is directed from west to east initiates downwelling at the eastern boundary and upwelling at the western boundary.

Fig. 3. The x-t section of pycnocline height anomaly for a case in which a steady, zonal, uniform wind stress is applied impulsively to an ocean initially at rest. The contour interval is 10 m. The wind stress, which is directed from west to east initiates downwelling at the eastern boundary and upwelling at the western boundary.

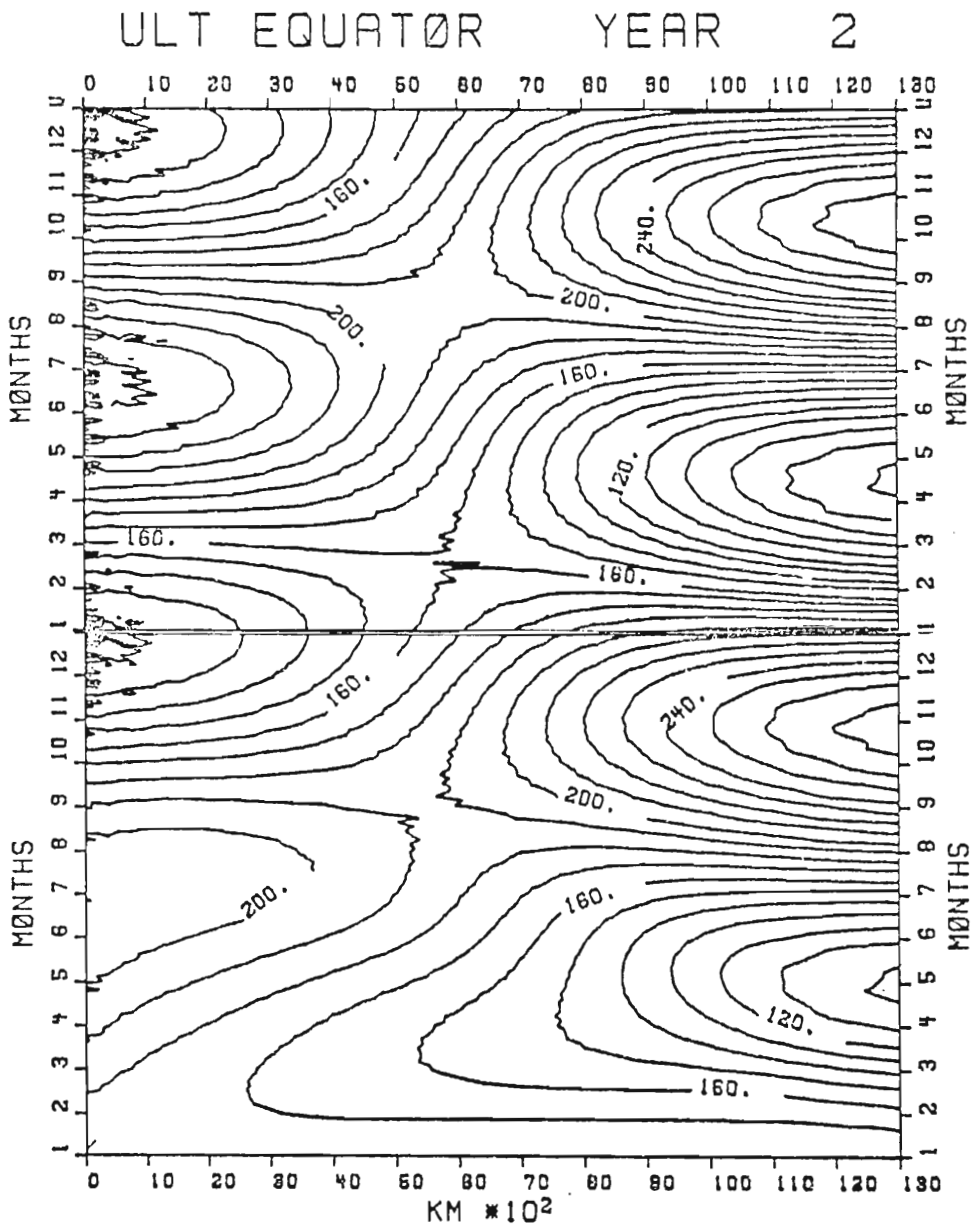

Fig 4. The x-t section of upper layer thickness (ULT) for a zonal, uniform wind with an annual period. The contour interval is 10 m. The initial layer thickness is 175 m.

zonal, uniform wind with an annual period. The contour interval is 10 m. The initial layer thickness is 175 m.

linear theory of equatorial β-plane wave dynamics; however, the numerical model is used to determine some of the parameters. Since the solutions produced by the linear version of the numerical model are very close to those predicted by linear theory, the resulting expression is a useful tool to the study of the equatorial response to time-variable zonal winds.

The foundation of the derivation is the equatorial response to uniform zonal winds in an ocean with no meridional boundaries. This will be referred to as the interior solution . This problem was first solved by Yoshida (1959) and more recently (as well as more generally) by Moore and Philander (1977). Consider the reduced-gravity model (6) which is forced by a uniform zonal wind and in which all zonal derivatives are neglected. In order to filter out inertial oscillations, the acceleration of the meridional velocity is also neglected. Substitution in favor of the meridional velocity yields:

$$\gamma^4 V_{yy} - y^2 V = \frac{y}{\rho\beta}\left(\frac{\tau^x}{H}\right) \qquad (14)$$

where γ is the equatorial radius of deformation $= \left(\frac{g'H}{\beta^2}\right)^{\frac{1}{4}}$. The value of the vertical velocity at the interface is essentially given by

$$W = -\frac{\partial h}{\partial t} = H\,\frac{\partial v}{\partial y}$$

which at the equator is equal to

$$W = -\frac{.6\tau^x}{C} \qquad (15)$$

where $C = \sqrt{g'H}$. The factor .6 arises from the non-dimensional value of the meridional divergence at the equator. Although this expression
where $C = \sqrt{g'H}$. The factor .6 arises from the non-dimensional value of the meridional divergence at the equator. Although this expression

was originally derived for a steady wind stress, it is also valid for a time-variable wind provided the period of the forcing is much greater than the inertial period.

Associated with the motion of the interface in the interior response is a zonal acceleration often referred to as the Yoshida jet. In the presence of meridional boundaries this zonal current must be divergent, thereby exciting equatorially trapped Kelvin and Rossby waves. These waves propagate according to the free wave dispersion relation given by (10), and with amplitudes dependent upon both the magnitude of the divergence and the type of wave. For steady forcing, the free waves and their reflections establish a steady state in which the wind-stress force is balanced by the zonal pressure gradient. The existence of such a balance for variable forcing, however, depends upon the stratification, the basin width and the period. In order to determine precisely the proper balance for given parameters, it is necessary to know the magnitude of the free wave response and of the subsequent reflections.

c. Uniformly Distributed Zonal Wind Case

In this section the equatorial response to a uniformly distributed time-variable zonal wind is examined in terms of the vertical velocity of the model pycnocline along the equator. The vertical motion of the pycnocline is influenced not only by the local response, but also by the excitation of equatorially trapped waves and the subsequent reflections of these waves at the boundaries. The magnitude of the interior response depends directly upon the magnitude of the wind stress and, for the frequencies of interest in this paper, the local response is in phase with the forcing. Also, the amplitudes of the waves excited at the boun-

daries (the Rossby wave at the eastern boundary and the Kelvin wave at the western boundary) are directly proportional to the amplitude of the wind stress. If the forcing has a sinusoidal variation in time, each of these waves produces a sinusoidal zonal distribution as it propagates away from the boundary of its origin. In the interior, the phase with respect to the forcing of a particular wave depends upon the ratio of the distance from the original boundary to its wavelength. Upon reflection, the waves undergo no phase changes, because the meridional walls are free boundaries for the height field.

Let us consider the equatorial response to a time-varying spatially-uniform wind with a frequency and an initial phase given by ω and ϕ, respectively. The vertical motion of the interface may be expressed as the sum of the interior response and the various contributions of the waves excited by the wind stress and by the reflections from the boundaries, i.e.,

$$\begin{aligned} W(x, t) = {} & W_I \sin(\omega t + \phi) + W_K \sin(\omega(t - \frac{x}{C_K}) + \phi) \\ & + W_R \sin(\omega(t - \frac{(L-x)}{C_R}) + \phi) \\ & + W_{KR} \sin(\omega(t - \frac{L}{C_K} - \frac{(L-x)}{C_R}) + \phi) \\ & + W_{RK} \sin(\omega(t - \frac{L}{C_R} - \frac{x}{C_K}) + \phi) \\ & + W_{KRK} \sin(\omega(t - L(\frac{1}{C_R} + \frac{1}{C_K}) - \frac{x}{C_K}) + \phi) \\ & + W_{RKR} \sin(\omega(t - L(\frac{1}{C_R} + \frac{1}{C_K}) - \frac{(L - x)}{C_R}) + \phi) \end{aligned} \tag{16}$$

where C_K is the speed of the Kelvin wave, C_R is the speed of the first mode Rossby wave ($C_K/3$) and L is the width of the basin. The amplitudes where C_K is the speed of the Kelvin wave, C_R is the speed of the first mode Rossby wave ($C_K/3$) and L is the width of the basin. The amplitudes of the interior response, the Kelvin wave and the Rossby wave are denoted

by W_I, W_K and W_R, respectively. The remaining terms refer to the waves generated by the reflections of the free waves at the eastern and western boundaries. For example, the term W_{KR} represents the amplitude of the westward propagating Rossby wave resulting from the incidence of the initial Kelvin wave onto the eastern boundary; the amplitude of this wave is given by the product of the amplitude of the initial Kelvin wave and the effective reflection coefficient at the eastern boundary. Only the first latitudinal mode Rossby waves are included even though the higher modes are also excited both by the wind stress and the eastern boundary reflection. The amplitudes of the higher modes will be shown to be negligible in comparison to the amplitude of the gravest mode Rossby wave. Equation (16) also assumes that the vertical velocity associated with a wave undergoes no phase change upon reflection.

The amplitude of the forced motion, W_I, may be determined from (15). Hence, in order to complete the expression, it is necessary to know W_K, W_R and the reflection coefficients at the eastern and western boundaries. Since (16) will be used to interpret the numerical model results, the model will be used to determine the unknown parameters.

Prior to the calculation of the unknown parameters in (16), it will be shown that the numerical model results are very close to those predicted by linear theory. Let us reconsider the steady east wind case, the first two years of which are shown in Fig. 3. In order to examine the local response, the PHA for the first forty days at a point 9,000 km from the western boundary and the theoretical solution determined from (15) are plotted in Fig. 5. This figure clearly shows that the numerical model solution away from the effects of boundaries oscillates closely

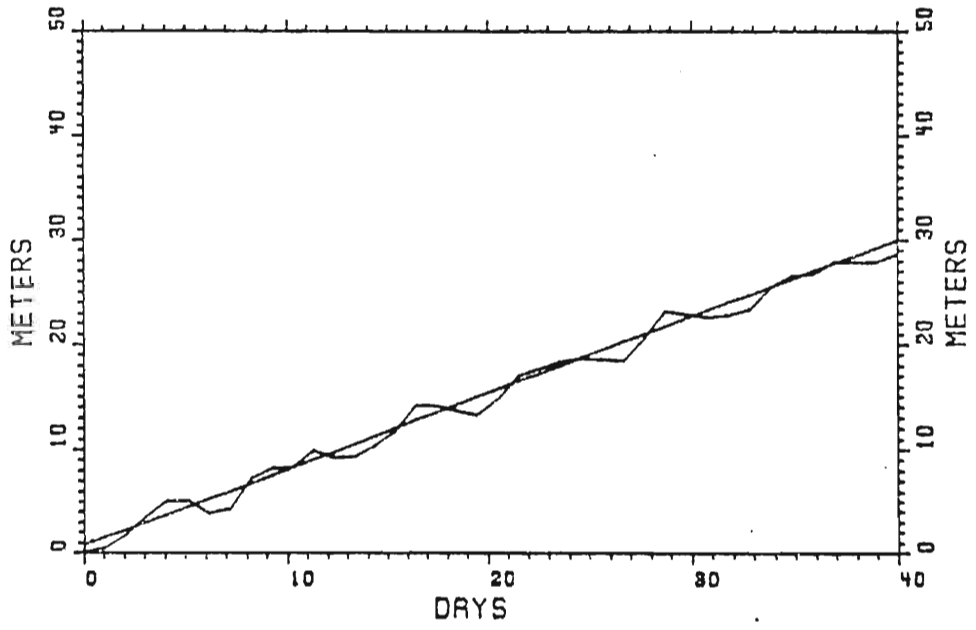

Fig. 5. Comparison of analytical model solutions for the first 40 days of the steady wind case. The straight line is the analytical solution (Yoshida solution) for the PHA; inertial oscillations cause the numerical solution to oscillate about the theoretical value.

about the analytic solution given by (15). Linear wave theory also stipulates that 72.6 days are required for the Kelvin wave to cross the basin and 218 days for the first mode, non-dispersive Rossby wave to travel that distance. These are within 5% of the values demonstrated by the numerical model. Finally, the steady solution of this system is a balance between the wind stress and the zonal pressure gradient, i.e.,

$$g'h_x = \frac{\tau^x}{\rho_o H} \quad . \tag{17}$$

For the given parameters, the steady slope of the interface is 7×10^{-6}. From Fig. 3, it can be seen that the zonal slope of the interface at the end of year two is essentially 70 meters in 10,000 km, i.e., 7×10^{-6}.

The amplitudes of the initial Kelvin and Rossby waves may be determined from Fig. 6, which is an enlargement of the first four months of Fig. 3. Along the western boundary, the rate of upwelling prior to the arrival of the Rossby wave from the east is given by the sum of the amplitudes of the interior response and the Kelvin wave. The value of the upwelling rate at the western boundary during this period is 9 m/month, while that of the interior is -22.5 m/month. Hence, the amplitude of the Kelvin wave is given by

$$W_K = -W_I + W = 31.5 \text{ m/month.}$$

Hence, regardless of the frequency or the amplitude of the forcing, the numerical model predicts that the relationship between the amplitude of interior response and that of the associated Kelvin wave is given by

$$W_K = -1.4\ W_I. \tag{18}$$

interior response and that of the associated Kelvin wave is given by

$$W_K = -1.4\ W_I. \tag{18}$$

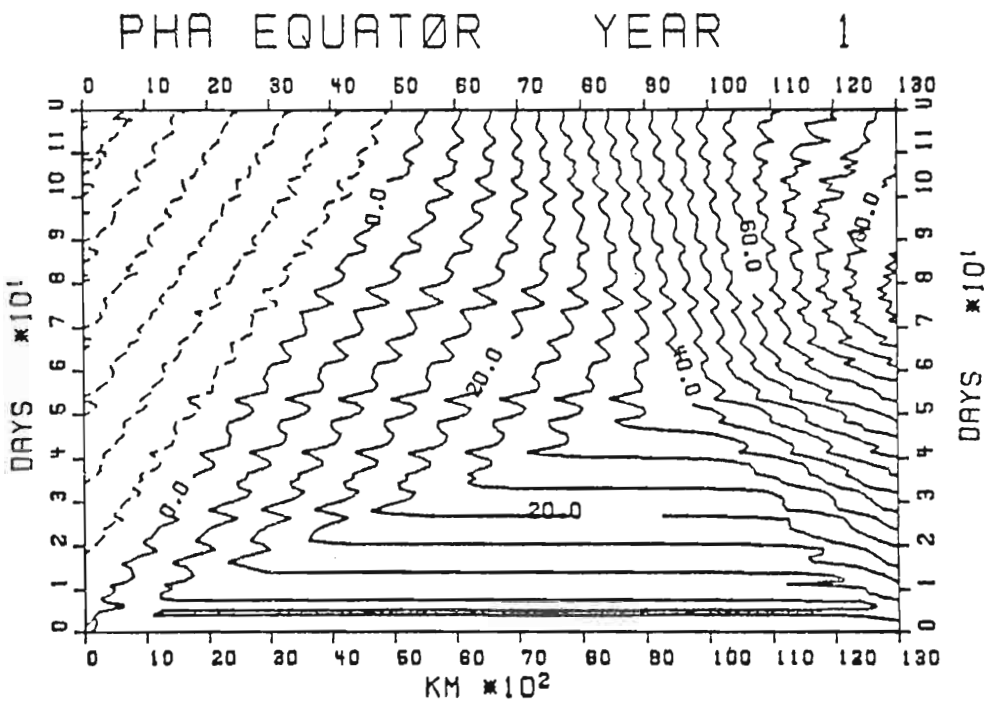

Fig. 6. The x-t section of PHA along equator for first 4 months of the steady wind case. The contour interval is 5 m. Positive values (solid lines) indicate a deeper pycnocline depth than the initial value.

In a similar calculation, the amplitude of the Rossby wave is determined to be

$$W_R = .6W_I. \tag{19}$$

The divergence of the Kelvin wave at the equator is more than twice that of the Rossby wave and opposite in sign both to the Rossby wave and the interior upwelling. Hence, the initial motion of the model pycnocline is four times greater at the eastern boundary than at the western boundary. The steady-state value of the upper layer thickness at the eastern boundary is eventually reached due to the effects of Kelvin waves arriving from the west which alternately produce vertical velocities of opposite signs and ever diminishing amplitudes. These Kelvin waves are excited by the wind stress and the reflections of Rossby waves from the western boundary.

The magnitudes of the reflected waves are most easily determined from the steady wind case. At the eastern boundary, the vertical velocity between the time of the incidence of the initial Kelvin wave and the arrival of the second one is given by:

$$W(x = L) = W_I + W_K + W_R + W_{KR}. \tag{20}$$

The magnitudes of W_I, W_K and W_R have already been determined. The value of W_{KR} is equal to the product of W_K and the vertical velocity reflection coefficient at the eastern boundary. The value of $W(x = L)$ is the upwelling rate at the eastern boundary between the third and tenth months (Fig. 3). The expression for the reflection coefficient, R_E, at the eastern boundary is given by

(Fig. 3). The expression for the reflection coefficient, R_E, at the eastern boundary is given by

$$R_E = \frac{W(x = L) - W_I - W_K - W_R}{W_K} .$$

The value of R_E is determined to be .36. In a similar type calculation, the reflection coefficient at the western boundary, R_W, is found to be .75. The smaller value at the eastern side is the result of the incident energy being distributed over a wider latitudinal range. The reflection at the western boundary funnels energy into the equatorial region, whereas at the eastern boundary, the incident energy is distributed over many westward-propagating Rossby waves and the coastally trapped Kelvin wave. Table 2 is a list of the parameters necessary to complete the expression for the vertical velocity (16).

Table 2. Parameters for Vertical Velocity Equation: Basin Wide Wind Stress

W_K	$= -1.4\ W_I$
W_R	$= .6\ W_I$
R_E	$= .36$
R_W	$= .75$

An alternate and more compact expression for the vertical velocity (16) is

$$
\begin{aligned}
W(x,\,t) = {} & W_I \sin(\omega t + \phi) \\
& + \sum_{n=0,1} [(R_E R_W)^n W_R \sin(\omega(t - nL(\tfrac{1}{C_K} + \tfrac{1}{C_R}) - \tfrac{(L-x)}{C_R}) + \phi) \\
& + (R_E R_W)^n R_E W_K \sin(\omega(t - nL(\tfrac{1}{C_K} + \tfrac{1}{C_R}) - \tfrac{L}{C_K} - \tfrac{(L-x)}{C_R}) + \phi)] \\
& + \sum_{n=0,1} [(R_E R_W)^n R_W W_R \sin(\omega(t - nL(\tfrac{1}{C_K} + \tfrac{1}{C_R}) - \tfrac{L}{C_R} - \tfrac{x}{C_K}) + \phi) \\
& + (R_E R_W)^n W_K \sin(\omega(t - n(\tfrac{1}{C_K} + \tfrac{1}{C_R}) - \tfrac{x}{C_K}) + \phi)]
\end{aligned}
\tag{21}
$$

where the first summation is over all the first mode Rossby waves in the system and the second is over all the Kelvin waves. Since $R_E W_K$ is approximately equal to $-W_R$, the Rossby wave excited by the first reflection of the wind generated Kelvin wave is nearly the same magnitude as the wind-induced Rossby wave. At the western boundary, however, the first reflected Kelvin wave has approximately one-third the amplitude of the directly forced Kelvin wave.

As a check on the accuracy of the parameter calculations and the assumption of excluding higher mode Rossby waves in (16), a comparison will be made between the analytical expression and the numerical model results. An advantage of examining the response of the vertical velocity is that for the long, low frequency waves considered here, the expressions for the reflection and generation of equatorially trapped waves are independent of frequency. Therefore, let us consider the case shown in Fig. 4 in which a wind stress of amplitude .3 dynes cm^{-2} with a period of one year is applied to the model ocean. Fig. 7 is a comparison of the model solution for the third year of integration with the analytical
iod of one year is applied to the model ocean. Fig. 7 is a comparison of the model solution for the third year of integration with the analytical
expression (16). The vertical velocity is calculated from the model

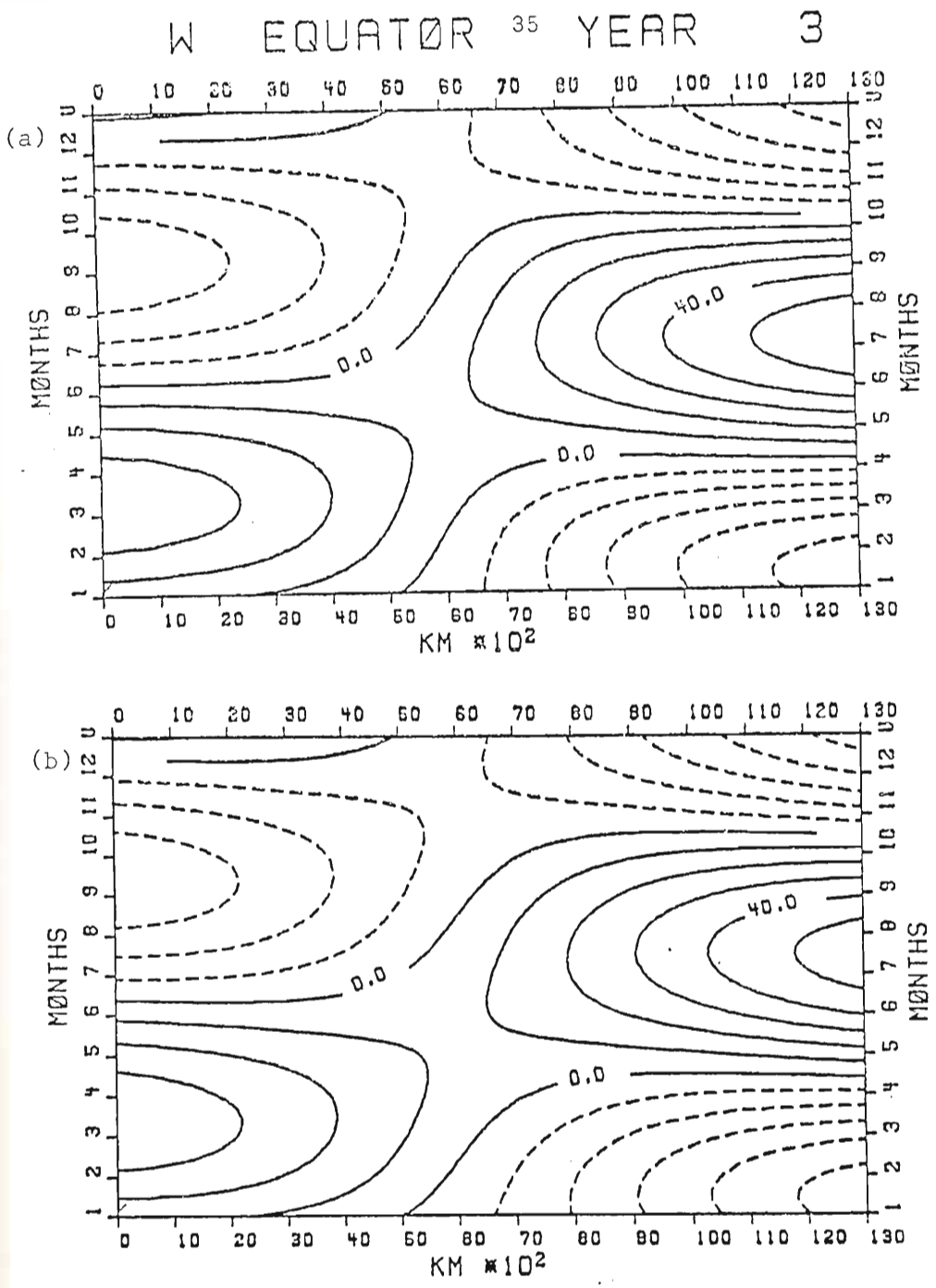

Fig. 7. Comparison of (a) numerical and (b) analytical solutions for the upper layer thickness tendency along the equator for the annual forcing case. The contour interval is 10 m/mo. Dashed contours indicate deepening. Inertial oscillations have been filtered out of the numerical solution.

forcing case. The contour interval is 10 m/mo. Dashed contours indicate deepening. Inertial oscillations have been filtered out of the numerical solution.

solutions after the removal of the inertia-gravity waves. In Fig. 8, time sections at the western and eastern boundaries are compared for the two plots in Fig. 7. The close agreement between the two solutions reveals that the analytical expression is an accurate predictor of the numerical solutions and will be an invaluable tool in identifying the effects of the various equatorial waves.

d. Longitudinally Bounded Zonal Wind Case

One of the weaknesses of the above expression is that it cannot account for zonal variation of the wind stress. Although the equatorial trade winds extend virtually across the breadth of the Pacific, there are considerable zonal variations in the magnitude of the wind stress. The divergence of the zonal wind can excite equatorially trapped waves in the interior region in addition to those waves generated at the meridional boundaries. Since the numerical model is a useful tool in the investigation of the equatorial response to more realistic type wind-stress distributions, it would be beneficial to derive an expression similar to (16) for winds with a non-uniform zonal variation along the equator. The wind stress will be decomposed into an arbitrary number of longitudinally bounded regions, within which each section the wind is uniform. Hence, in the same manner as before, we will derive an expression for the vertical velocity due to a suddenly imposed, steady, uniform wind which is confined to an interior region of arbitrary longitudinal extent. McCreary (1977) examined the radiation of equatorial waves from a region with a steady wind stress whose amplitude varied linearly in the zonal direction. We prefer, however, to consider a patch of spatially uniform wind stress in order to apply the theory developed for

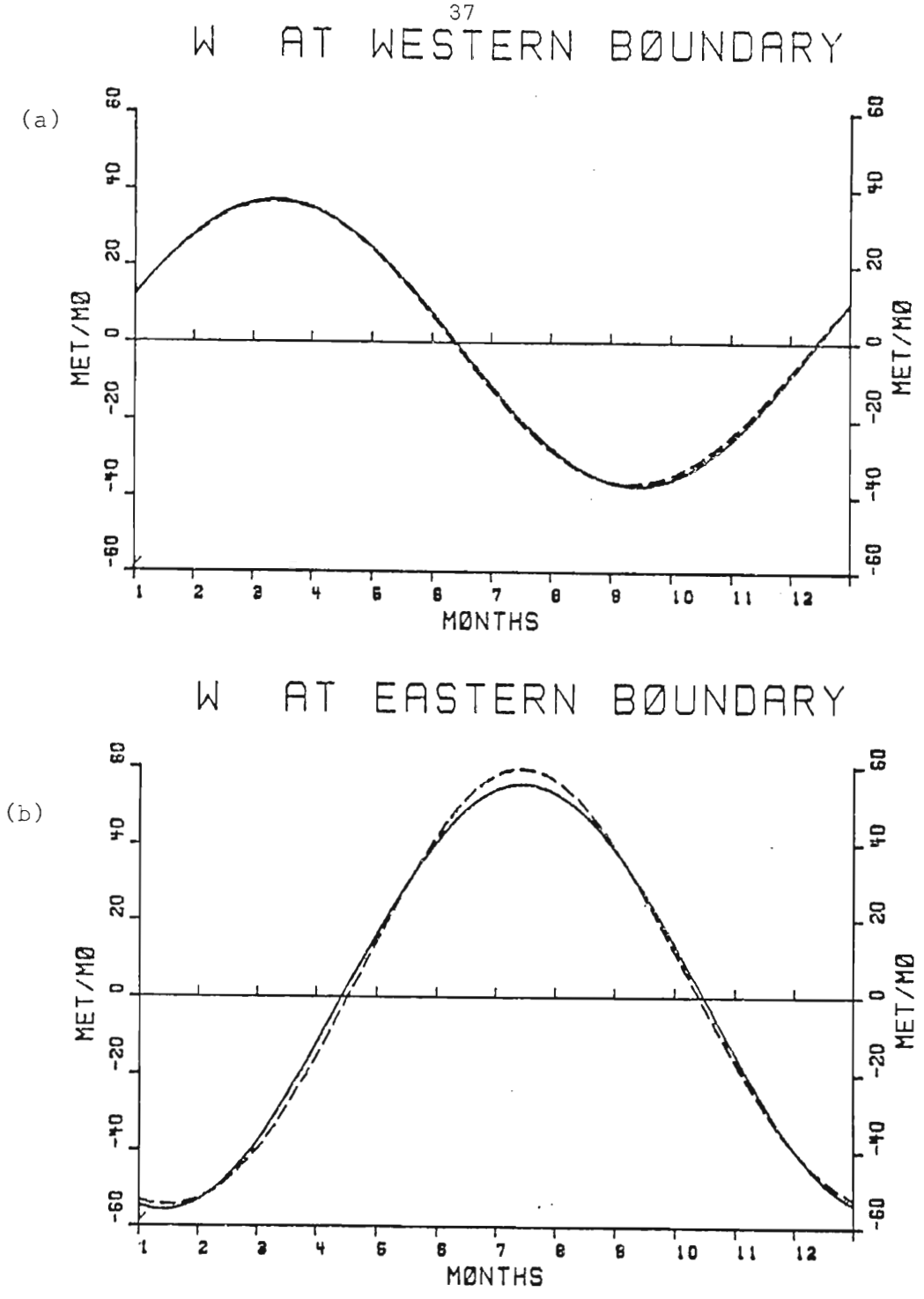

Fig. 8. Comparison of numerical and analytical solutions for ULT tendency at (a) western boundary and (b) eastern boundary for the same case shown in Fig. 7. The numerical solution is designated by the

Fig. 8. Comparison of numerical and analytical solutions for ULT tendency at (a) western boundary and (b) eastern boundary for the same case shown in Fig. 7. The numerical solution is designated by the dashed line.

the interior response given by (15). Although we impose a different distribution of the wind stress patch than that used by McCreary, the philosophy of our approach is the same, i.e., the solution forced by a wind stress of arbitrary zonal distribution may be decomposed into the sum of responses due to individual wind-stress patches.

Consider the case in which the model ocean is forced by a wind stress which is uniform in a longitudinal strip of width d and has zero amplitude outside this region, that is,

$$\begin{aligned} \tau^x &= R_{(x)}\tau \\ R_{(x)} &= 1 \quad a < x < a + d \\ &= 0 \quad 0 < x < a,\ a + d < x < L \\ \tau &= A \sin(\omega t + \phi) \end{aligned} \tag{22}$$

The divergence of the wind stress at each edge excites an equatorially trapped Kelvin wave and a series of Rossby waves. In deriving an expression for the vertical velocity along the equator, we shall include only the effects of the first mode Rossby wave and the Kelvin wave. An expression similar to (21) for the case above may be written as:

$$\begin{aligned} W(x, t) = {} & W_I \sin(\omega t + \phi) \\ & + W_{IK}\, H(x-a-d) \sin\left(\omega\left(t - \frac{(x-a-d)}{C_K}\right) + \phi\right) \\ & + W_{IR}\, (1 - H(x-a-d)) \sin\left(\omega\left(t - \frac{(a+d-x)}{C_R}\right) + \phi\right) \\ & - W_{IK}\, H(x - a) \sin\left(\omega\left(t - \frac{(x-a)}{C_K}\right) + \phi\right) \\ & - W_{IR}\, (1 - H(x-a)) \sin\left(\omega\left(t - \frac{(a-x)}{C_R}\right) + \phi\right) \\ & - W_{IR}\, (1 - H(x-a)) \sin\left(\omega\left(t - \frac{(a-x)}{C_R}\right) + \phi\right) \end{aligned}$$

$$+ \sum_{n=0,1} \Big\{ R_W W_{IR} (R_E R_W)^n \left[\sin\left(\omega\left(t - nL\left(\frac{1}{C_R} + \frac{1}{C_K}\right) - \frac{(a+d)}{C_R} - \frac{x}{C_K}\right) + \phi\right) \right.$$

$$\left. - \sin\left(\omega\left(t - nL\left(\frac{1}{C_R} + \frac{1}{C_K}\right) - \frac{a}{C_R} - \frac{x}{C_K}\right) + \phi\right)\right]$$

$$+ W_{IK} (R_E R_W)^{n+1} \left[\sin\left(\omega\left(t - nL\left(\frac{1}{C_R} + \frac{1}{C_K}\right) - \left(\frac{L-a-d}{C_K} + \frac{L}{C_R}\right) - \frac{x}{C_K}\right) + \phi\right)\right.$$

$$\left. - \sin\left(\omega\left(t - nL\left(\frac{1}{C_R} + \frac{1}{C_K}\right) - \left(\frac{L-a}{C_K} + \frac{L}{C_R}\right) - \frac{x}{C_K}\right) + \phi\right)\right] \qquad (23)$$

$$+ W_{IR} (R_E R_W)^{n+1} \left[\sin\left(\omega\left(t - nL\left(\frac{1}{C_R} + \frac{1}{C_K}\right) - \frac{(a+d)}{C_R} + \frac{L}{C_K}\right) - \frac{(L-x)}{C_R}\right) + \phi\right)\right.$$

$$\left. - \sin\left(\omega\left(t - nL\left(\frac{1}{C_R} + \frac{1}{C_K}\right) - \left(\frac{a}{C_R} + \frac{L}{C_K}\right) - \frac{(L-x)}{C_R}\right) + \phi\right)\right]$$

$$+ R_E W_{IK} (R_E R_W)^n \sin\left(\omega\left(t - nL\left(\frac{1}{C_R} + \frac{1}{C_K}\right) - \frac{(L-a-d)}{C_K} - \frac{(L-x)}{C_R}\right) + \phi\right)$$

$$\left. - \sin\left(\omega\left(t - nL\left(\frac{1}{C_R} + \frac{1}{C_K}\right) - \frac{(L-a)}{C_K} - \frac{(L-x)}{C_R}\right) + \phi\right)\right] \Big\}$$

where W_{IK} and W_{IR} are the respective amplitudes of the equatorial Kelvin wave and the first mode Rossby wave generated at the edge of a wind stress of step function form. In the case of a rectangular pulse wind-stress distribution, the waves excited at one edge are equal in magnitude but opposite in sign to the waves generated at the other edge. The function $H(x - x_o)$ is the Heaviside step function; all other terms retain their previous definitions.

The amplitudes of the Rossby and Kelvin waves excited at the edge of a zonal wind-stress patch are determined by examining a case for which the forcing is a steady, uniform, eastward wind stress of .3 dynes cm^{-2} magnitude and which extends 7,000 km from the western boundary. Fig. 9 is a plot of the PHA for the first 1.5 years. As in the previous steady wind case, the steady-state pressure gradient in the forced region is

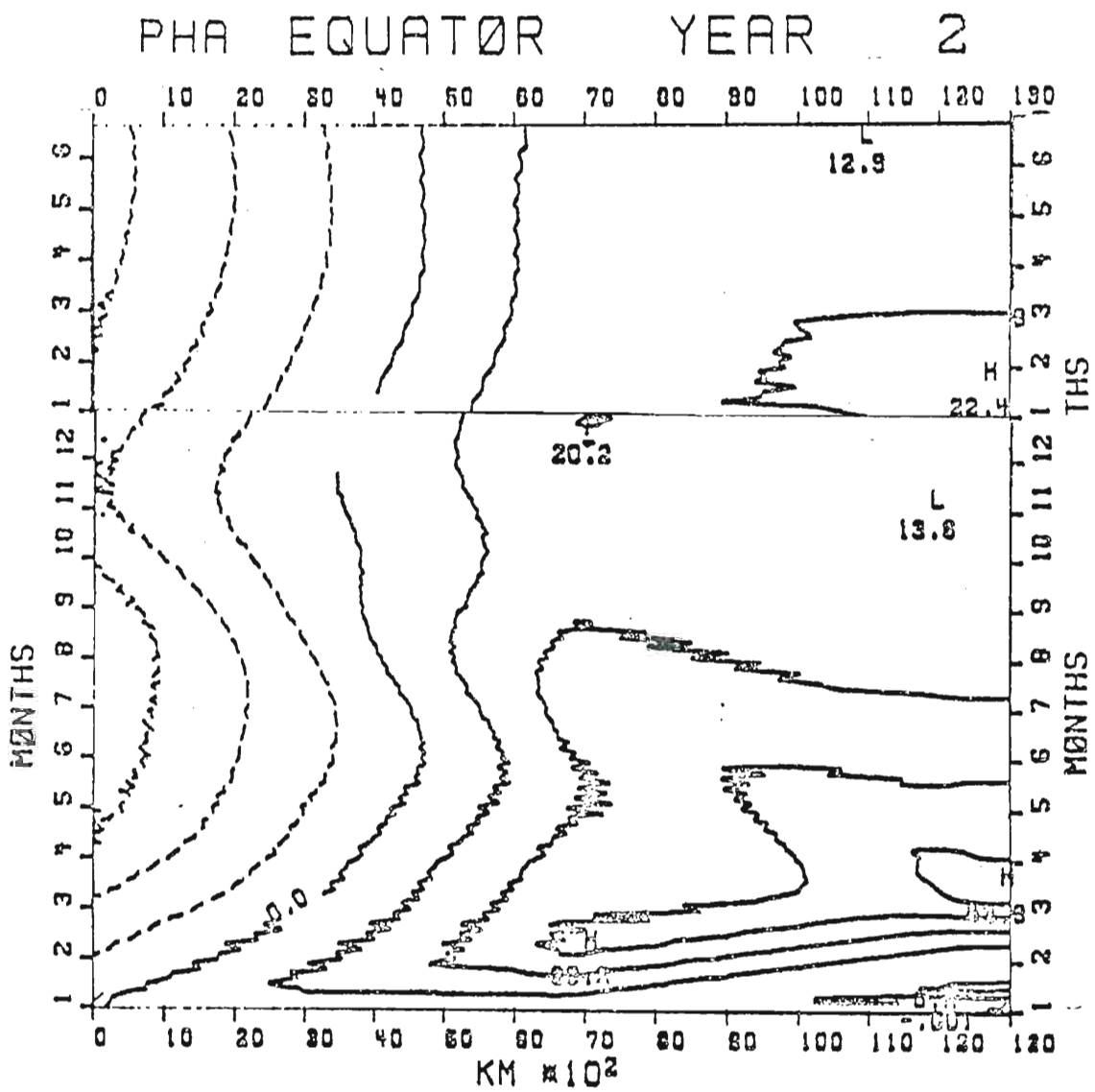

Fig. 9. The x-t section of PHA along the equator for a case in which a steady, meridionally uniform, zonal wind stress is applied impulsively to an ocean at rest. The wind stress extends only 7,000 km from the western boundary and is directed from west to east. The contour interval is 10 m.

which a steady, meridionally uniform, zonal wind stress is applied impulsively to an ocean at rest. The wind stress extends only 7,000 km from the western boundary and is directed from west to east. The contour interval is 10 m.

7×10^{-6}. The PHA for the first four months at a point approximately 11,000 km from the western boundary is shown in Fig. 10. The arrival of the Kelvin wave around day 20 initiates vertical motion which remains unchanged until the nearly simultaneous arrival of the reflected Rossby wave from the eastern boundary and the Kelvin wave from the western boundary near day 60. From this and similar plots, the magnitude of the vertical velocity associated with this Kelvin wave is determined to be 26 m/month, i.e.,

$$W_{IK} = 1.15\ W_I \tag{24}$$

Similarly, the magnitude of the Rossby wave generated at the edge of the wind stress is found to be

$$W_{IR} = .17\ W_I \tag{25}$$

As a check on the parameters, Fig. 11 is a comparison of the numerical and analytic solutions (23) for a case in which the wind stress has a period of one year, an amplitude of .5 dynes cm^{-2}, and is confined within a region of 7,000 km to 11,000 km from the western boundary.

e. Discussion and Critique

For the linear inviscid equatorial β-plane problem (3), the reflection coefficients at the eastern and western boundaries may be determined using the technique of Moore (1968) who solves for the amplitude(s) of the free wave(s) necessary to satisfy the no-flux condition at the meridional boundary. The corresponding values of R_E and R_W, using Moore's method, are 0.5 and 1.0, respectively. Hence, the numerical model underestimates the inviscid reflection coefficients by approxi-

Moore's method, are 0.5 and 1.0, respectively. Hence, the numerical model underestimates the inviscid reflection coefficients by approxi-

mately twenty-five percent. This is most likely caused by the effects

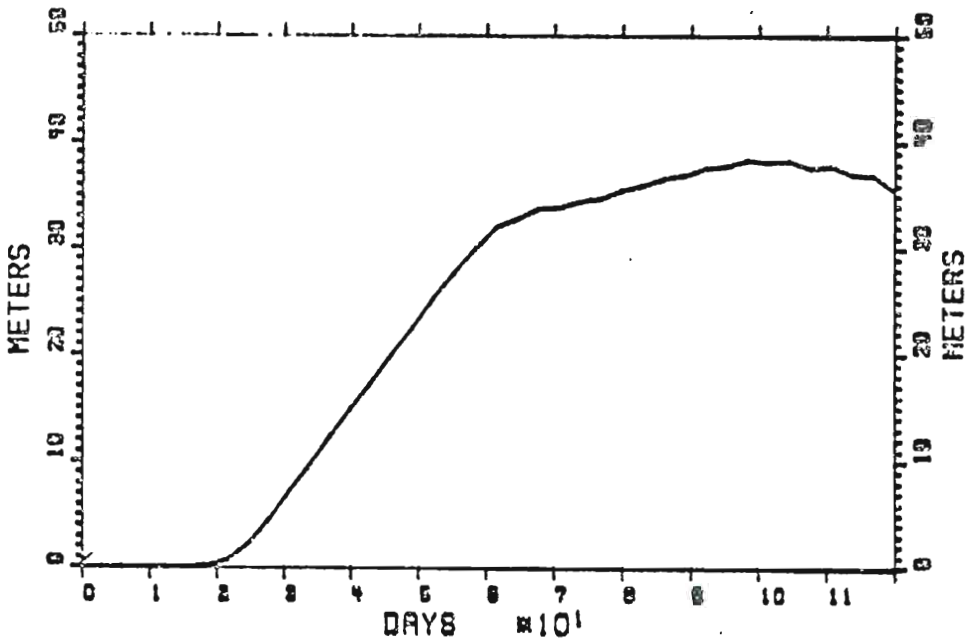

Fig. 10. Time series of PHA at a point 10,500 km from the western boundary at the equator for the limited wind stress case shown in Fig. 4.

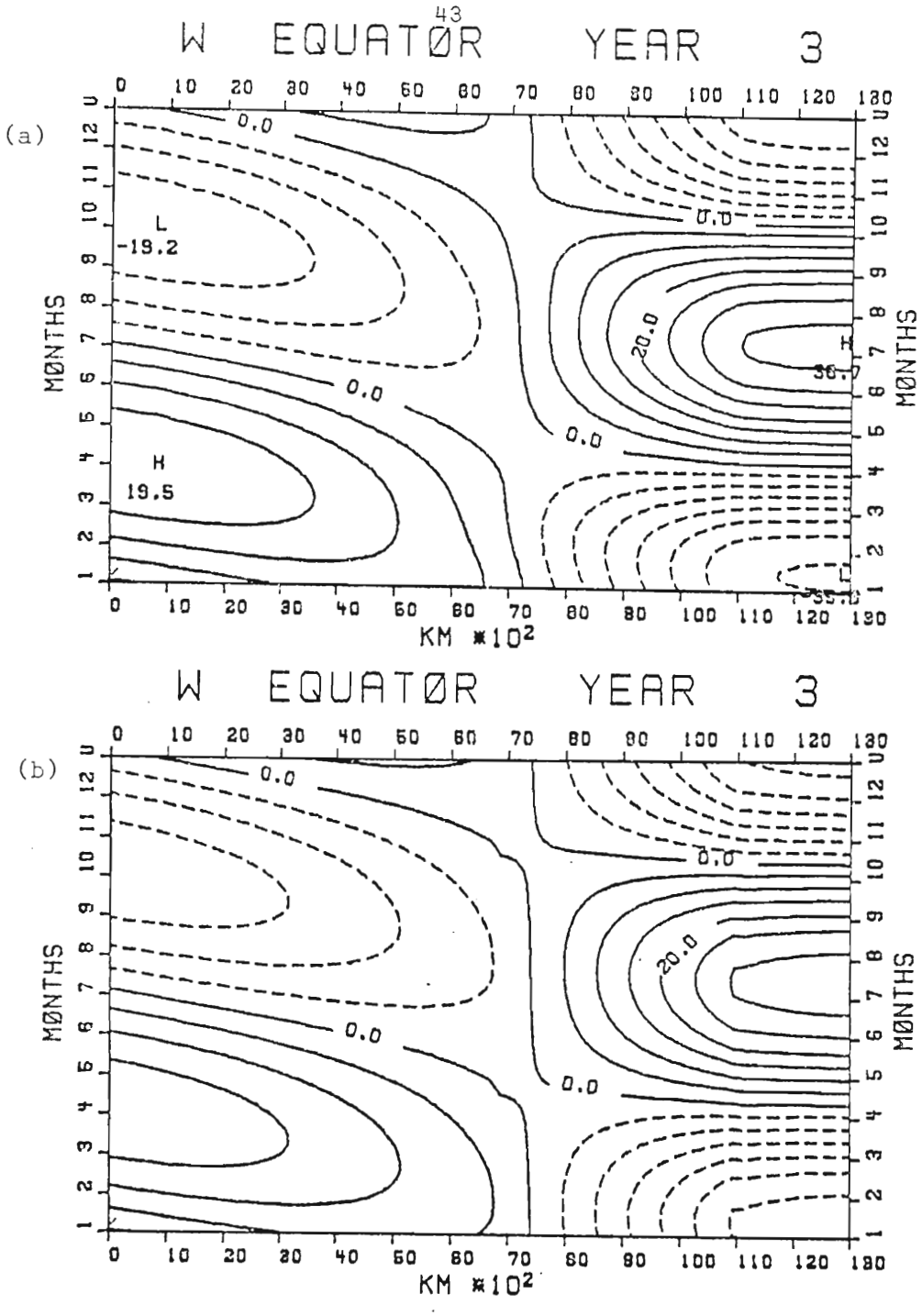

Fig. 11. Comparison of ULT tendency along the equator for (a) numerical and (b) analytical solutions. The wind stress is non-zero between 7,000 and 11,000 km and has a period of one year. The contour interval is 5 m/mo.

between 7,000 and 11,000 km and has a period of one year. The contour interval is 5 m/mo.

of both viscosity and the periodic application of smoothing during the numerical integrations. If the coefficients determined from Moore's technique for the inviscid problem are utilized in (21) and (23), then the mixture of the inviscid analytical results and the numerical calculations is not sufficiently accurate to examine many of the numerical solutions. This is particularly true when the distribution of the forcing is represented by a combination of wind-stress patches. The subsequent accumulation of errors due to the summation over all the individual patches precludes a useful examination of the numerical results. Alternatively, one could determine the coefficients by an optimization method based on minimizing a measure of the differences between the numerical and the analytical solutions. It was judged, however, that such an approach is unnecessary; it has been shown that the expressions (21) and (23) are excellent approximations to the numerical model solutions and that the numerical results are very close to those predicted by linear theory.

An alternative form for the wind-stress patch is the type considered by McCreary (1977),that is one in which the amplitude of the forcing varies linearly. Such patches may be able to represent an arbitrary distribution of forcing with fewer elements than the type considered in this paper. However, the assumption of a uniform distribution within the patch allows one to differentiate between the interior or local response (Yoshida solution) and the effects of waves generated at the edges of each region of forcing. Since the waves excited at one edge of a patch are equal in magnitude but opposite in sign to those generated at the other region of forcing. Since the waves excited at one edge of a patch are equal in magnitude but opposite in sign to those generated at the other edge, the net response excited at the common boundary of two identical

patches is zero. Hence, if a sufficient number of patches are used to describe realistically the distribution of the forcing, the sum of all the equatorial waves generated at the edges of each patch will produce a realistic representation of the waves excited by a wind stress with an arbitrary distribution.

The close agreement between the approximate expressions, the numerical model results and linear theory appears to justify the neglect of Rossby waves with a latitudinal mode number greater than one. The value of the inviscid reflection coefficient at the eastern boundary for the m = 3 Rossby wave is -.12, according to Moore's technique. Hence, for the numerical model, the magnitude of the vertical velocity of the m = 3 Rossby wave would be less than ten percent of the magnitude of the incoming Kelvin wave. The effects of this Rossby wave are not distinctly evident in any of the time history plots at various grid points. In view of 1) the small magnitude of this wave in comparison to the other equatorial waves; and 2) the close agreement between the derived expressions for the vertical velocity and the numerical results, it is a justified approximation to neglect the Rossby wave modes greater than the first.

The effects on the reflection process of a non-meridional coastline have also been neglected. Presumably, an east-west tilt of the coastline would introduce an asymmetry into the reflected response, the magnitude of which would depend upon the departure of the coastline profile from a meridional orientation. Although the eastern boundary of the equatorial Pacific is not a meridional wall, such an assumption is a good first approximation. The use of a meridional wall at the western

equatorial Pacific is not a meridional wall, such an assumption is a good first approximation. The use of a meridional wall at the western boundary, however, is a more tenuous assumption. We examine only the

symmetrically reflected response. The influence of a non-meridional coastline orientation on equatorial waves is a topic deserving of attention.

The influence of bottom topography on the reflection of equatorially trapped waves at a boundary also requires further clarification. The system of equations (3) permits Kelvin waves as the only class of coastally trapped waves. However, in the presence of both topography and stratification, the coastally trapped waves are a hybrid of shelf and Kelvin waves, which under certain parameter ranges can be identified as mainly Kelvin or shelf-type waves (Wang, 1975; Allen, 1975). The characteristic offshore scale of the Kelvin wave is the radius of deformation, whereas the shelf width provides the primary scale of the shelf trapped wave. In the equatorial eastern Pacific, where the internal radius of deformation is on the order of 250 km and the shelf-slope region is approximately 50 km, one can reasonably expect that the reflection of a long internal Kelvin wave will not be substantially modified by the presence of such comparatively narrow topography. Even when the coastal Kelvin wave travels poleward into regions where the shelf width and the radius of deformation are comparable, the internal Kelvin wave may retain its essential characteristics (Suginohara, personal communication). Since, in this paper, we are not concerned with the details of the poleward propagating internal Kelvin wave, it is reasonable to neglect bottom topography in favor of studying the fundamental equatorial response to time-variable winds.

to time-variable winds.

4. ON THE EQUATORIAL RESPONSE TO TIME-VARIABLE WINDS

The derived expressions for the vertical velocity provide a useful mechanism for studying the general response of the equatorial ocean to time-variable zonal winds. In particular, we will examine such features as 1) the relative importance of the reflected equatorial waves; 2) the apparent amplitude maximum at the eastern boundary; and 3) the dependence of the equatorial response on the period of the forcing, the basin length, the stratification and the width of the forced region.

In order to investigate the above effects we will derive expressions for the amplitude and phase of the oscillations as functions of the model parameters and the zonal coordinate, x. The expression for the vertical velocity may be written in the form

$$W(x, t) = B(x) \sin(\omega t + \phi) + C(x) \cos(\omega t + \phi) \tag{26}$$

or

$$W(x, t) = A(x) \sin(\omega t + \phi + \theta(x)) \tag{27}$$

where

$$A(x) = (B(x)^2 + C(x)^2)^{\frac{1}{2}} \tag{28}$$

$$\theta(x) = (\tan^{-1}(C(x)/B(x)) \tag{29}$$

and B(x) and C(x) are derived from (21) or (23). The motion at any given point, x_i, along the equator will have a frequency $2\pi/T$, an ampli-

given point, x_i, along the equator will have a frequency $2\pi/T$, an ampli-

tude $A(x_i)$ and a phase with respect to the forcing of (x_i). The derivation of the expressions for B(x) and C(x) are given below.

First, let us examine the case for which a uniform oscillatory wind stress extends across the entire basin. If the horizontal coordinate, x, is scaled by the length of the basin, the functions B(x) and C(x) in (26) and (27) are given by

$$B(x) = W_I[1 + \sum_{n=0,1} [(R_E R_W)^n W_R \cos((4n + 3(1-x))\alpha) + (R_E R_W)^n W_K \cos((4n+x)\alpha) + (R_E R_W)^n R_W W_R \cos((4n+3+x)\alpha) + (R_E R_W)^n R_E W_K \cos((4n+1+3(1-x))\alpha)]] \quad (30)$$

$$C(x) = -W_I[\sum_{n=0,1} [(R_E R_W)^n W_R \sin((4n+3(1-x))\alpha) + (R_E R_W)^n W_K \sin((4n+x)\alpha) + (R_E R_W)^n R_W W_R \sin((4n+3+x)\alpha) + (R_E R_W)^n R_E W_K \sin((4n+1+3(1-x))\alpha)]]$$

where α is a non-dimensional parameter $(2\pi L/C_K T)$ which is the fraction of 2π radians given by the ratio of the basin length to the wavelength of the Kelvin wave. Equation (30) has also utilized the fact that $C_R = C_K/3$. Contour plots of the amplitude and phase as functions of x and α are shown in Fig. 12; the values of the reflection coefficients and wave magnitudes found in Table 2 have been used to evaluate (30). A detailed discussion of the significance of these plots will follow this section.

a. Importance of Reflected Waves

In order to judge the accuracy of expressions which neglect some of the terms in (21), Fig. 12 will be used as the standard. If only the

In order to judge the accuracy of expressions which neglect some of the terms in (21), Fig. 12 will be used as the standard. If only the

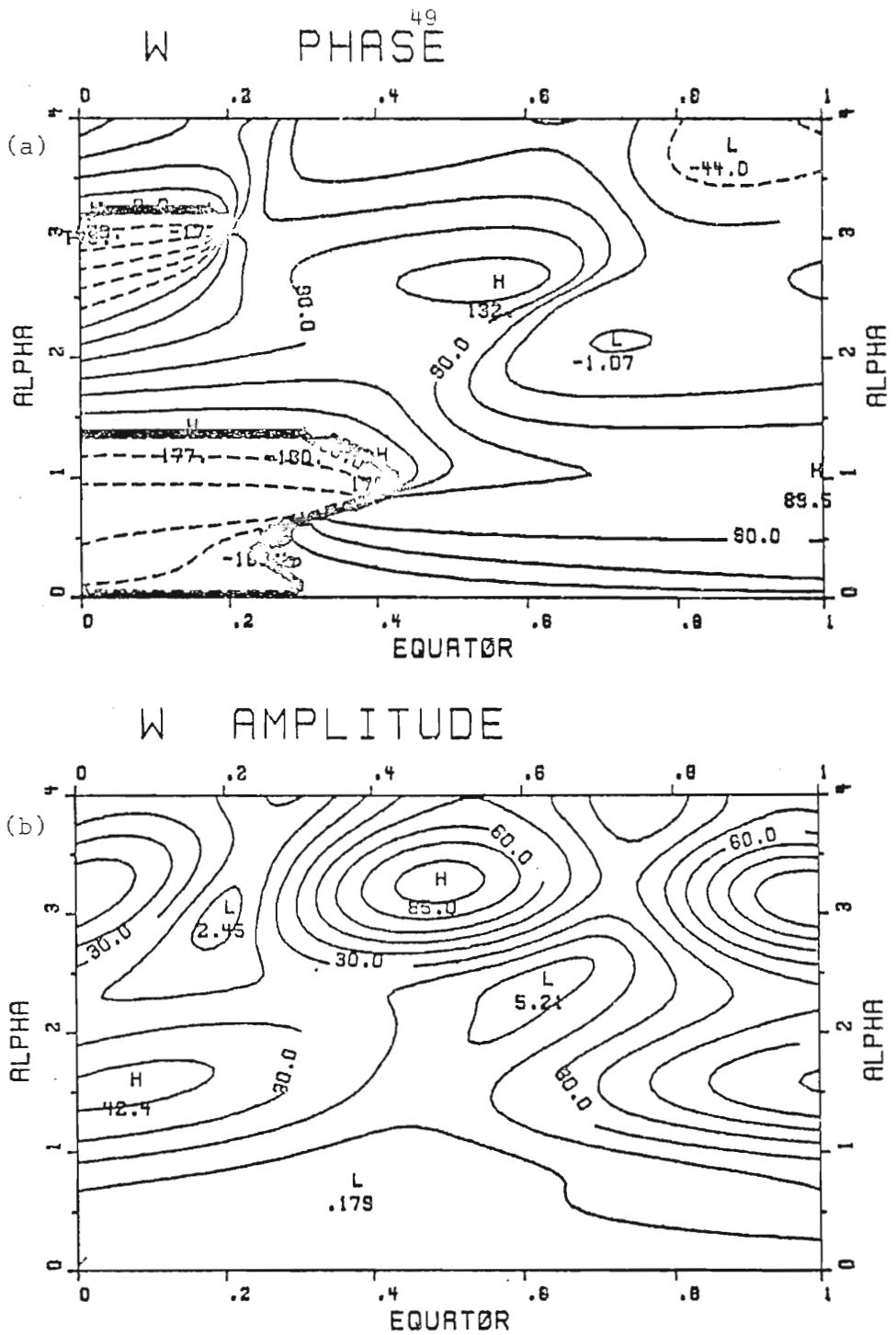

Fig. 12. (a) Phase and (b) amplitude of the vertical motion of the pycnocline along the equator for a case which is forced by a time-variable, uniform, zonal wind stress. The coordinate along the abscissa is non-dimensionalized by the length of the basin. The variable along the ordinate is the non-dimensional parameter α which is given by $\alpha = \omega L/C_K = 2\pi L/C_K T$; hence α increases with decreasing period. The maximum vertical velocity of the model pycnocline occurs at $\alpha = \pi(L = C_K T/2)$ along the eastern boundary (x = 1). The units of the amplitude plot are the percentages of this maximum value. The contour interval for the phase plot (a) is 30°, while for the amplitude plot (b) it is 10%.

n = 0 terms in (21) are used, the resulting amplitude function is that which is shown in Fig. 13. Such an expression includes only one reflection each of the Rossby and Kelvin waves generated directly by the wind stress. The result presents a qualitatively accurate picture of the full expression and, in general, underestimates the true amplitude by no more than 20 percent. For example, at the eastern boundary the amplitude of the vertical velocity oscillation for $\alpha = 1.26$ (which is the value for the annual signal using the parameters in Table 1) is 2.57 W_I, while it is 2.53 W_I when the n = 0 terms are used. The phase also undergoes a small change from 75 to 65 degrees. At the western boundary, though, the error is larger. For the same comparison of terms, the amplitude at the western boundary changes from 1.72 W_I to 1.42 W_I, while the phase changes from -166 to 179 degrees. The addition of only one term, however, can produce a significant improvement, particularly at the western boundary. If we include the W_{KRK} term, that is the Kelvin wave resulting from two reflections of the initial Kelvin wave, then the resultant phase and amplitude plots are shown by Fig. 14. For $\alpha = 1.26$, the amplitude of W is not 1.59 W_I while the phase is -173 degrees. Since it is judged that the plots in Fig. 14 are sufficiently close to those in Fig. 12, the inclusion of more terms is unnecessary.

The equatorial response to an oscillating patch of wind stress may be analyzed in a similar manner. Consider the wind-stress distribution given by (22) in which the forcing has a rectangular pulse shape of width d and its western-most edge is a distance a from the western boundary. If we use the trigonometric identifies, scale x, d, and a by the width d and its western-most edge is a distance a from the western boundary. If we use the trigonometric identifies, scale x, d, and a by the width of the basin, and examine the response to the east of the forced

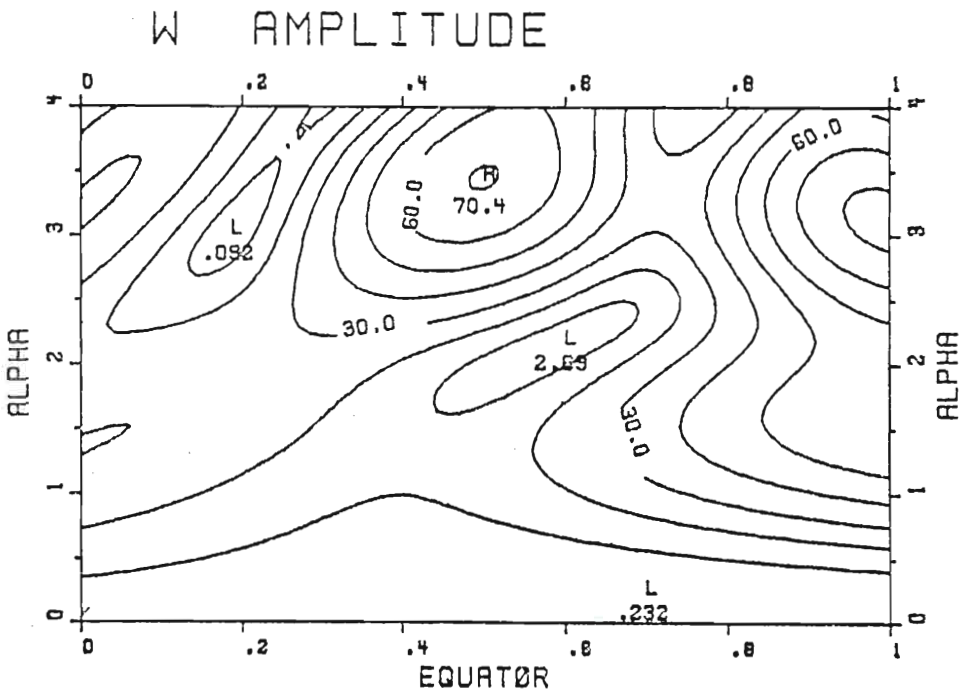

Fig. 13. Same as Fig. 12(b) except that amplitude function includes only the n = 0 terms in the analytical expression (30) (see text).

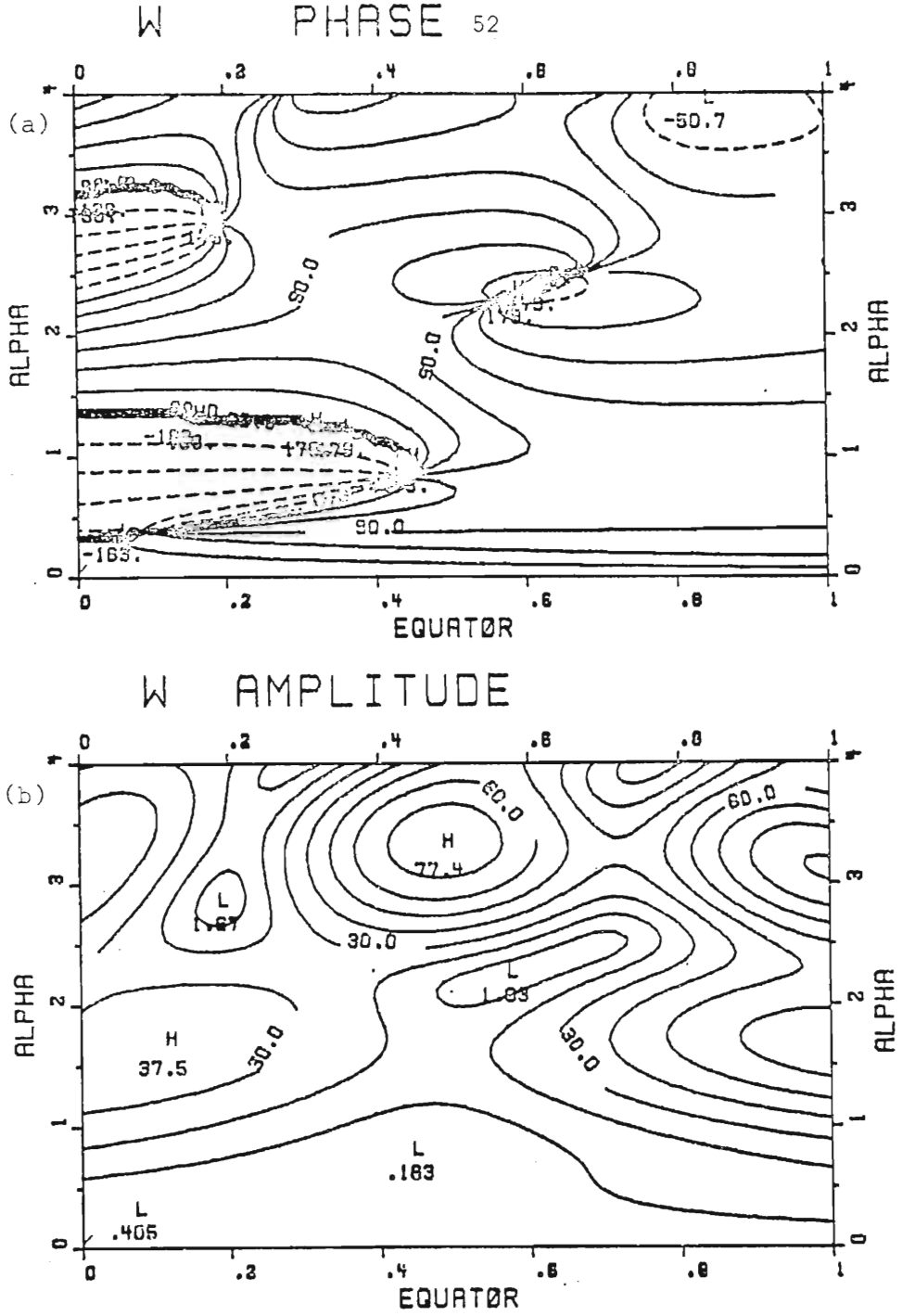

Fig. 14. Same as Fig. 12 except that the analytic espression (30) includes only the n = 0 terms plus the reflection of the initial Kelvin wave, i.e., the W_{KRK} term. The thick line in the phase diagram is due to the bunching of contours when the phase changes sign at $\pm$ 180°.

wave, i.e., the W_{KRK} term. The thick line in the phase diagram is due to the bunching of contours when the phase changes sign at $\pm$ 180°.

region, the expression for the vertical velocity becomes

$$W(x,t) = 2 \sum_{n=0,1} \cos(\omega t + \phi + \alpha(a+\tfrac{d}{2}))[\sin \tfrac{\alpha d}{2} ([R_E R_W)^n W_{IK} \cos((4n+x)\alpha)$$

$$+ (R_E R_W)^n R_E W_{IK} \cos((4n + 1 + 3(1-x))\alpha))$$

$$- \sin \tfrac{3\alpha d}{2} ((R_E)^n R_W W_{IR} \cos((4a + 2d + 4n(1-x))\alpha))] \qquad (31)$$

$$+ \sin(\omega t + \phi + \alpha(a+\tfrac{d}{2}))[\sin \tfrac{d}{2} ((R_E R_W)^n W_{IK} \sin((4n+x)\alpha)$$

$$+ (R_E R_W)^n R_E W_{IK} \sin((4n + 1 + 3(1-x))\alpha))$$

$$- \sin(\tfrac{3\alpha d}{2}) (R_E)^n R_W W_{IR} \sin((4a + 2d + 4n(1-x)))\alpha)]$$

where α retains its previous definition and $x > a + d$. Equation (31) includes only two reflections from the excitation of Rossby waves at the edges of the wind stress. Because the amplitude of the Kelvin wave generated by the wind-stress is approximately seven times the amplitude of the Rossby wave, the effects of the Rossby wave are negligible after two reflections.

If (26) is written in the form

$$W(x,t) = B(x) \sin(\omega t + \phi + (a + \tfrac{d}{2})\alpha)$$

$$+ C(x) \cos(\omega t + \phi + (a + \tfrac{d}{2})\alpha) \qquad (32)$$

then the expression for B(x) and C(x) become:

$$B(x) = 2W_I \sum_{n=0,1} [\ 1.15 \sin(\tfrac{\alpha d}{2})((R_E R_W)^n \sin((4n+x)\alpha)$$

$$+ (R_E R_W)^n R_E \sin((4n + 1 + 3(1-x))\alpha)) \qquad (33)$$

$$-.17 \sin (\tfrac{3\alpha d}{2}) R_E^n R_W \sin((4a + 2d + x + 4n(1-x))\alpha)]$$

$$-.17 \sin (\tfrac{3\alpha d}{2}) R_E^n R_W \sin((4a + 2d + x + 4n(1-x))\alpha)]$$

$$C(x) = 2W_I \sum_{n=0,1} [1.15 \sin(\frac{\alpha d}{2})((R_E R_W)^n \cos((4n + x)\alpha)$$

$$+ (R_E R_W)^n R_E \cos((4n + 1 + 3(1-x))\alpha))$$

$$- .17 \sin(\frac{3\alpha d}{2}) R_E^n R_W \cos((4a + 2d + x + 4n(1-x))\alpha)]$$

where W_{IK} and W_{IR} have been substituted in favor of W_I using (24) and (25). When B(x) and C(x) are written in the form (33) the resulting phase angle

$$\theta(x) = \tan^{-1} C(x)/B(x)) \qquad (34)$$

is not the phase relative to the forcing, but rather part of the phase which depends upon x. The advantage of the form (33) is the revelation that one of the model parameters, a, appears only in the last term in each bracket. It will be shown that these terms may be neglected without producing a significant change in the amplitude of the response.

In Fig. 15, the amplitude and phase functions using (33) and (34) are plotted for the region to the east of a wind-stress patch. Fig. 15 includes all terms in (33) and will be used as the standard for comparison purposes. The close agreement between the linear expression (23) and the numerical model has been demonstrated in Fig. 11. Now, it remains to be shown which terms are required to reproduce the essential results of the linear expression.

If we include only the n = 0 terms in (33), the resultant amplitude function is shown in Fig. 16a. Such an expression includes two reflections of each of the four waves excited by the wind stress. The agreement with the full expression is excellent; the higher reflections are tions of each of the four waves excited by the wind stress. The agreement with the full expression is excellent; the higher reflections are unimportant. The result given by Fig. 16a is essentially reproduced even

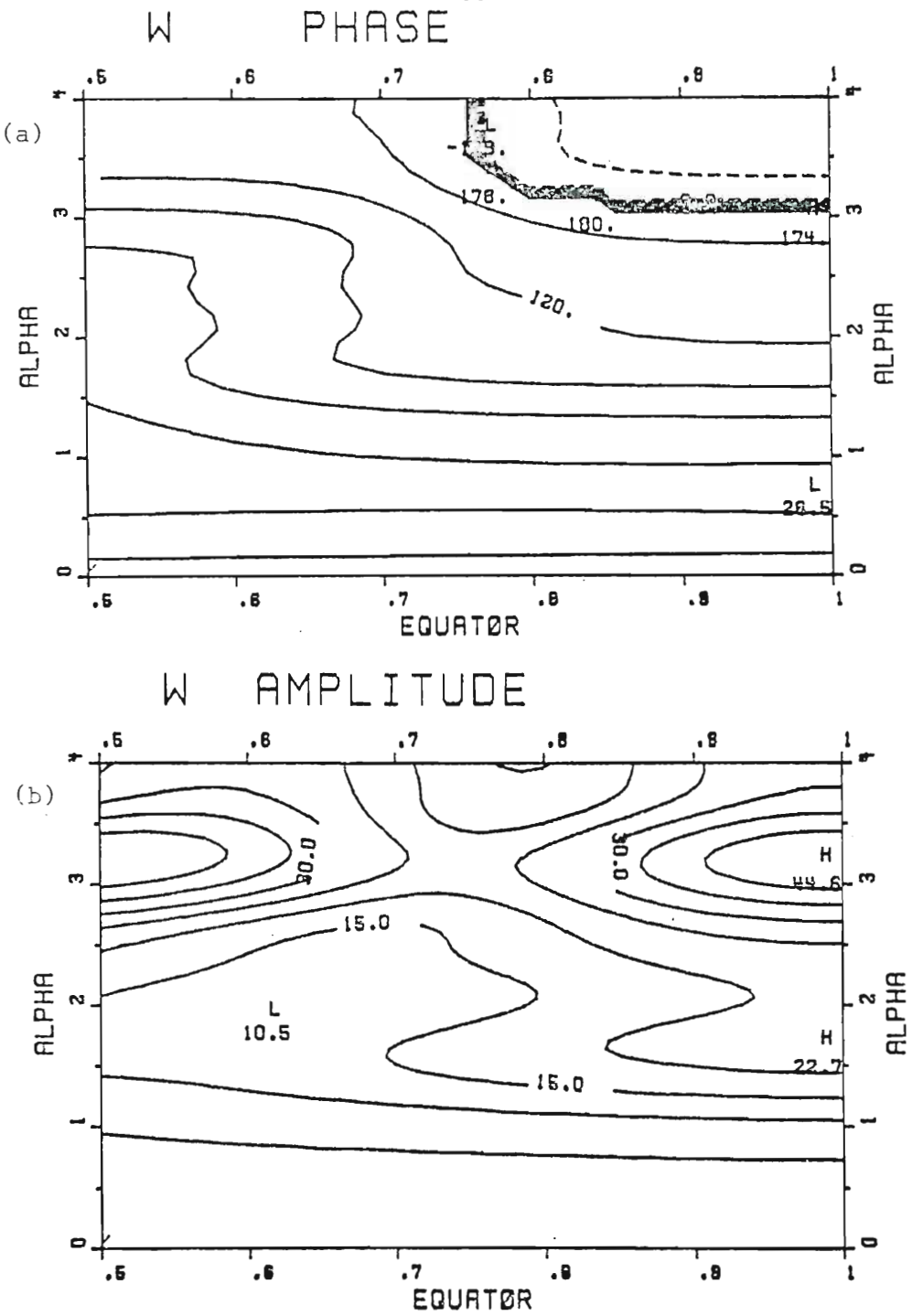

Fig. 15. Phase and amplitude functions for wind stress patch case. The easternmost point of the forced region is at x = .45. The contour interval is 30° for (a) and 5% of maximum for (b) (see Fig. 12). For this plot, a = .15 and d = .3.

Fig. 15. Phase and amplitude functions for wind stress patch case. The easternmost point of the forced region is at x = .45. The contour interval is 30° for (a) and 5% of maximum for (b) (see Fig. 12). For this plot, a = .15 and d = .3.

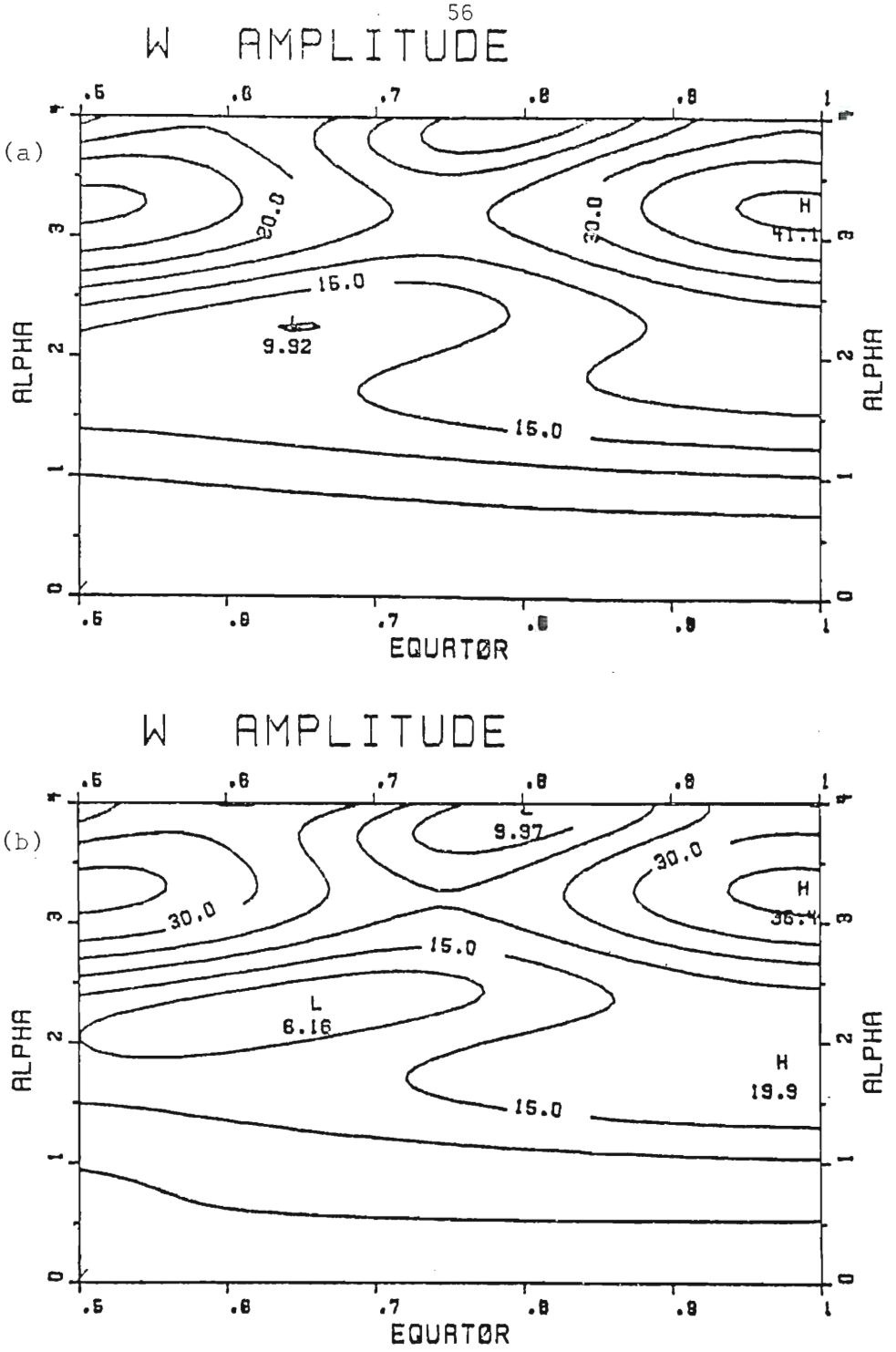

Fig. 16. (a) Same as Fig. 15(b) except that only the n = 0 terms are included, i.e., two reflections each of the Rossby and Kelvin waves generated at edges of forced region. (b) Same as 16(a) except that only Kelvin waves generated at wind stress edges are included.

Fig. 16. (a) Same as Fig. 15(b) except that only the n = 0 terms are included, i.e., two reflections each of the Rossby and Kelvin waves generated at edges of forced region. (b) Same as 16(a) except that only Kelvin waves generated at wind stress edges are included.

if the Rossby waves excited by the wind stress are neglected. The resultant amplitude function, which includes only two reflections of each of the two Kelvin waves, is shown in Fig. 16b. Since the Rossby wave terms are the only ones that contain the parameter a, Fig. 16b reveals that the amplitude function at a given point is essentially independent of the location of the wind stress patch provided one is east of the forcing. The total phase of the response with respect to that of the forcing, however, does depend upon the position relative to the forced region.

The amplitude of the Kelvin waves generated directly by the wind stress are so much larger than any other waves, they dominate the solution to the east of the forcing. Thus, the inclusion of only these waves and their reflections from the eastern boundary are sufficient to produce a fairly good approximation to the full solution. Fig. 17 is a comparison of solutions for a case in which the parameters are identical to the case in Fig. 11 except that the distance of the patch from the western boundary, a, is set to .15 instead of .53. In Fig. 17a, the $n = 0$ terms have been included, while in Fig. 17b, the reflection coefficient at the western boundary, R_W, has been set of zero. Hence, only the Kelvin waves and their first reflection affect the eastern region. The agreement between the two solutions is quite good. At the eastern boundary there is a slight phase shift of about 30 degrees, but the amplitudes agree to within twenty percent. The importance of this result will be discussed in the subsequent chapter when these expressions are applied to the study of observations in the equatorial Pacific.
be discussed in the subsequent chapter when these expressions are applied to the study of observations in the equatorial Pacific.

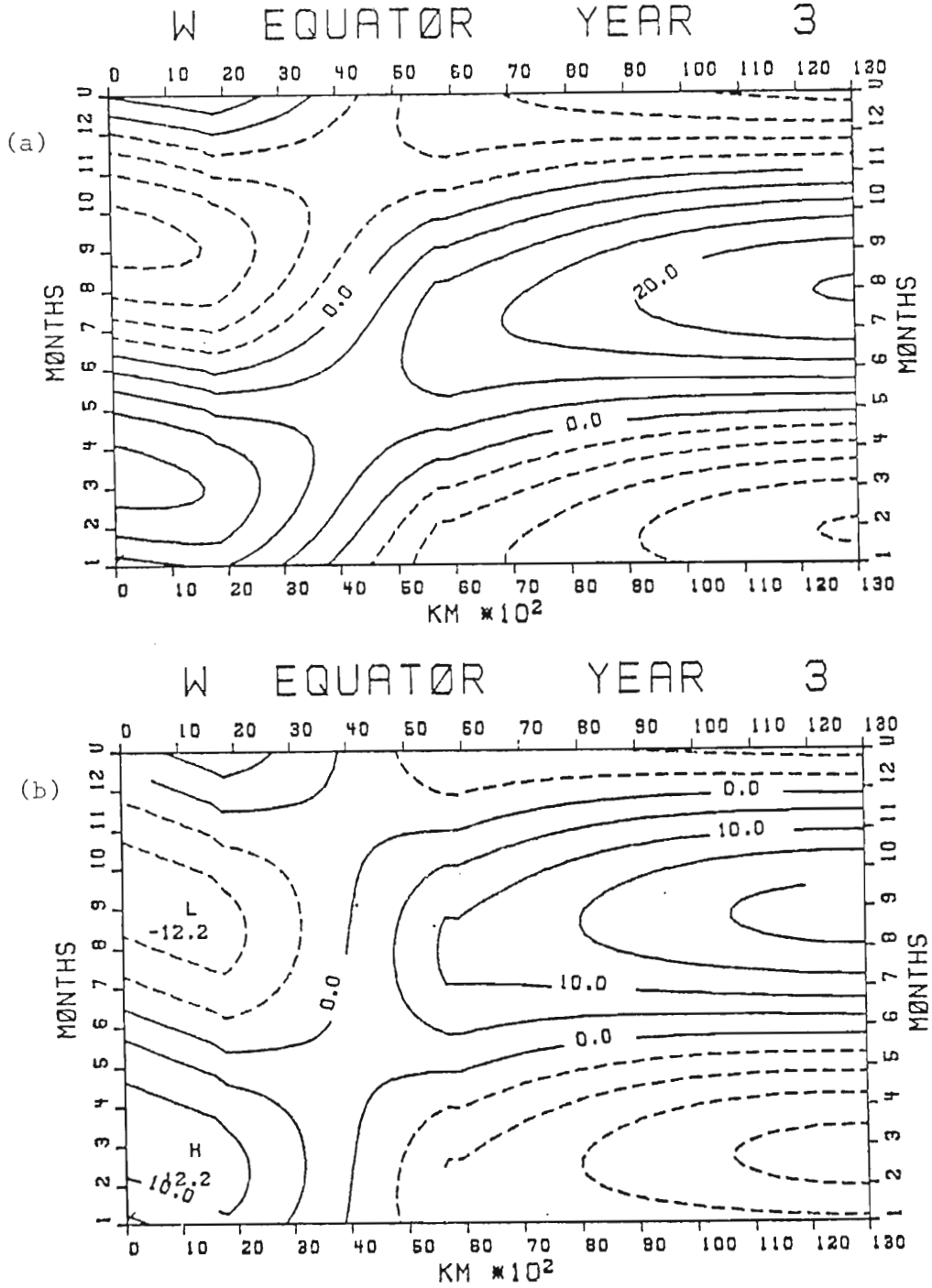

Fig. 17. Comparison of results of analytic expression for wind stress patch case in which (a) only the n = 0 terms have been included and (b) the reflection coefficient at the western boundary, R_W, has been set to zero. For this case, the values of the parameters a and d are .15 and .3, respectively.

stress patch case in which (a) only the n = 0 terms have been included and (b) the reflection coefficient at the western boundary, R_W, has been set to zero. For this case, the values of the parameters a and d are .15 and .3, respectively.

b. Amplitude Maximum at Eastern Boundary

The expressions for the amplitude and phase as shown in Figs. 12, 15 may also be utilized to examine the general nature of the equatorial response to variable winds. One of the most prominent features of the amplitude plots is the maximum along the eastern boundary for all values of the parameter α. There are essentially two reasons for this. The first is associated with the familiar concept that the maximum amplitude of a vibrating string, say, occurs at the free end(s). It is at this point that the incident and reflected waves are perfectly in phase. Since both the eastern and western boundaries are free with respect to the height field, we must examine the phase of the response in order to understand the strong asymmetry.

The amplitude function (Fig. 18b) is essentially symmetric about the mid-point of the basin. The asymmetry of the total response is caused by the phase relationship between the forced interior motion and the free wave solution. It is evident from Fig. 18a that the response at the eastern boundary is much more in phase with the wind stress than that at the western boundary. At $\alpha = 0$, the "wave" solution is uniform across the basin, has a value of W_I (21% contour value) and is 180° out of phase with the forced motion. This is the steady state solution. However, for non-zero values of α, the solution and the interior response always combine to produce the largest resultant amplitude at the eastern boundary. When the wave amplitude is at a maximum value, the western boundary response is 180° out of phase with the wind stress.

A somewhat more simplified viewpoint of the above situation can be the western boundary response is 180° out of phase with the wind stress.

A somewhat more simplified viewpoint of the above situation can be stated in terms of the Rossby and Kelvin waves generated at the boundar-

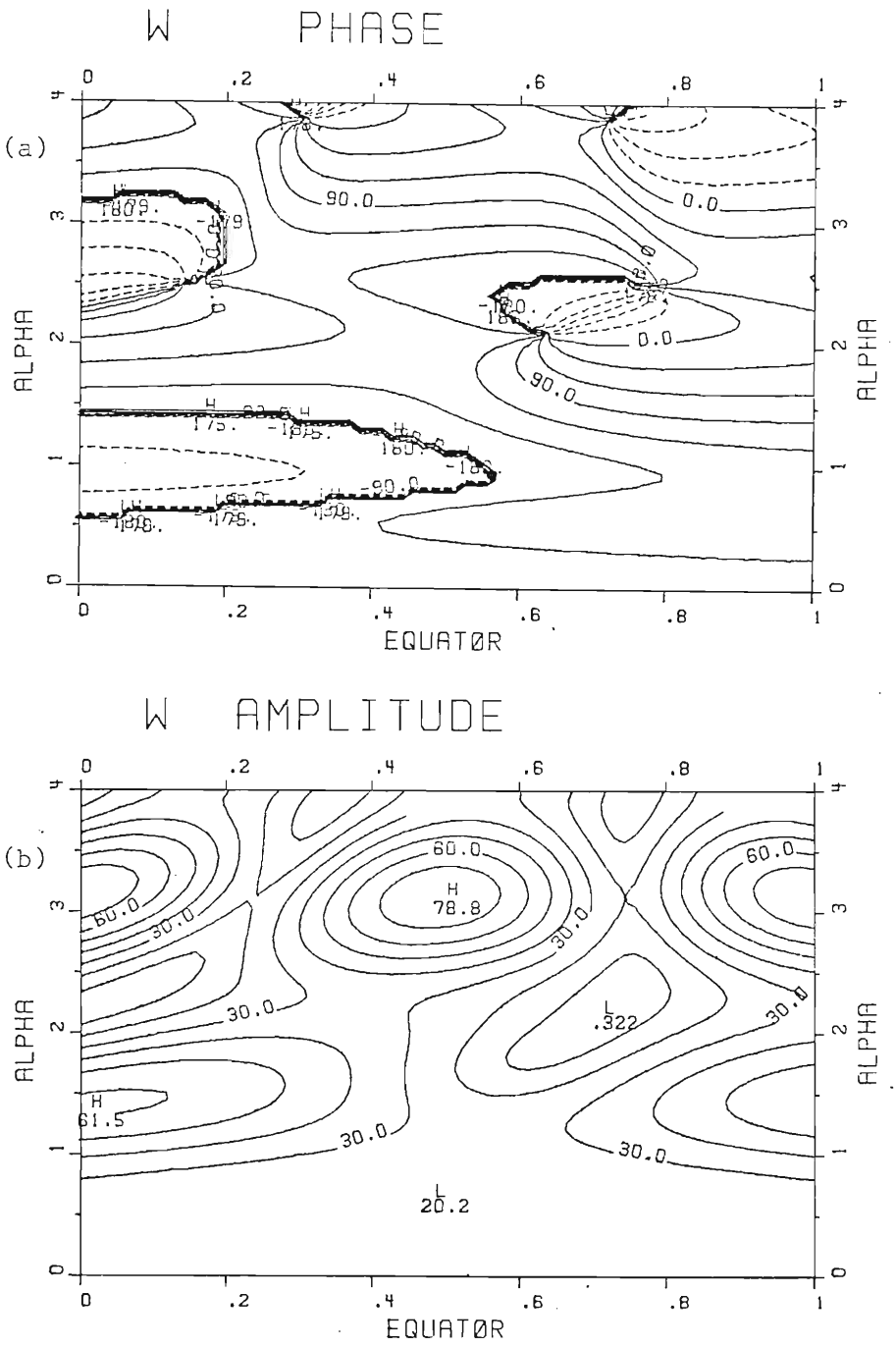

Fig. 18. Same as Fig. 12 except that the forced interior response has been removed; hence, this figure shows the response of the pycnocline due to the effects of the equatorially trapped waves only.

has been removed; hence, this figure shows the response of the pycnocline due to the effects of the equatorially trapped waves only.

ies. The Kelvin wave generated by the wind stress is 180° out of phase with the wind at the western boundary, whereas the Rossby wave is in phase with the wind at the eastern boundary. When the incident waves reinforce the waves generated at the boundaries, the response is reduced by the wind at the western boundary but amplified by the wind at the eastern boundary.

Although for slightly different reasons than above, the maximum amplitude of the vertical velocity also occurs at the eastern boundary when the wind stress is confined to the interior region. The asymmetry in this case is caused by the larger amplitude incoming waves at the eastern boundary than at the western boundary; the Kelvin wave affects the western boundary only after reflection. For higher values of α, though, there may be interior regions east of the wind stress with comparable amplitudes to that at the eastern boundary. That is, if the waves have a short enough wavelength, the Kelvin wave and reflected Rossby wave could constructively interfere at interior points as well.

c. Dependence of Amplitude Function on Model Parameters

For the case in which the wind stress extends across the entire basin, the amplitude and phase of the response depend upon one parameter, α, which is given by

$$\alpha = \frac{\omega L}{C_K} = \frac{2\pi L}{C_K T}$$

As stated earlier, this is the fraction of 2π radians given by the ratio of the basin width to the wavelength of the Kelvin wave. The maximum amplitude occurs for $\alpha = \pi$, with a secondary maximum at $\pi/2$; the minimum response occurs at $\alpha = 3\pi/4$. At $\alpha = \pi$, the basin width, L, is half the

wavelength of the Kelvin wave. This is the resonant condition for the system; at the boundaries, all the waves and reflected waves are perfectly in phase. A wave initiated at a boundary arrives at the opposite boundary 180° out of phase from when it started. Subsequently, when the reflected wave returns to its origin, it is in phase with the other waves. At the secondary maximum point ($\alpha = \pi/2$), the reflected wave again returns to the original boundary with the same phase as when it began. However, at the opposite boundary, it was 90° out of phase with the wind stress. Hence the resultant amplitude is not as large as the $\alpha = \pi$ case.

The wind-stress patch case also has a maximum response at $\alpha = \pi$, $\pi/2$. For this type of wind stress, however, an additional parameter is introduced, i.e., the width of the forced region, d. The effect of the longitudinally bounded wind stress is to increase the value of α for which the maximum response is obtained. It was shown earlier that we can neglect the Rossby waves excited at the edges of the forcing without significantly changing the amplitude of the response (Fig. 16b). Using this approximation, (33) shows that the effect of the wind stress confinement is to modulate the response via the term

$$\sin \frac{\alpha d}{2}$$

which reaches its first maximum at

$$\alpha d = \pi.$$

Since $d < 1$, the maximum amplitude of the free wave solution is shifted to higher values of α than for the basin-forced case.

Since $d < 1$, the maximum amplitude of the free wave solution is shifted to higher values of α than for the basin-forced case.

Let us now consider the dependency of the equatorial response on such model parameters as the width of the basin, L, the period, T, and the Kelvin wave speed, C_K. For a given value of the wind stress and C_K, the amplitude and phase depend upon the ratio

$$L/T.$$

Hence, the Atlantic and Indian Oceans, which are one third the width of the Pacific, would have the same response as the Pacific if the period of the wind stress is also one third of that in the Pacific. It should be noted here, that while the amplitude of the vertical velocity depends only on α, the amplitude of the thermocline displacement depends additionally on the period. That is, for an adiabatic process and a constant vertical velocity in each case, the thermocline displacement for the annual forcing would have twice the displacement as for the semi-annual period. As will be discussed below, however, this fact is frequently offset by the tendency of the vertical velocity amplitude to increase with decreasing period.

The results of this work agree with Philander (1979a) who stated that, at the equator, the annual response in the comparatively smaller Atlantic would be close to the equilibrium condition, whereas in the Pacific the response to the annual forcing would have a more wavelike solution. If we assume a width of 15,000 km for the Pacific and 5,000 km for the Atlantic and use the parameters in Table 1, then the value of α for the annual period is approximately 1.5 in the Pacific and .5 in the Atlantic. Fig. 13 shows that at α = .5, the solution is essentially in equilibrium with the wind stress. The response is virtually symmetric
the Atlantic. Fig. 13 shows that at α = .5, the solution is essentially in equilibrium with the wind stress. The response is virtually symmetric

about the mid-point of the basin. In such a case, the thermocline slope would be in phase with the wind. At $\alpha = 1.5$, however, a pronounced asymmetry is shown; the thermocline slope is no longer in balance with the local wind. Philander also suggests that this is the reason for the large seasonal signal in the Atlantic compared with that of the Pacific. This hypothesis is not supported by Fig. 13, which shows that a wavelike response generated by a basin-wide wind stress with an annual period would produce a much greater response in the Pacific than in the Atlantic, particularly at the eastern boundary.

The most probable cause of the larger seasonal signal in the Atlantic is that the zonal wind stress has a larger annual amplitude in that basin. Bunker (Katz et al., 1977) has shown that the annual period wind in the equatorial Atlantic has an average amplitude of approximately .15 dynes cm^{-2} which is superimposed on a mean value of approximately .4 dynes cm^{-2}. The average is calculated between 10°W and 40°W. In the Pacific, Meyers (1979b) shows that the annual signal varies between .1 and .02 dynes cm^{-2} with a mean value similar to that in the Atlantic.

It is interesting to note that a given size patch of oscillating wind, with all other factors being equal as well, will generate a comparable amplitude response to the east of the forcing in the Atlantic as in the Pacific. This is in contrast to the basin-wide forcing case for which we saw that the Pacific response would be much larger than that in the smaller Atlantic. Fig. 19 shows that for a region of wind stress 3,000 km wide (d = .2 in the Pacific, Fig. 19a; d = .6 in the Atlantic, Fig. 19b) and having an annual period, the amplitudes east of the wind 3,000 km wide (d = .2 in the Pacific, Fig. 19a; d = .6 in the Atlantic, Fig. 19b) and having an annual period, the amplitudes east of the wind stress for the respective values of α are about equal.

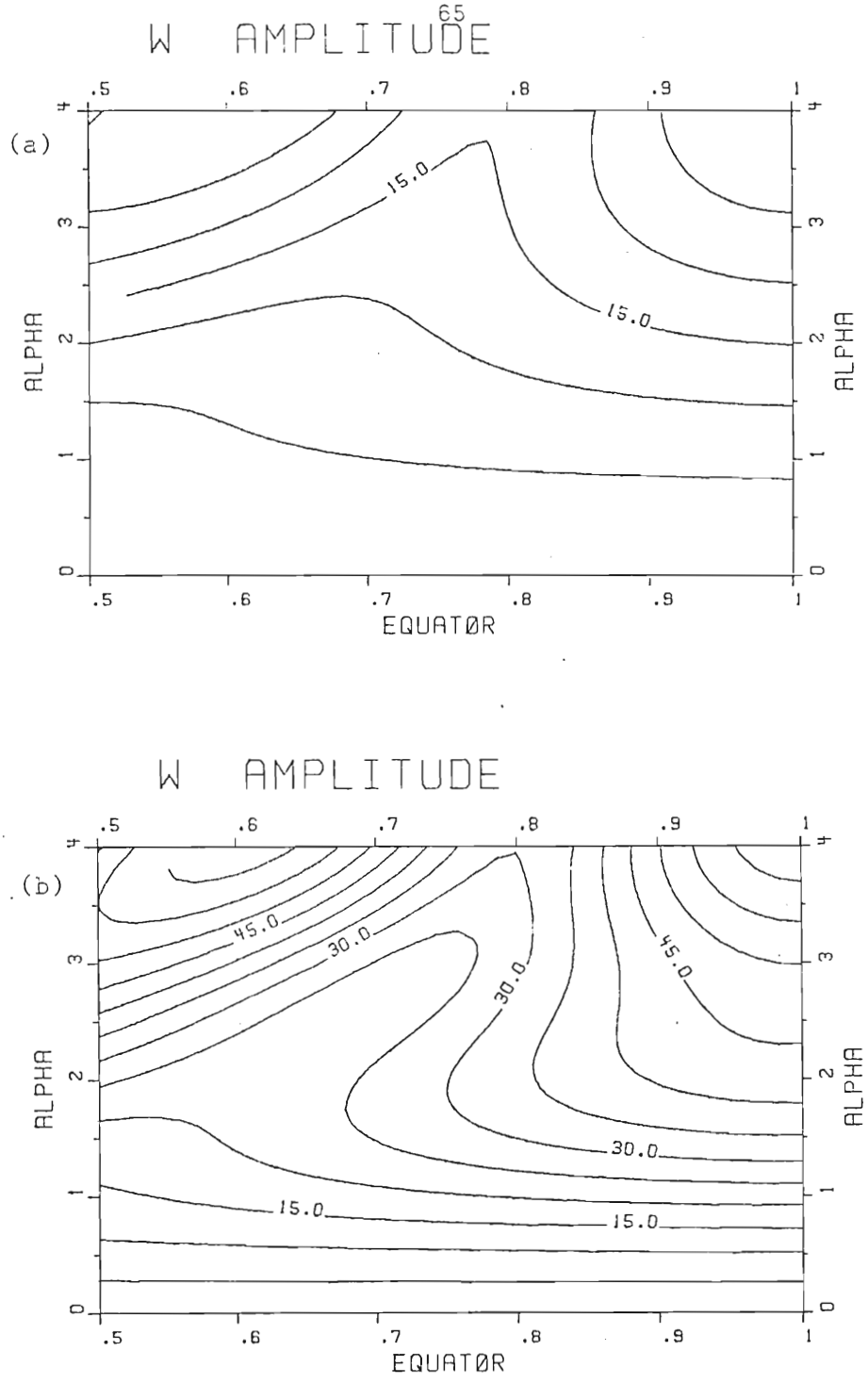

Fig. 19. Comparison of amplitude of W for 3,000 km wide wind stress patch in (a) Pacific and (b) Atlantic. The value of α for the first baroclinic mode with annual periodicity is 1.5 in the Pacific and .5 in the Atlantic.

stress patch in (a) Pacific and (b) Atlantic. The value of α for the first baroclinic mode with annual periodicity is 1.5 in the Pacific and .5 in the Atlantic.

The amplitude of the response as a function of period only can be seen both in Fig. 14b and 16b. In general, there is an increase in the amplitude of the vertical velocity with decreasing period. For example, if we use the values of C_K and L given above, the value of α for the annual period in the Pacific is approximately 1.5, while it is about 3.0 for the semi-annual period. As discussed earlier, these value are close to those for which the amplitude response at the boundaries is maximized. Cane and Sarachik (1977) suggest that the annual response in the Pacific may be enhanced because the time for a round trip in that basin is close to the annual period. As mentioned above, this period corresponds to the value of $\alpha = \pi/2$ in the Pacific. Although we would also predict an amplification of the annual period, it is the semi-annual period ($\alpha \simeq \pi$) which is most amplified in the Pacific.

For a given basin width and period of the forcing, the parameter α depends upon the phase velocity of the Kelvin wave. Since the formulation we have employed is valid for any baroclinic mode, the vertical eigenvalues, C_K, can differ appreciably. The amplitude of the forcing projected onto the second baroclinic mode can be non-negligible (Moore and Philander, 1977); hence it is of interest to examine the differences in the responses between the first and second baroclinic modes.

For the equatorial mode analyses described by Moore and Philander (1977) and Cox (1976), the phase speed of the Kelvin wave for the second baroclinic mode is a factor of approximately 1.7 smaller than that of the first mode. Such changes in the value of α can produce a significant effect on the amplitude of the solution. For example, Fig. 12b

the first mode. Such changes in the value of α can produce a significant effect on the amplitude of the solution. For example, Fig. 12b (the case for which the wind extends across the basin) shows that an

increase in α of magnitude 1.7 could either increase or decrease the response relative to the first baroclinic mode. In both the Atlantic and Indian Oceans, the annual and semi-annual responses of the second baroclinic modes would be larger than otherwise expected. Depending upon one's choice of parameters, the opposite may be true for the Pacific.

It should be pointed out here, however, that the applicability of these results to the study of the real ocean depend, in part, upon the nature of the interaction between the wave field and the mean flow. For equatorial motions, the interaction between the Undercurrent and equatorially trapped waves is of primary interest. Two recent theoretical studies (McPhaden and Knox, 1979; Philander, 1979b) indicate that the Undercurrent has little effect on the first baroclinic mode Kelvin wave at low frequencies; the speed of the Undercurrent is too low and its width is too narrow to produce a significant modification. The effects of the Undercurrent increase with increasing vertical mode, since both the phase speed and latitudinal extent of the waves decrease. Except for some Doppler shifting, the very low frequency Kelvin waves in the second baroclinic mode do not appear to be seriously affected by the Undercurrent. McPhaden and Knox do not examine the modification of Rossby waves. Philander does not explicitly examine the effects on first baroclinic mode Rossby waves emanating from the eastern boundary except to say that they would slow down, increase their latitudinal scale and lose some energy to extra-equatorial regions. The higher mode Rossby waves may be affected more seriously by the Undercurrent.
scale and lose some energy to extra-equatorial regions. The higher mode Rossby waves may be affected more seriously by the Undercurrent.

5. SEASONAL VARIABILITY IN THE EASTERN EQUATORIAL PACIFIC

In this section, both the numerical and analytical models are utilized to examined the seasonal variation of the thermal structure and the circulation of the equatorial Pacific Ocean. Attention is focused on the remote forcing due to equatorially trapped waves. In particular, theoretical evidence is presented which supports the hypothesis of Meyers (1979b) that remote forcing may be responsible for the large semi-annual component of the vertical motion of the thermocline in the eastern equatorial Pacific.

a. Description of Observational Work

A recent paper by Meyers (1979b) presents a very interesting analysis of the seasonal variation of the 14°C isotherm in the equatorial Pacific. Bathythermographic data taken over many years between 2°S-2°N were used to determine the mean depth of the 14°C isotherm as well as the mean monthly variation. Meyers shows that 1) the 14°C isotherm is located in the lower portion of the thermocline, 2) variation of temperature within the depth range spanning the thermocline is due primarily to vertical motion of the thermocline rather than variation of the temperature gradients within it; and 3) vertical motion of the 14°C isotherm is essentially in phase with the vertical motion of the thermocline.

A scatter diagram of the observations of the depth of the 14°C isotherm averaged between 1°S to 1°N is shown in Fig. 20. The east-west

A scatter diagram of the observations of the depth of the 14°C isotherm averaged between 1°S to 1°N is shown in Fig. 20. The east-west

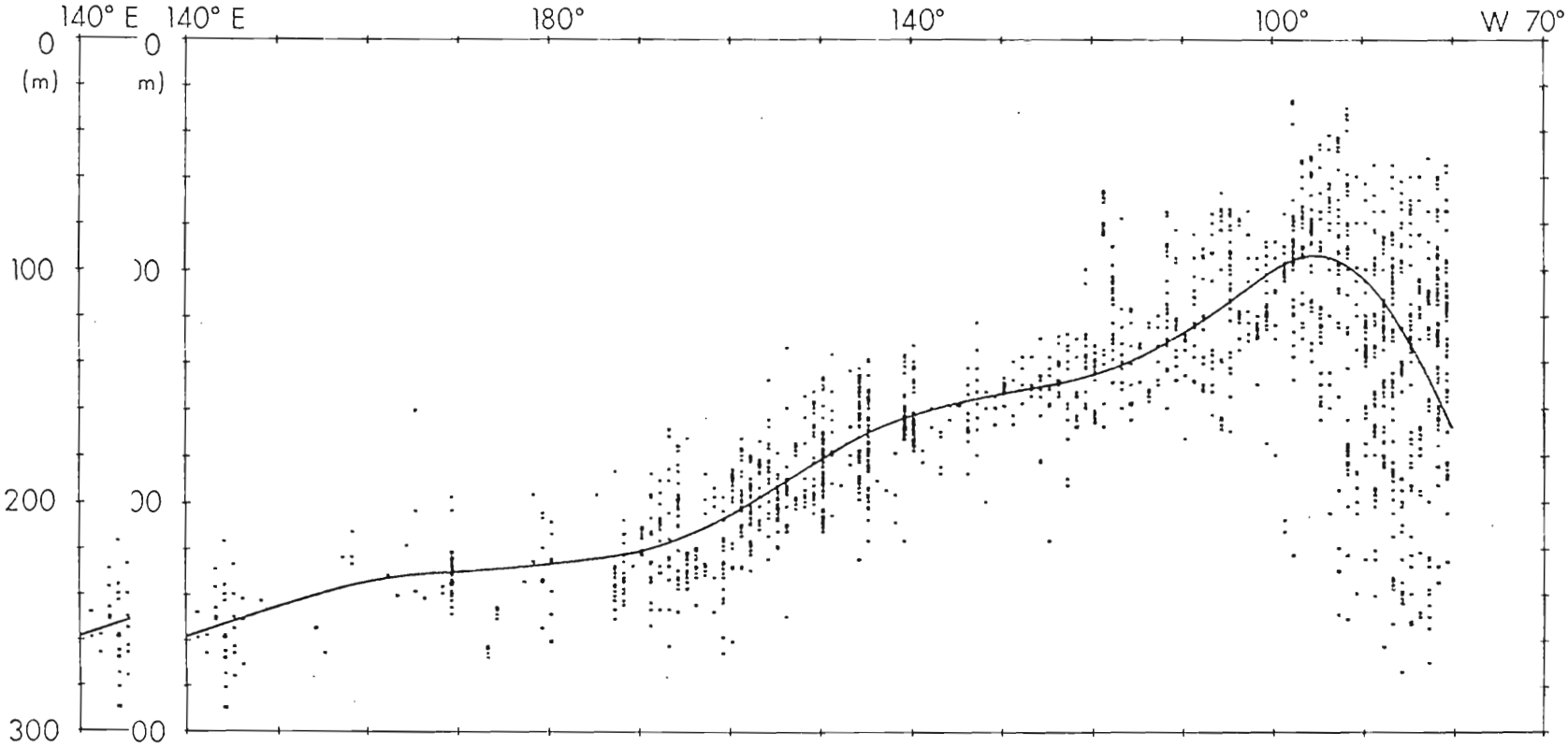

Fig. 20. Scatter diagram of the observations of the depth of the 14°C isotherm between 1°S to 1°S to 1°N in the Pacific Ocean (from Meyers, 1979b).

slope of the mean position of the isotherm is representative of the slope of the thermocline along the equator. The most striking aspect of this plot is the large amplitude of the depth variations near the eastern boundary. The extreme values are due to the large El Niño events. However, even if one considers the region over which the distribution of data points is rather uniform, the largest amplitude is at the eastern boundary. As was shown in the preceding section, the eastern boundary is consistent with the hypothesis that remote forcing mechanisms are operant in the eastern equatorial Pacific.

In order to study the seasonal variability of the thermocline, Meyers averaged the data over areas of 20° longitude (± 2° about the equator) and calculated mean monthly values. Then for each region between 80°W and 140°E, he determined the mean depth as well as the annual and semi-annual signals. A similar analysis was performed on the zonal component of the wind stress between 2°S to 2°N. The results of these calculations are shown in Fig. 21. Note that both the annual and semi-annual components of the 14°C isotherm depth variation have a maximum amplitude at the eastern boundary. This is particularly impressive in view of the fact that the semi-annual component of the wind stress has virtually no amplitude in that region. This is what led Meyers to suggest that remote forcing may be responsible for the large amplitude of the semi-annual component of the vertical displacement of the thermocline at the eastern boundary.

In the following sections, the dynamical causes of the variation of the 14°C isotherm at the eastern boundary are examined in an effort

In the following sections, the dynamical causes of the variation of the 14°C isotherm at the eastern boundary are examined in an effort to test Meyers' hypothesis. The mean seasonal variation of the isotherm

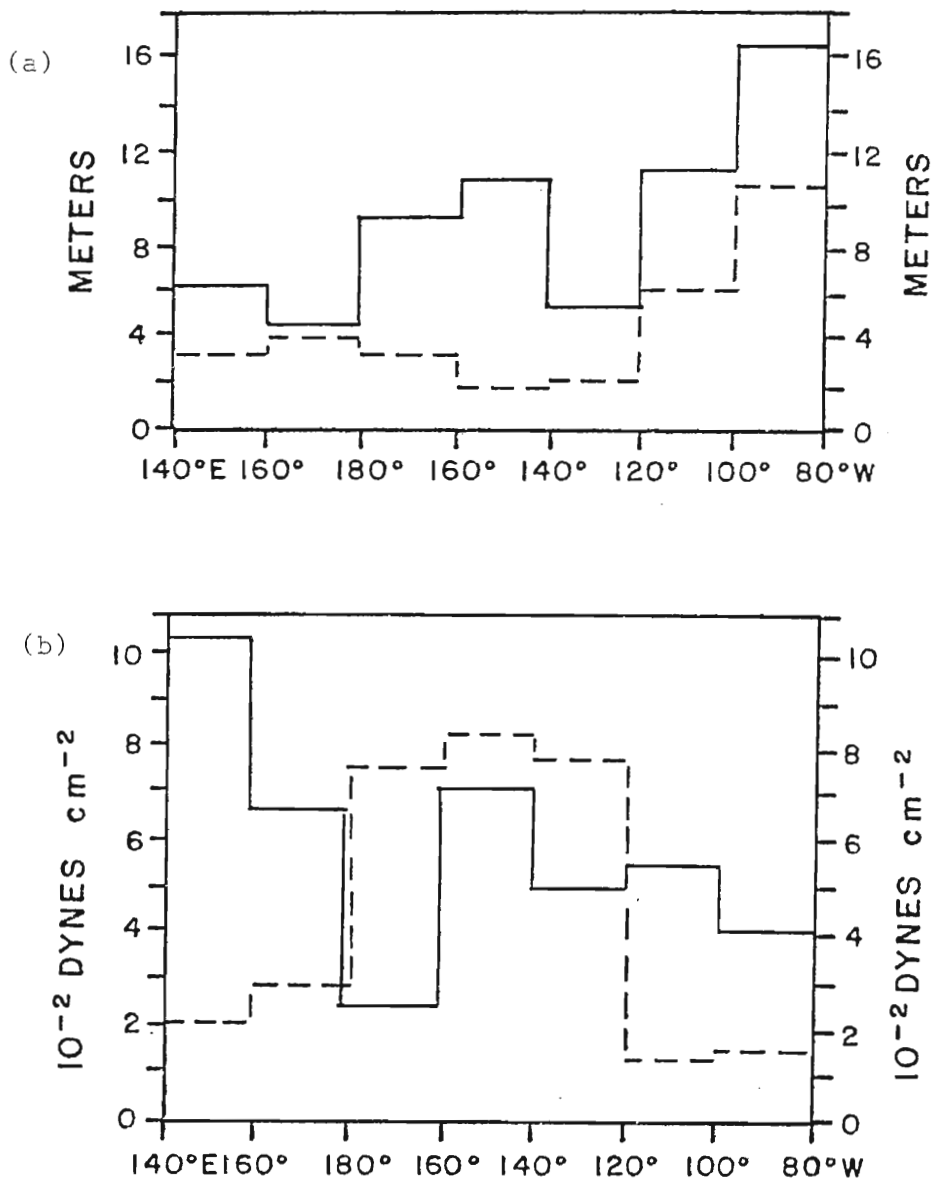

Fig. 21. Comparison of amplitudes of the annual (solid line) and semi-annual (dashed line) components of (a) vertical displacement of 14°C isotherm in the equatorial Pacific and (b) the zonal equatorial wind stress across the entire Pacific (from Meyers, 1979b). The data are averaged over 20° of longitude.

wind stress across the entire Pacific (from Meyers, 1979b). The data are averaged over 20° of longitude.

at the boundary is shown in Fig. 22a. Note that the downwelling initiated in March is representative of a mini-El Niño. The corresponding vertical motion of the isotherm is plotted in Fig. 22b.

b. Numerical Model Results

The mean and seasonal components of the equatorial zonal wind stress as analyzed by Meyers (1979b) are used to force the numerical model. The winds are assumed to have no meridional variation. This is not a serious deficiency; the variation of the wind stress outside of the equatorial radius of deformation ($\sim$ 250 km) has little effect on the near equatorial response (McCreary, (1976)). Meyers also found that the zonal winds in the near equatorial region were distributed symmetrically. Within each of the seven regions between 144°E and 80°W, the winds are assumed to be uniform.

The model parameters for the numerical simulations are those found in Table 1, except that the initial layer depth, H, and the density difference, $\rho_2 - \rho_1$, are set to 200 meters and $2\sigma_t$ units respectively. The model is started from rest and run for four years in order to remove all transients initiated by the spin-up process. All solutions shown in this section are from year four.

The model PHA is now defined as the departure of the interface from its mean position. The comparison of the seasonal variation of the model PHA with the observed variation is shown in Fig. 23. Considering the simplicity of the model, the close agreement is remarkable.

It now remains to determine the dynamics of the variation of the

It now remains to determine the dynamics of the variation of the

model pycnocline at the eastern boundary in order to examine the credibility of such a response in the real ocean.

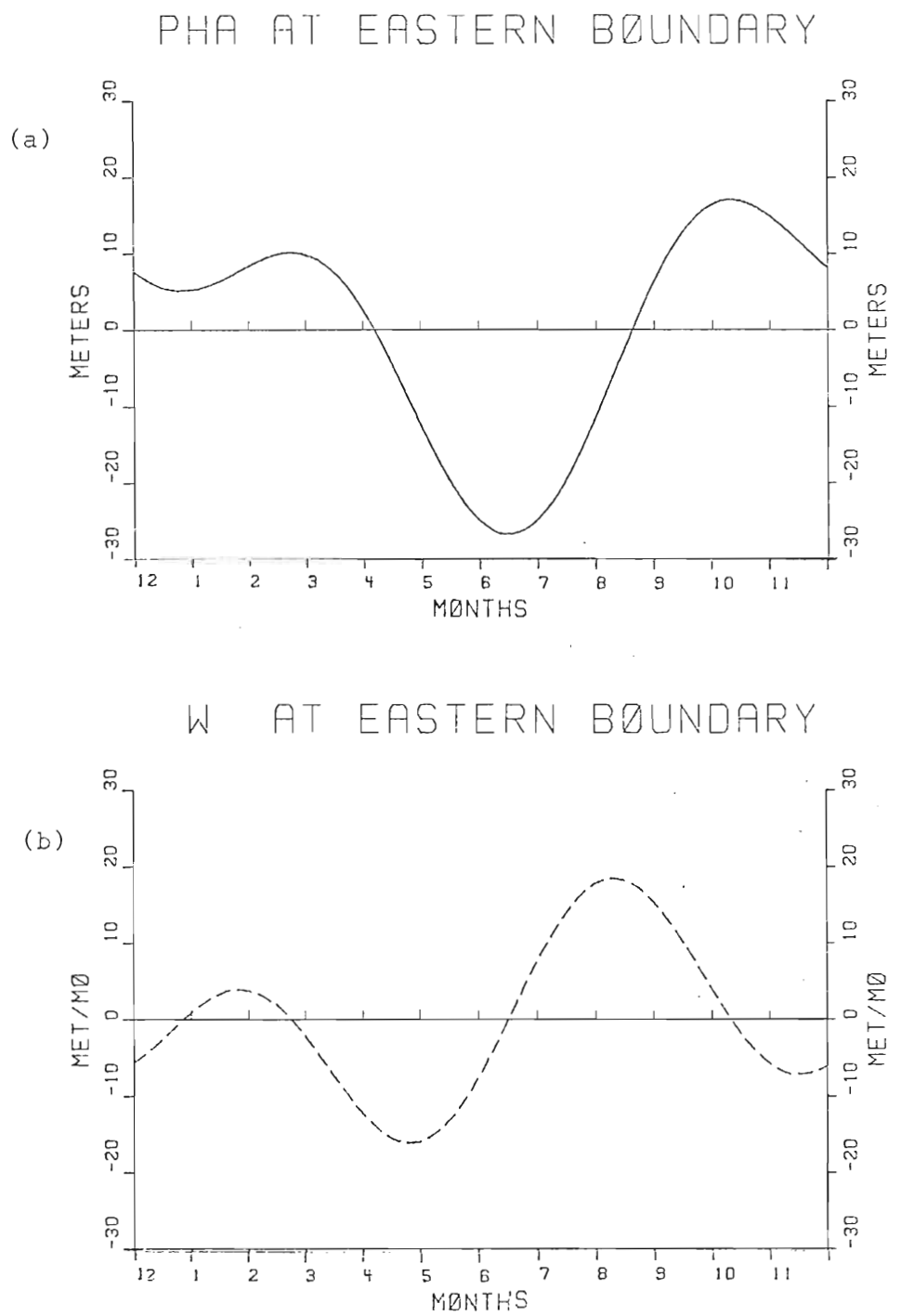

Fig. 22. (a) Time series of the seasonal vertical displacement of the 14°C isotherm from its mean position in the region of 80°W to 100°W at the equator. (b) The corresponding rate of displacement of this iso-

Fig. 22. (a) Time series of the seasonal vertical displacement of the 14°C isotherm from its mean position in the region of 80°W to 100°W at the equator. (b) The corresponding rate of displacement of this iso-therm. The tick marks along the abscissa designate the mid-points of months. The plot begins in mid-December. Positive values in (b) indicate upwelling. (Data from Meyers, 1979b).

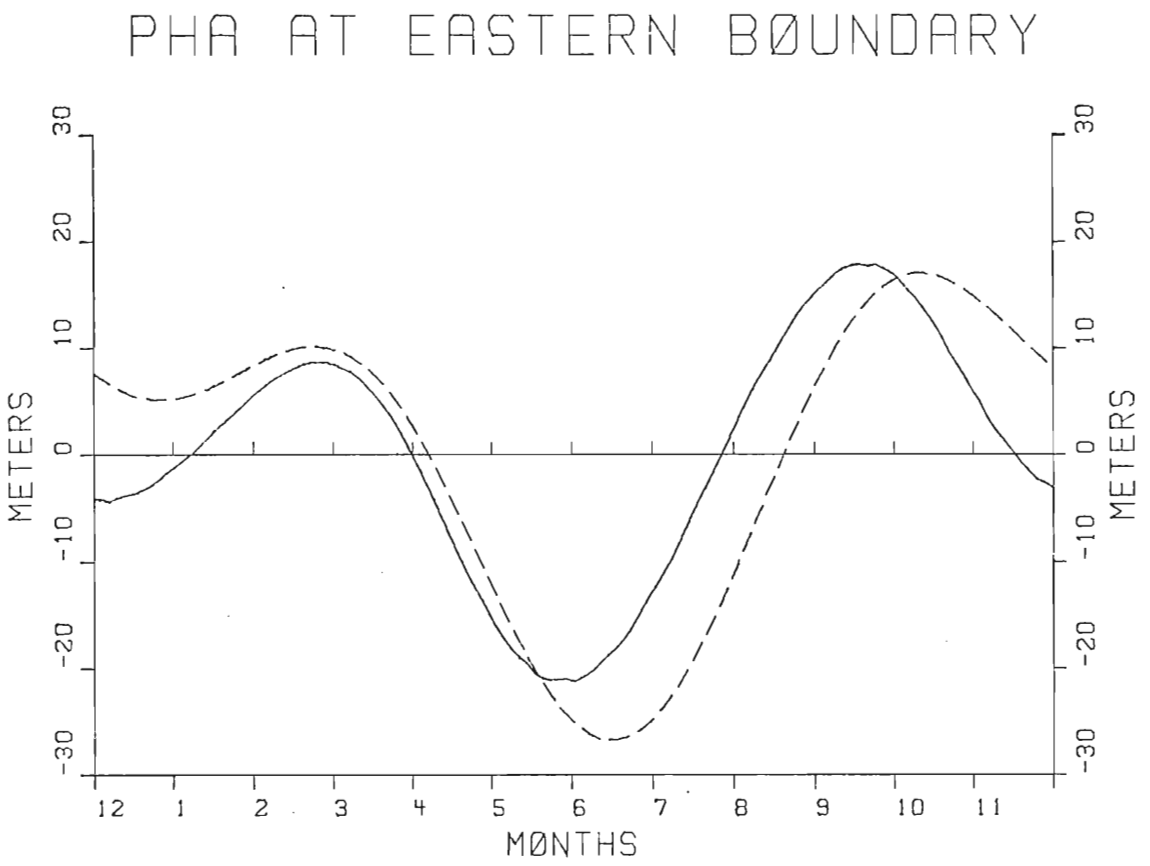

Fig. 23. Comparison of nonlinear numerical model solution (solid line) with observations (dashed line) as shown in Fig. 22(a). The numerical solution is shown for the fourth year of integration.

In order to examine the model results in detail, it is desirable to use the concepts pertaining to the linear response to time-variable winds developed in Sections 3 and 4. Hence, it is necessary to determine whether the model results are inherently nonlinear or rather the result of nonlinear modification to linear dynamics. Therefore, the linear version of the model was run using the identical parameters as in the nonlinear case. The comparison between the linear results and observations is shown in Fig. 24. Although the comparison isn't quite as close as the nonlinear case, the essential features are still present. The larger amplitude response in the nonlinear case is probably due to the nonlinearity of the wind stress term in regions where the layer thickness is less than the initial thickness. The phase differences between the two cases is most probably due to the nonlinear dispersion of the equatorial waves. The essential point, though, is that the linear model can reproduce the basic properties of the response. Hence, the linear response can be examined in more detail by using the analytical expressions developed in Section 3.

c. Analytical Model Results

The wind stress applied in the numerical runs is composed of fourteen wind stress patches as defined in Section 3d, i.e., there are two components of the wind stress in each of the seven regions. Hence, by the principle of superposition, the sum of the fourteen solutions of the analytical model should reproduce the linear numerical results. These calculations, which were performed using all terms in (23), are shown in comparison to the numerical results in Fig. 25a. The agreement is very

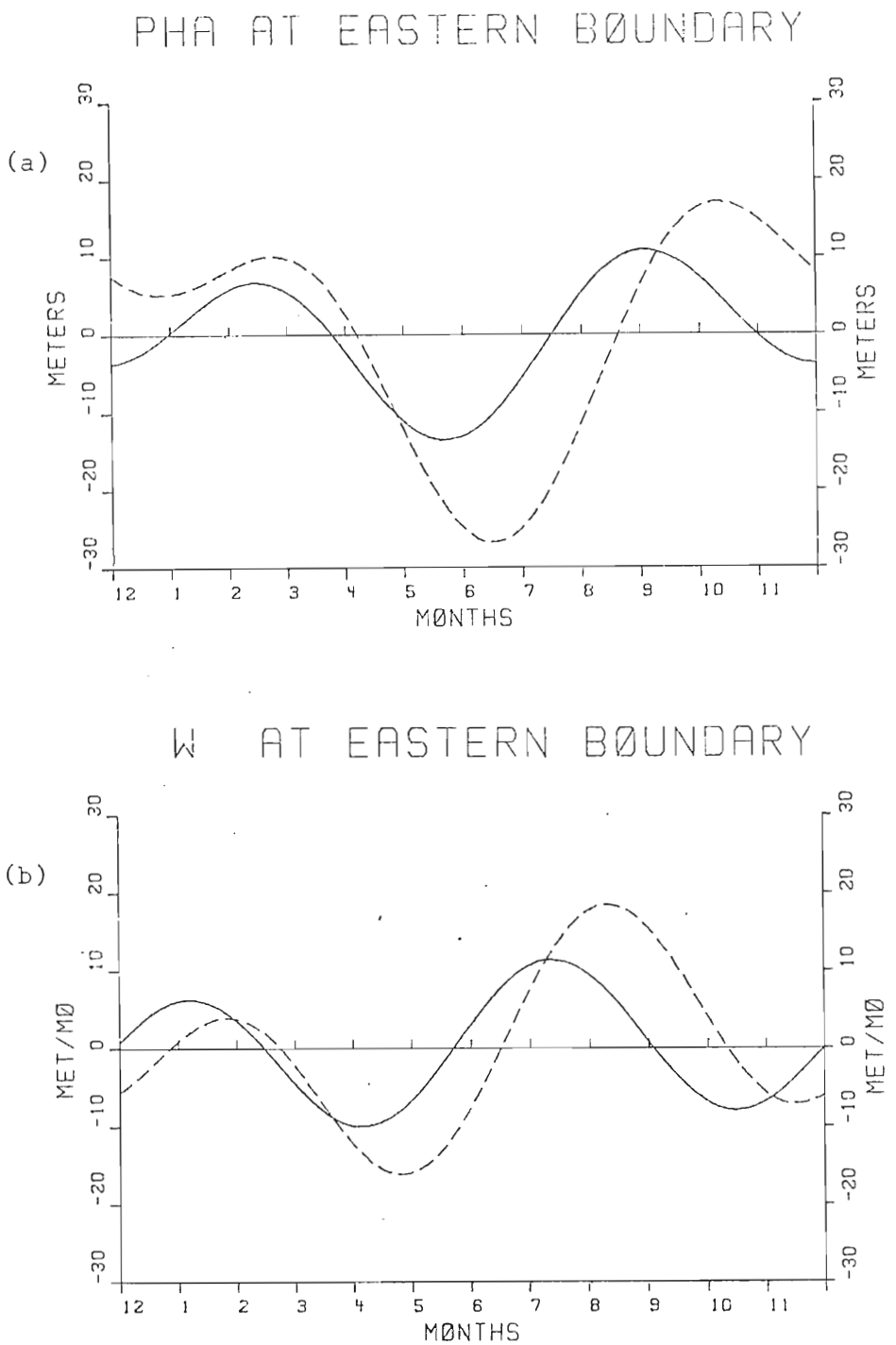

Fig. 24. Comparison of Year 4 of the linear numerical model solution (solid lines) for (a) PHA and (b) W with observations (dashed lines) given by Fig. 22(a) and Fig. 22(b), respectively. Inertial oscillations have been filtered from the numerical solution.

Fig. 24. Comparison of Year 4 of the linear numerical model solution (solid lines) for (a) PHA and (b) W with observations (dashed lines) given by Fig. 22(a) and Fig. 22(b), respectively. Inertial oscillations have been filtered from the numerical solution.

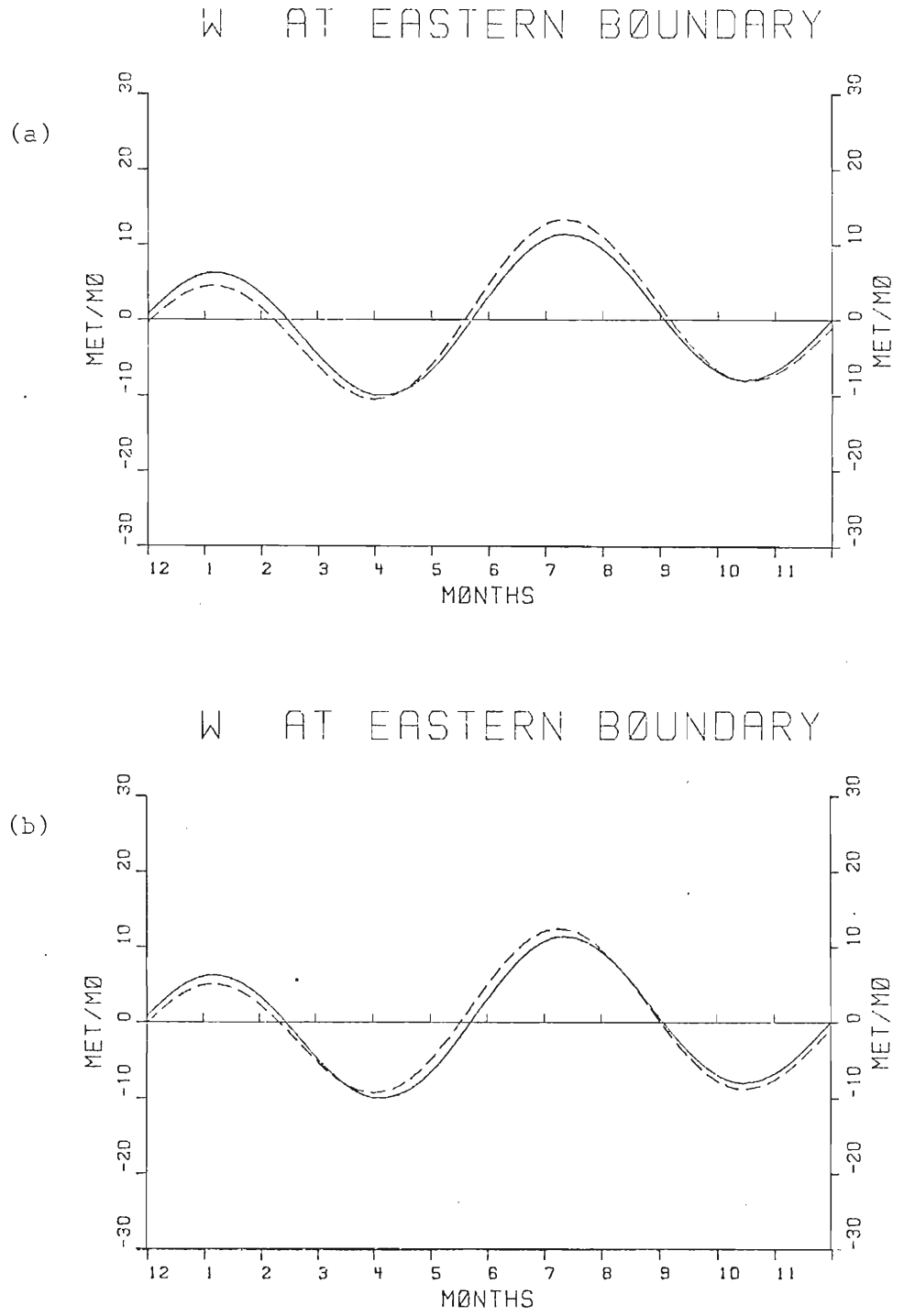

Fig. 25. (a) Comparison of linear numerical model solution (solid line) of W at eastern boundary at the equator with the sum of all the components of the full analytical expression. (b) Comparison of linear numerical model solution (solid line) with the sum of all analytic components evaluated assuming no reflection from the western boundary.

close; we can now apply the analytical model in an attempt to delineate the effects of individual waves.

The analysis in Section 4a showed that Kelvin waves dominated the response to the east of a wind stress patch. Hence the analytical expression was evaluated for the case in which only Kelvin waves and their reflections from the eastern boundary are included. This is equivalent to setting the reflection coefficient of the western boundary, R_W, equal to zero. Fig. 25b shows the comparison between the sum of all the Kelvin wave responses and the linear numerical solution. Again, the comparison is very close. This tells us that although the numerical model includes all the waves and their multiple reflections from the boundaries, the vertical motion of the model pycnocline is due to the propagation of Kelvin waves excited in the interior region. The results do not depend upon the position nor the nature of the western boundary.

Finally, we will examine whether the interfacial displacement at the eastern boundary can be attributed to the effects of Kelvin waves emanating from the region where the semi-annual component of the wind stress is a maximum. Fig. 21 shows that this region is between 180° and 120°W. In Fig. 26 the results of including only the semi-annual Kelvin waves which originate from the above area are shown. Clearly, the semi-annual response of the model pycnocline is governed by the remote forcing due to Kelvin waves excited between 180° and 120°W.

Although equatorial Kelvin waves have yet to be observed in the ocean, recent theoretical studies indicate that once these waves are initiated, they should be able to traverse large distances without sub-
ocean, recent theoretical studies indicate that once these waves are initiated, they should be able to traverse large distances without sub-
stantial modification by the mean circulation (McPhaden and Knox, 1979;

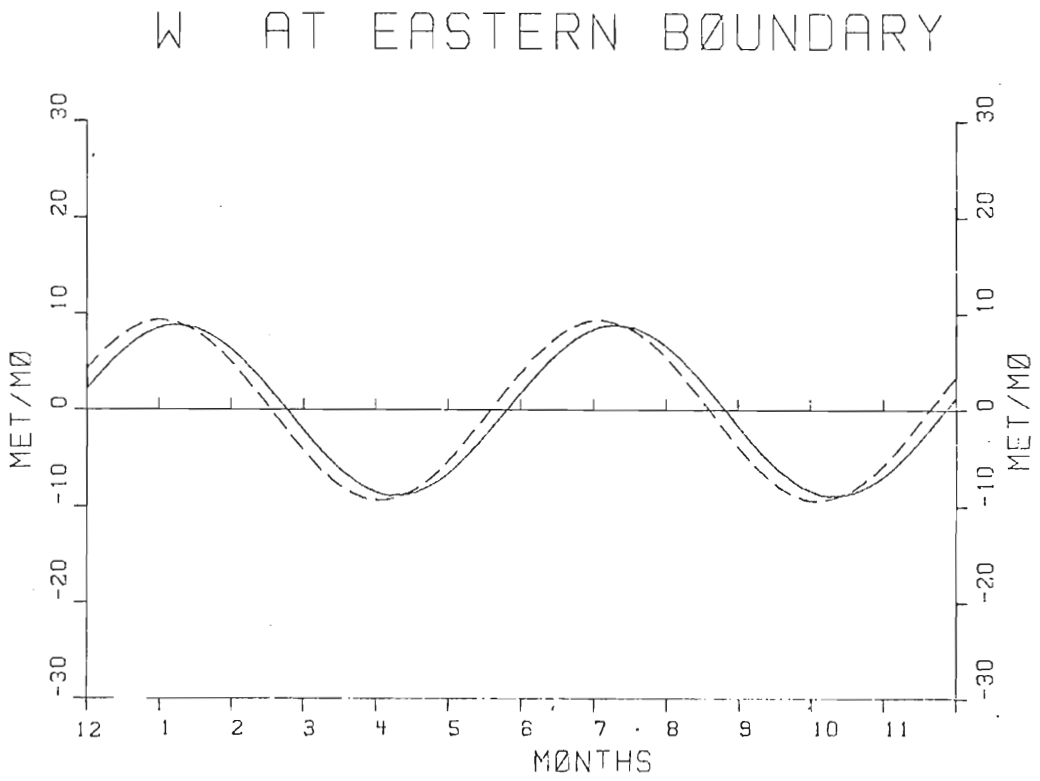

Fig. 26. Comparison at the eastern boundary of the equator of the semi-annual component of W determined by the linear numerical model (solid line) with the same component of the analytical expression evaluated using only Kelvin waves excited between 180° and 120°W.

Philander, 1979b; and Semtner, personal communication). The results presented above are strong indirect support for their existence, and can be tested by the acquisition of appropriate long period data records in the eastern equatorial Pacific.

d. Seasonal Circulation

In this section, the numerical model simulation described in Section 4b is used to examine the seasonal variability of the circulation along the equator. The numerical results are applicable only within approximately $\pm$ 5° of the equator, because we have assumed that the forcing has a uniform meridional distribution.

In Fig. 27a, the seasonal variation of the upper layer thickness (ULT) along the entire equator is shown. The variability at the eastern boundary has been discussed above. The model data are also consistent with the observations of Taft and Jones (1974) who were unable to find a mean zonal pressure gradient east of 115.5°W during the Piquero Expedition (June 26-August 4, 1969). The numerical simulation predicts that the lack of a zonal thermocline slope east of 115°W is a seasonal phenomenon.

The ability of the model to simulate the seasonal variability of the thermocline depth is much better east of approximately 130°W than to the west of this region. Although the amplitude of the model thermocline variation is consistent with observations in the central and western Pacific, there is only marginal agreement between the phase of the observed seasonal variability and the numerical simulation. This is not
Pacific, there is only marginal agreement between the phase of the observed seasonal variability and the numerical simulation. This is not
surprising in view of both the simplicity of the model and the much smaller amplitude of the seasonal cycle in the central and western Pacific.

(a)

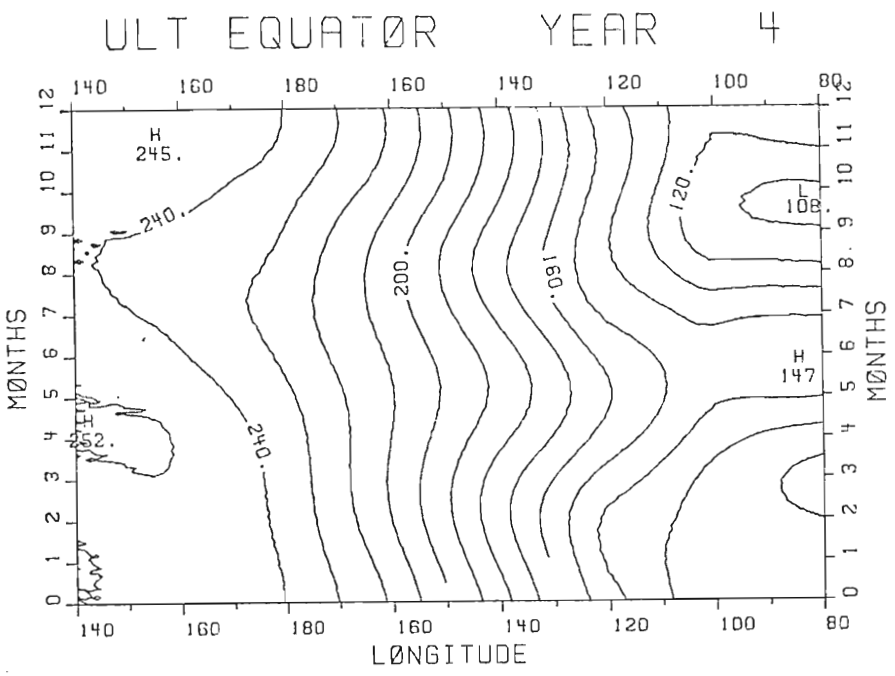

(b)

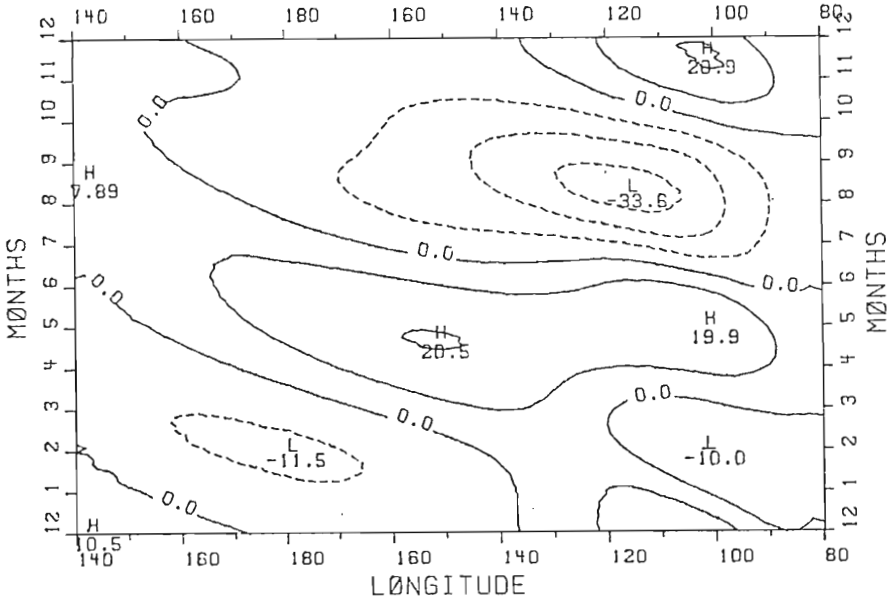

Fig. 27. Seasonal variation along the equator of (a) pycnocline depth and (b) zonal velocity component as predicted by nonlinear numerical model. Components of wind stress for the calculations are from Meyers (1979b) as shown in Fig. 21(b). The contour interval for (a) is

depth and (b) zonal velocity component as predicted by nonlinear numerical model. Components of wind stress for the calculations are from Meyers (1979b) as shown in Fig. 21(b). The contour interval for (a) is 10 m and for (b) is 10 cm sec^{-1}.

The mean zonal slope of the thermocline, however, is accurately represented by the numerical model along the entire equatorial Pacific (Figs. 20, 27a). The ability of the numerical model to simulate a realistic zonal slope of the equatorial thermocline will prove to be an important facet of the El Niño experiments in the following section.

The predicted seasonal variation of the zonal velocity component along the equator is shown in Fig. 27b. This figure depicts only the departure from the mean flow, because the layered model does not possess a realistic steady state solution for the current field. If the model is forced only by the mean winds, the steady state solution is a zero flow condition in which the mean wind stress balances the pressure gradient. The mean surface current at the equator is part of the westward South Equatorial Current.

The amplitude of the variability of the surface flow shows a distribution patterns similar to the pycnocline variability (Fig. 27a), that is, the largest amplitude fluctuations are in the eastern third of the equator. The model predicts that the mean westward flow at the equator is weakened from April to June, and strengthened from July to October. This is consistent with the analysis of the EASTROPAC observation by Tsuchiya (1974). The observations taken during this year-long expedition in the eastern Pacific reveal that the westward surface current very near the equator was most intense in the fall season but weakest in the spring. In fact, Tsuchiya observed a very weak eastward surface flow near the equator during the April to May period. Although this eastward equatorial surface current is often viewed as the surfacing of flow near the equator during the April to May period. Although this eastward equatorial surface current is often viewed as the surfacing of the Undercurrent, Tsuchiya found that such a hypothesis was not consis-

tent with his analysis. Moore and Philander (1977) support Tsuchiya's contention by presenting a theory which relates the dynamics of the Undercurrent to that of the surface flow. This theory predicts that variations of the intensities of these two currents are negatively correlated. Such a theory is consistent with the observations of Taft and Jones (1974) who found that the strongest flow of the Undercurrent is in the spring, while the weakest flow occurs in the fall.

The numerical simulation predicts a large semi-annual component of the surface flow in the eastern equatorial region. This component is associated with the remote forcing mechanism described earlier. Hence, in November and December, there may be another period of weak (strong) surface equatorial (Undercurrent) flow in the eastern equatorial Pacific. Since the numerical model overestimates the downwelling event at the end of the year, the associated variations in the velocity field may not be as large as in the spring event. Long period current meter records will be required to test this hypothesis.

Vector plots for the velocity field in the eastern tropical Pacific are shown in Fig. 28. These plots reveal that the equatorial flow periodically separates into two branches. This feature was also observed by Hurlburt, et al. (1976) in their numerical simulation of El Niño. They explained it as an effect due to the westward propagation of the pressure field as an internal Rossby wave.

The seasonal variation along the eastern boundary of the meridional velocity field and the ULT are shown in Fig. 29. In this simulation, the seasonal variation of the zonal winds along the equator does not pro-

velocity field and the ULT are shown in Fig. 29. In this simulation, the seasonal variation of the zonal winds along the equator does not pro-

duce a large meridional velocity component along the eastern boundary

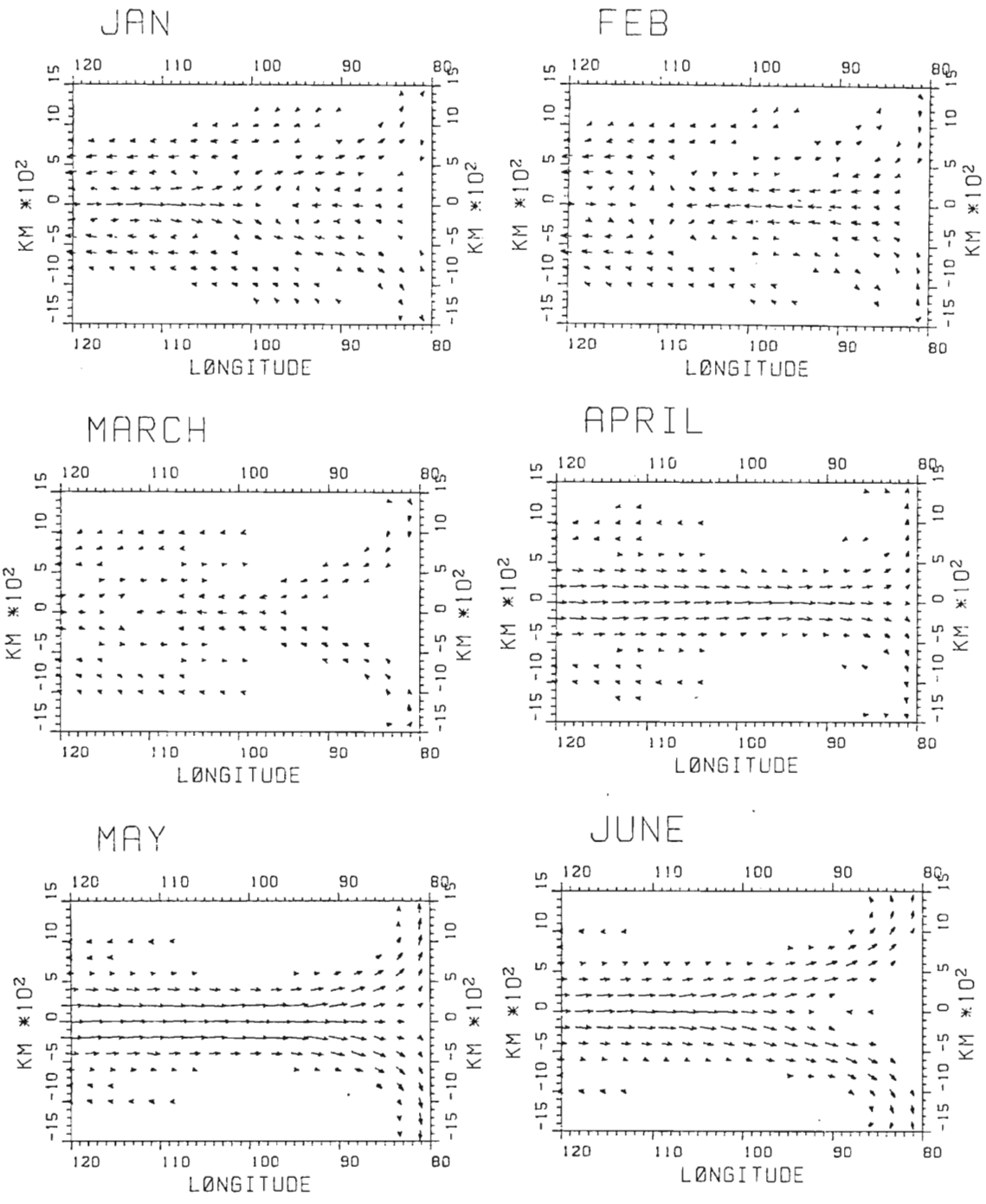

Fig. 28a. Velocity vectors depicting the circulation in the eastern tropical Pacific for the first six months of the seasonal cycle. The

Fig. 28a. Velocity vectors depicting the circulation in the eastern tropical Pacific for the first six months of the seasonal cycle. The numerical simulation is that which is represented in Fig. 27.

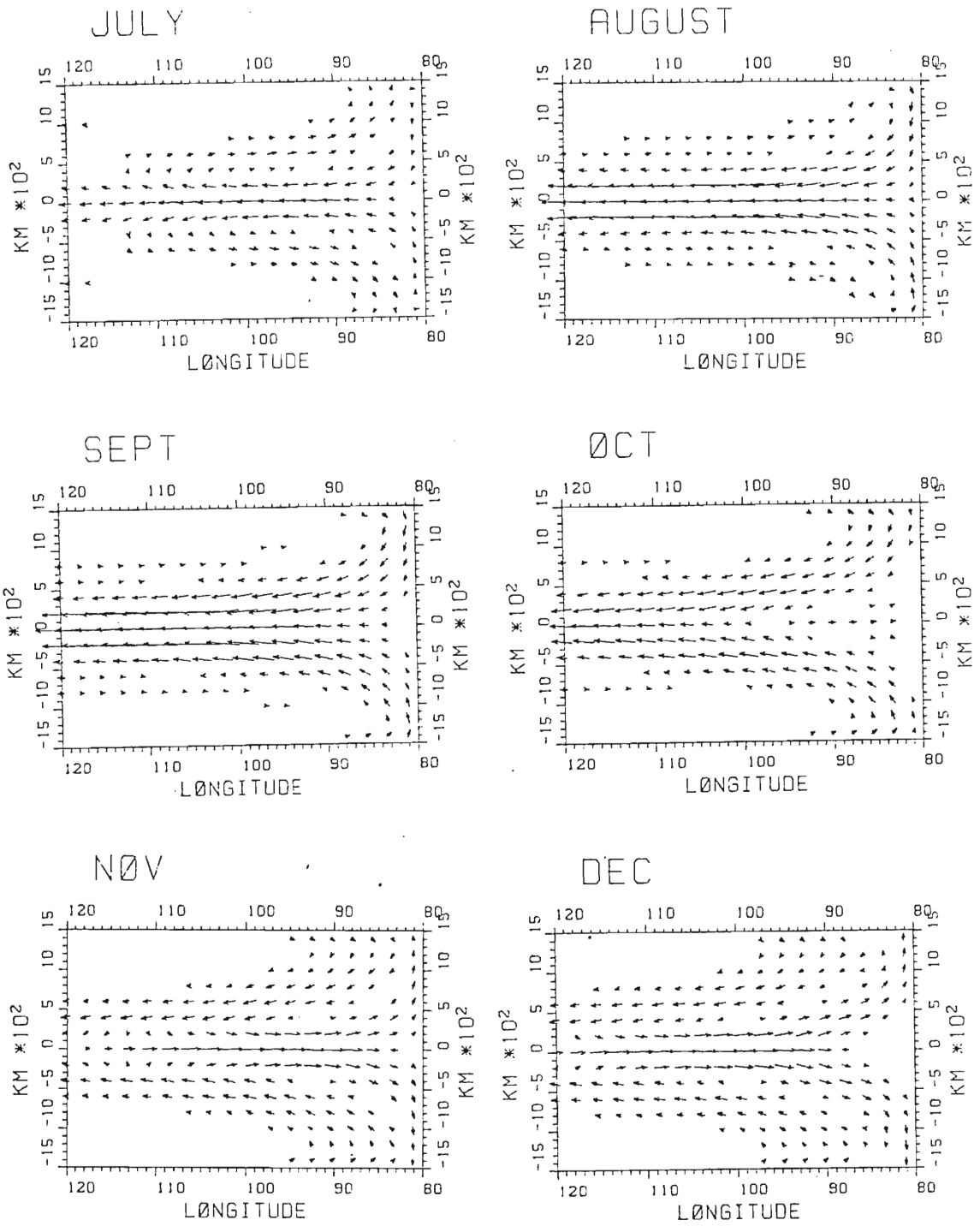

Fig. 28b. Same as Fig. 28(a) except for second half of year. The numerical solution is shown at the mid-point of each month.

Fig. 28b. Same as Fig. 28(a) except for second half of year. The numerical solution is shown at the mid-point of each month.

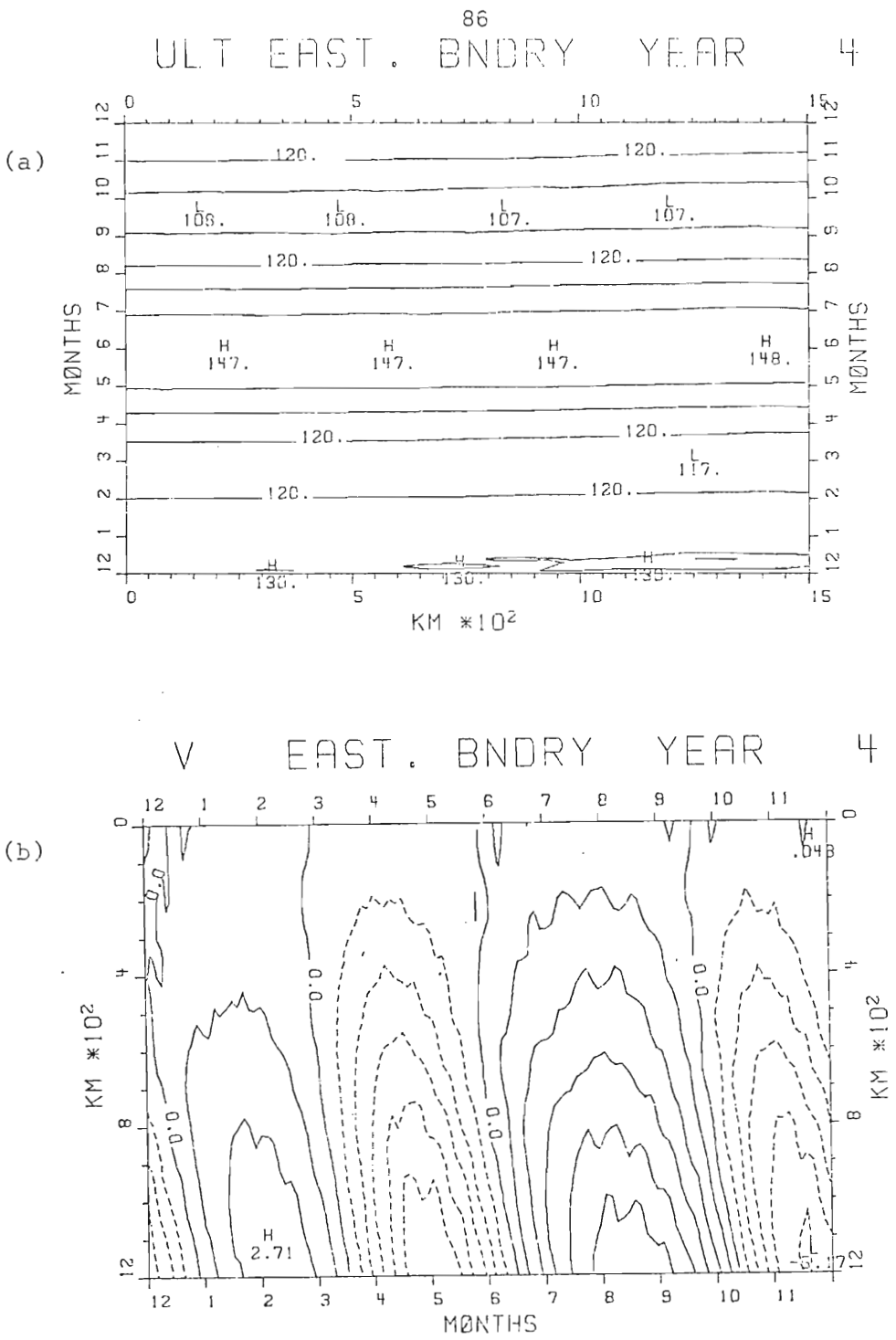

Fig. 29. The y-t sections along the eastern boundary for (a) upper layer thickness and (b) meridional velocity component determined by the nonlinear numerical simulation of the seasonal cycle. The contour interval is 10 m for (a) and 1 cm sec^{-1} for (b). The dashed lines in (b) indicate poleward flow.

Fig. 29. The y-t sections along the eastern boundary for (a) upper layer thickness and (b) meridional velocity component determined by the nonlinear numerical simulation of the seasonal cycle. The contour interval is 10 m for (a) and 1 cm sec^{-1} for (b). The dashed lines in (b) indicate poleward flow.

(Fig. 29b). These plots are included primarily for comparison purposes for the El Niño experiments in the following section.

6. MODELLING OF EL NIÑO

El Niño is an anomalous oceanographic and meteorological event which is characterized by the sudden appearance of abnormally warm surface water on the scale of a thousand kilometers off the coasts of Ecuador and Peru. These warm water anomalies, which can persist for up to a year or more, also extend thousands of kilometers along the equator. There are no criteria which clearly define El Niño, because 1) the onset of the event occurs during the normal seasonal warming period and 2) the magnitudes of El Niño-like events vary from slightly greater than the seasonal perturbations to extreme fluctuations. Hence, most studies of this phenomenon focus on major El Nino events. The most recent occurrences of major El Niños were in 1957-58, 1965, 1972-73 and 1976. These primary El Niño events are not only catastrophic to the Peruvian fishing industry, but also appear to be closely related to global scale changes in the circulations of the atmosphere and the ocean (Bjerknes, 1966b, 1969, 1972; Julian and Chervin, 1978; Namias. 1976; Quinn and Burt, 1970; Barnett, 1978; Weare, et al., 1976; Wyrtki, 1973).

To what extent El Nino is the cause of or the result of large scale atmospheric anomalies is not well understood. Most studies of the oceanic manifestation of El Nino ignore complex air-sea feedback mechanisms and concentrate, instead, on the following question: Given a prescription of atmospheric forcing prior to and during El Niño, can one

isms and concentrate, instead, on the following question: Given a prescription of atmospheric forcing prior to and during El Niño, can one

account for the oceanic observations of this event? Recent theoretical studies have been able to account only for the onset phase of the event, i.e., the first few months (Hurlburt, et al., 1976; McCreary, 1976, 1977). In this section, the nonlinear numerical model is used to simulate El Niño from the onset phase to the termination of the event. In spite of the simplicity of the model, the numerical simulation is able to account for many of the observed features associated with El Niño. The dynamics of the model event are also discussed.

a. Observational and Theoretical Background

There are a number of excellent descriptions of the observational evidence associated with El Niño (e.g., Bjerknes, 1961, 1966, Wyrtki, 1975a, 1977, 1979; Caviedes, 1975; Wooster and Guillen, 1974; Namias, 1976; Barnett, 1977 and Zuta, et al., 1974). It is not within the scope of this section to detail these works; instead, we will focus on the most salient features which appear to be common to all or most major El Niño events. The most prominent indicator of El Niño in the eastern Pacific is the sea surface temperature (SST) anomaly pattern. Both Wooster and Guillen (1974) and Zuta, et al., (1974) chronicle El Niño in terms of three phases of SST changes. The first phase is characterized by a very sudden appearance of warm water along the coasts of Equador and Peru. The warm water, which is of equatorial origin, advances rapidly along the coast. Although the onset of El Niño is coincident with the normal seasonal warming, the magnitude and extent of the warm equatorial water go well beyond the usual seasonal limits. The initial phase lasts for several months; its termination is characterized by the retreat of the warm water towards the equator. The intermediate

phase is a quiescent period lasting for approximately six months. During this phase, warm SST anomalies persist but gradually diminish in magnitude. The final phase is similar to the initial period. Very warm SST anomalies suddenly reappear along the South American Coast. The magnitude of SST anomalies during this phase are usually not as large as during the initial period. The final phase generally begins about one year after the initial onset of El Niño. The duration of the third phase is shorter than the initial period; frequently, the final stage terminates abruptly.

The occasional appearance of warm SST anomalies in consecutive years is one of the major mysteries of El Niño. Unlike the events in 1957-58 and 1972-73, the occurrences of El Niño in 1965 and 1976 evidenced only single peaks in temperature (Wyrtki, 1979). In fact, the SST in the eastern Pacific and along the South American coast were substantially colder than normal seasonal values during the first quarter of 1966.

Wyrtki (1977, 1979) describes El Niño in terms of the sea level response, which he also shows is representative of the vertical motion of the thermocline along the equator. Wyrtki finds that sea level rapidly peaks at the start of El Niño along the coast of Peru. The western Pacific, however, evidences a very different response of sea level during the event. In this region, a very slow decline of sea level occurs throughout the entire El Niño year. This sequence of events occurred in both the 1972 and 1976 El Niño years. However, substantial differences were encountered between those two events during the year which followed both the 1972 and 1976 El Niño years. However, substantial differences were encountered between those two events during the year which followed each of these occurrences. In 1973 a second peak in sea level was

observed which was similar in nature to the peak in the preceding year. No successive sea level peak was observed in 1977. In both 1973 and 1977, the return to a normal sea level distribution occurred very rapidly.

Bjerknes (1966a) was the first to suggest that the occurrence of El Niño is related to changes in the Pacific trade wind system. It was Wyrtki (1975b), however, who proposed the specific theory that El Niño is caused by the sudden relaxation of the equatorial trade winds in the central and western Pacific Ocean. Analysis of the equatorial winds by Wyrtki and Meyers (1975) revealed that 1) major El Niño events are often preceded by a stronger than normal wind which lasts for a year or more, 2) subsequent to relaxation, the winds in the central and western Pacific remain weak for approximately a year, and 3) the winds in the eastern equatorial Pacific and along the coast of Peru are close to seasonal values during El Niño events. Hence, Wyrtki (1975a) hypothesized that the relaxation of the wind in the central and western equatorial Pacific would allow warm water, which had accumulated in that part of the ocean prior to El Niño, to flow eastward. The eastward flow, would be accomplished either by an internal Kelvin wave or by an increase in the transport of the North Equatorial Countercurrent. Eventually, the warm water would accumulate in the eastern Pacific and subsequently affect the coastal regions off Ecuador and Peru.

Wyrtki's hypothesis received theoretical support from Hurlburt, et al. (1976) and McCreary (1976, 1977). Both these modelling efforts showed that a Kelvin wave, excited by the relaxation of the wind stress,
et al. (1976) and McCreary (1976, 1977). Both these modelling efforts showed that a Kelvin wave, excited by the relaxation of the wind stress,
could account for the rapid, pronounced warming during the onset phase

of El Niño. The numerical solutions of Hurlburt, et al., reveal that nonlinear effects may help to explain the extremely rapid response observed during El Niño. The linear, analytic model of McCreary shows that a realistic distribution of the wind stress about the equator does not only produce the necessary Kelvin wave, but also can account for possible cross equatorial flow at the eastern boundary during El Niño.

Wyrtki's hypothesis, as well as the above modelling efforts, pertain only to the onset of El Niño. Generally, it is believed that more complicated models are required in order to account for the longer time scale aspects of El Niño, such as the slow decline in sea level at the western boundary, the reoccurrence of temperature peaks in successive years and the rapid end to the El Niño event. This hypothesis is tested in the next section. The very simple numerical model described in Section 2 is utilized to examine a model El Niño event from its inception to its termination.

b. Numerical Results

In Section 5, it was shown that the numerical model results could account for a number of observed features of the seasonal cycle in the equatorial Pacific. Among other aspects, the model realistically represents the zonal slope of the main thermocline and the seasonal variation of its depth at the eastern boundary. The ability of the model to represent these features makes it a very attractive tool with which to examine fundamental dynamics related to El Niño. The strategy of the El Niño experiments in this chapter is to initialize the model with the seasonal solution at the end of year 2, and, subsequently, examine the anomalous model solutions resulting from the application of El Niño-type winds.

There are several detailed accounts of the variability of the zonal equatorial winds related to El Niño (e.g., Wyrtki, 1975; Wyrtki and Meyers, 1976; Hickey, 1975). In an attempt to compromise between the complexity of directly applying real wind data and the over-simplicity of using highly idealized winds, we have made the following assumptions about the zonal equatorial winds associated with El Niño. 1) The zonal equatorial wind stress at inter-annual time scales has a much smaller amplitude in the eastern Pacific than in the western regions. 2) Even during El Niño periods, the seasonal cycle continues unchanged throughout the tropical Pacific. 3) The zonal distribution of the wind stress amplitude at inter-annual time scales is similar to the distribution of the mean zonal wind stress. 4) During El Niño events, the magnitude of the wind relaxation is comparable to the value of the mean wind stress in that region. There may be no single El Niño event in which all these assumptions apply. However, it is felt that these assumptions embody the fundamental behavior of the forcing during a major El Niño event. In addition, only the symmetrical response about the equator is examined. Although asymmetrical affects may be important to El Niño dynamics, it is the response associated with the Kelvin waves which is dominant, i.e., the symmetrical solution.

The initial state for the standard El Niño case is the seasonal solution at the end of year two. Subsequent numerical integration over three years represent the intensification of the winds prior to El Niño, the El Niño year and the return to normal conditions, respectively. Only the mean component of the winds west of 140°W is modified during the numer-

the El Niño year and the return to normal conditions, respectively. Only the mean component of the winds west of 140°W is modified during the numer-

ical integrations. The seasonal components of the trade winds are main-

tained at their long-term values as well as the mean winds west of 140°W. During the third year of integration, the mean wind components west of 140°W are increased linearly over a twelve month period, at which time they are a factor of 1.5 greater than their long-term values. The sudden relaxation of the equatorial winds occurs at the start of year four. The mean winds west of 140°W are decreased over a two month period to one half their normal mean values and are maintained at these values throughout the remainder of the year. At the beginning of year five, the relaxed winds are increased to their long-term magnitudes over a two month period. After the first two months of the last year, the forcing is identical to the wind stress used in the seasonal simulation, and no further modifications are made.

The details of the standard run are described below. Four additional numerical simulations are performed; the differences between these cases and the standard run are shown in Table 3.

The intensification of the mean winds west of 140°W causes a westward zonal acceleration relative to the seasonal response (Figs. 27b, 30a). The jet continues to accelerate rapidly until the arrival of an equatorially trapped Kelvin wave excited by the time variation of the wind stress divergence. The Kelvin wave, which propagates eastward, causes the zonal pressure gradient in the vicinity of the wind to increase, thereby helping to balance the increased wind stress force (Fig. 30b). In the region to the east of the increased forcing, the Kelvin wave produces upwelling relative to the seasonal solution (Fig. 31). As the wind continues to increase, so do the westward flow and Kelvin wave produces upwelling relative to the seasonal solution (Fig. 31). As the wind continues to increase, so do the westward flow and upwelling at the eastern boundary. At the end of year three, the model

Table 3. Description of Winds for El Niño Cases

Case	Description of Mean Winds West of 140°W During El Niño Experiments		
	Year 3	Year 4	Year 5
1	Winds increase over a 12 month period to 1.5 times their normal value (NV).	Relax over first 2 months to .5 their NV.	Strengthen over first 2 months to NV.
2	Same as Case 1	Relax over first month to .5 NV	Strengthen over 2 month period to NV beginning at month 3.5
3	Same as Case 1	1.5 NV for 1st 2 months. Subsequent relaxation is similar to case 2	Same as Case 1
4	No modification	Winds relax to zero value	No change
5	Same as Case 1	Same as Case 1	Same as Case 1

(a)

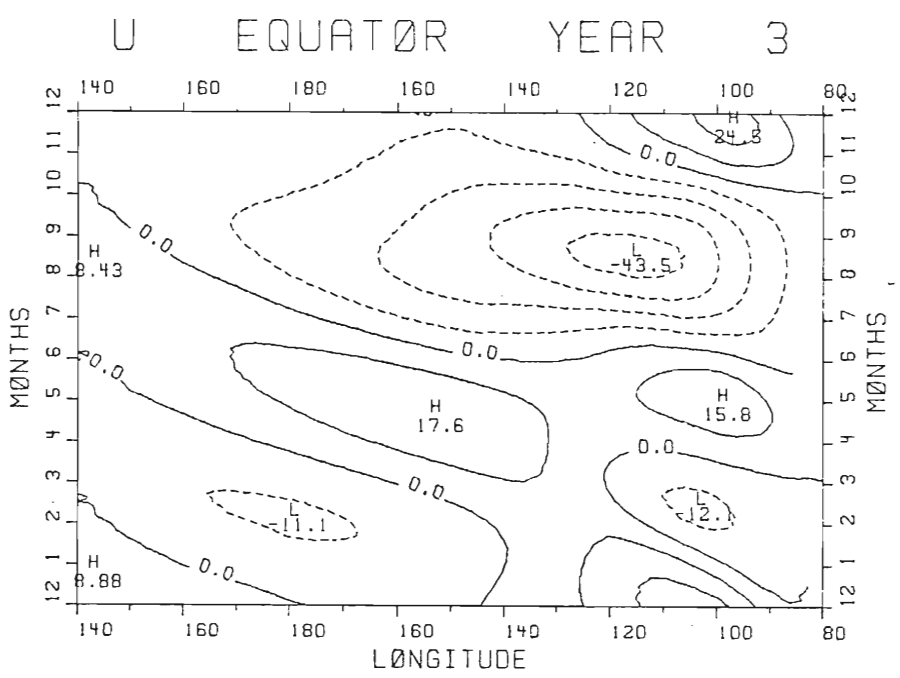

(b)

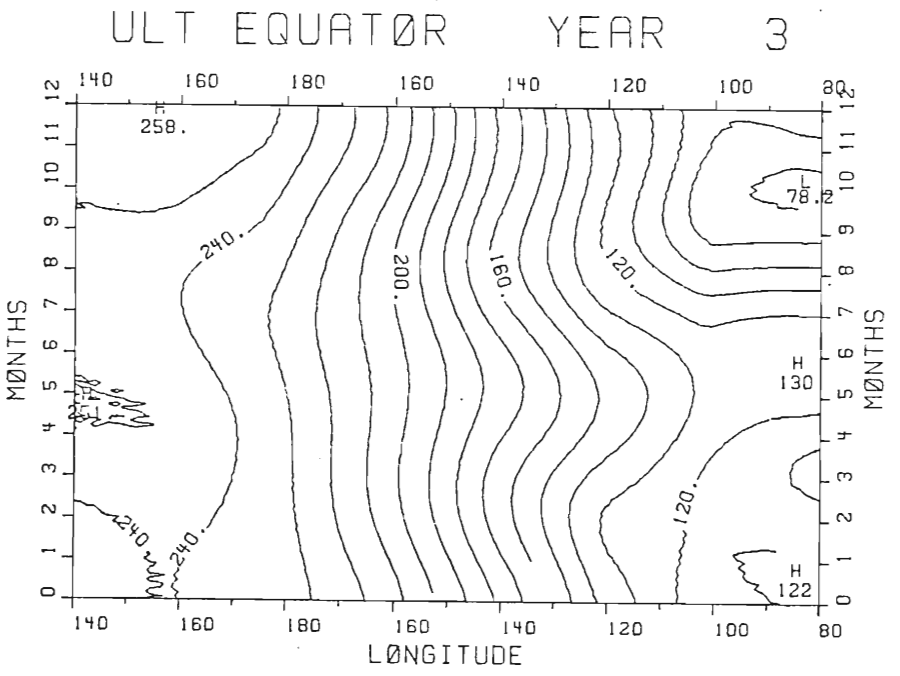

Fig. 30. The x-t sections along equator for (a) zonal velocity component and (b) the upper layer thickness during the intensification phase of Case 1. During this year the mean winds west of 140°W are linearly increased to 1.5 times their long-term value. The contour interval is 10 cm sec^{-1} for (a) and 10 m for (b).

component and (b) the upper layer thickness during the intensification phase of Case 1. During this year the mean winds west of 140°W are linearly increased to 1.5 times their long-term value. The contour interval is 10 cm sec^{-1} for (a) and 10 m for (b).

thermocline is nearly 40 m shallower than its normal seasonal value at the eastern boundary (Fig. 31). The east-west slope of the thermocline across the entire Pacific has intensified (Fig. 30b). These conditions are representative of the anomalously cold periods observed prior to El Niño events in the eastern equatorial Pacific and along the coast of South America.

The mean winds west of 140°W decrease to one-half their normal value at the start of year four. The maximum westward wind stress in the model central Pacific Ocean changes from approximately .75 dynes cm^{-2} to .25 dynes cm^{-2}. As stated above, the magnitude of the relaxation is dependent upon the value of the mean wind stress in a given longitudinal band. The response to this decrease in the wind in the central and western Pacific is what Wyrtki has hypothesized to be the initiating mechanism of El Niño. Detailed discussions of the dynamics associated with the onset of the event can be found in Hurlburt, et al. (1976) and McCreary (1976, 1977). Only the major features of the onset of El Niño are described below.

The relaxation of the wind stress west of 140°W destroys the approximate balance between the wind stress and the zonal pressure gradient. Subsequently, the unbalanced pressure gradient produces an eastward acceleration (Fig. 32). The divergence associated with the eastward driven flow excites equatorially trapped Rossby and Kelvin waves. In the vicinity of the decreased forcing, the equatorially trapped waves tend to bring the zonal pressure gradient into a new balance with the reduced wind stress. Hence, downwelling is initiated in the eastern portend to bring the zonal pressure gradient into a new balance with the reduced wind stress. Hence, downwelling is initiated in the eastern portion of the anomalously forced region, and upwelling in the western half.

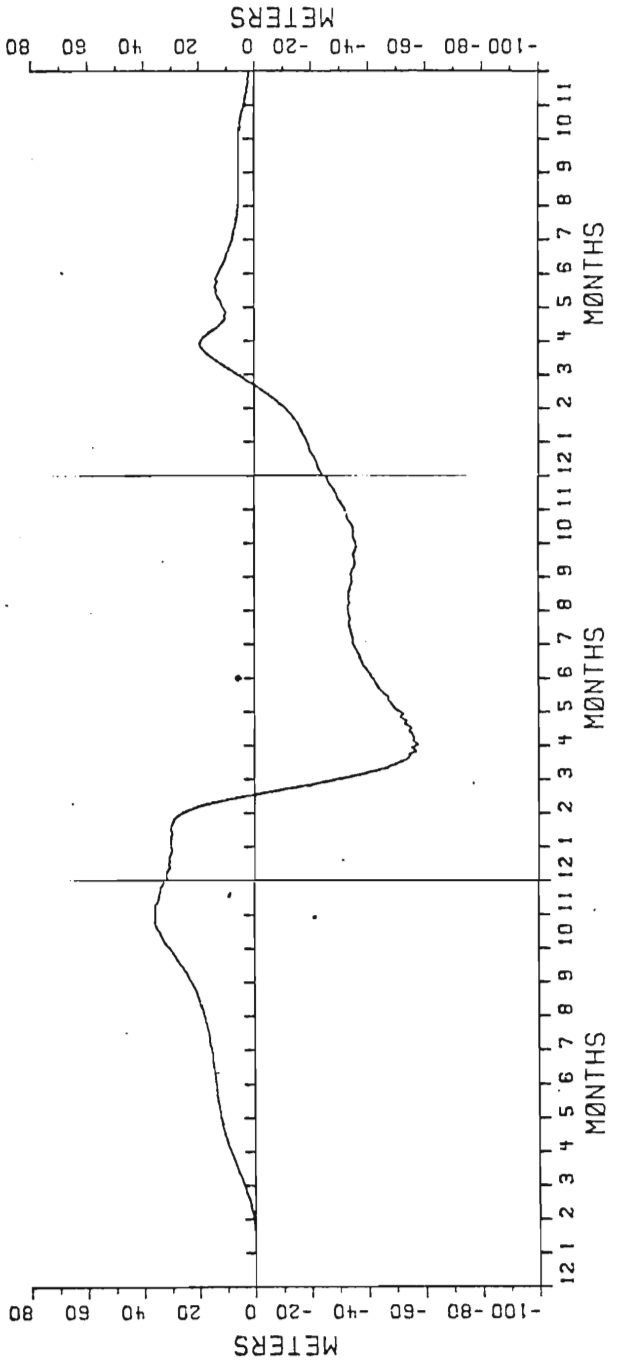

Fig. 31. Time series of the departure of the ULT from the long-term seasonal solution during yluring years 3, 4 and 5 of Case 1. The solution is evaluated at the eastern boundary of the equator.equator.

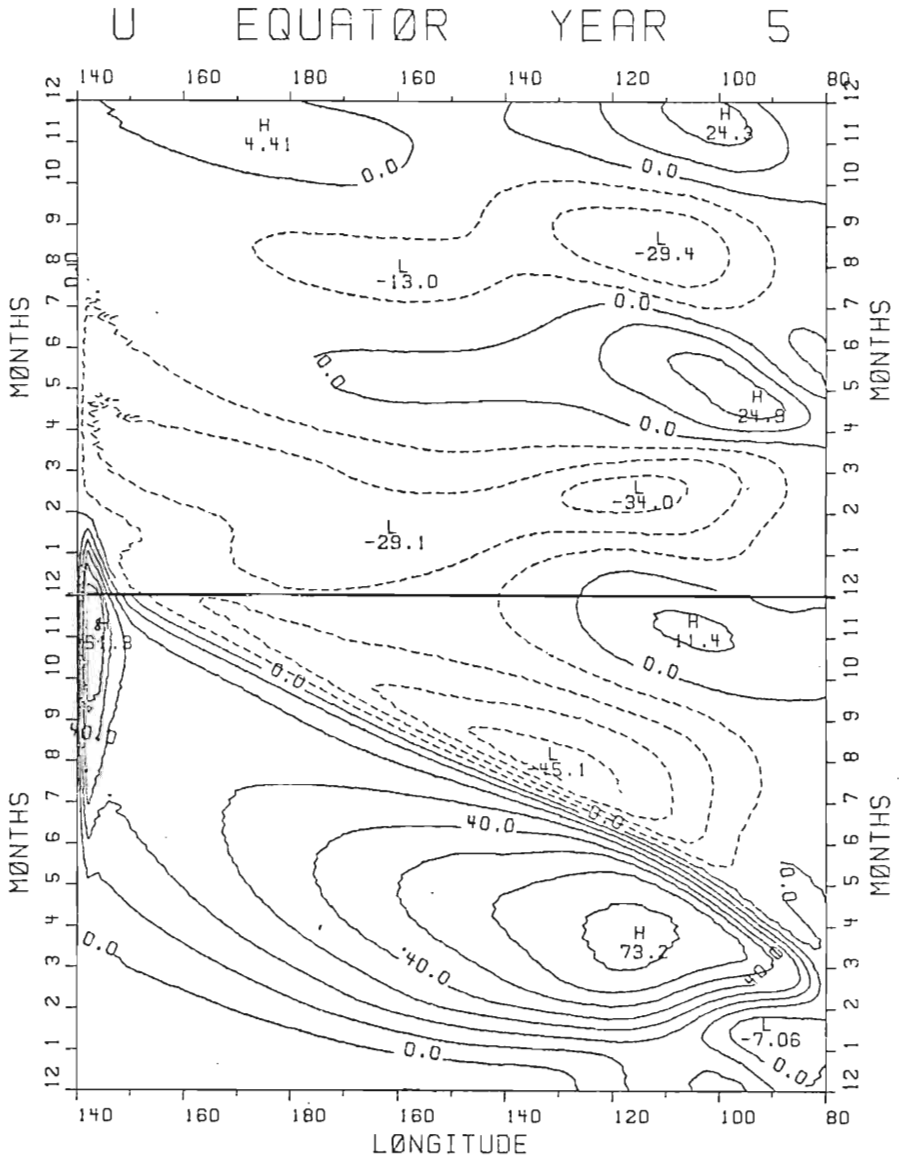

Fig. 32. The x-t section along equator for zonal velocity component during years 4 and 5 of Case 1. The rapid reversal of the flow in year 4 is due to the effects of a first mode internal Rossby wave which is excited by the incidence of the downwelling Kelvin wave at the eastern boundary. The contour interval is 10 cm sec^{-1}.

The leading edge of the Kelvin wave excited by the wind relaxation induces downwelling as it propagates eastward from 140°W. The downwelling is stopped only by the arrival of the trailing edge of the Kelvin wave[2].

Since there are no waves in the system which propagate faster than the Kelvin wave, the eastern boundary does not feel the effects of the reduced wind stress until the arrival of the leading edge of the Kelvin wave (Fig. 33). The combination of the incident Kelvin wave and the reflected Rossby waves create intense downwelling at the eastern boundary (Fig. 34). The pycnocline deepens by 100 m within two months and is finally stopped by the arrival of the trailing edge of the Kelvin wave (Fig. 33). The slight downwelling which continues between months 4 and 5 (Fig. 33) is a result of the seasonal signal.

The deepening of the model thermocline at the eastern boundary represents the intense warming event observed during El Niño. The downwelling response at the equator is propagated poleward by a coastally trapped Kelvin wave (Fig. 35). Hence, along the eastern boundary, a poleward flow is generated which, in the real ocean, is capable of advecting warm equatorial water along the coasts of Ecuador and Peru (Fig. 35). The alongshore current has a maximum speed of approximately 20 cm sec^{-1}, which is four times the value generated by the seasonal oscillations.

---

[2] A Kelvin and a Rossby wave are excited at each edge of an anomalous wind stress patch. The waves generated at the eastern edge of a patch are equal in magnitude but opposite in sign to the respective waves excited at the western edge. Hence, the effects of the waves generated at the common boundary between two adjacent patches tend to cancel if the magnitudes of the forcing are comparable. The largest magnitude waves are initiated in the region of largest zonal wind stress divergence. It is frequently more convenient to refer to the sum of all the Kelvin waves generated by an anomalous wind event as a single Kelvin wave which possesses a leading edge and a trailing edge.

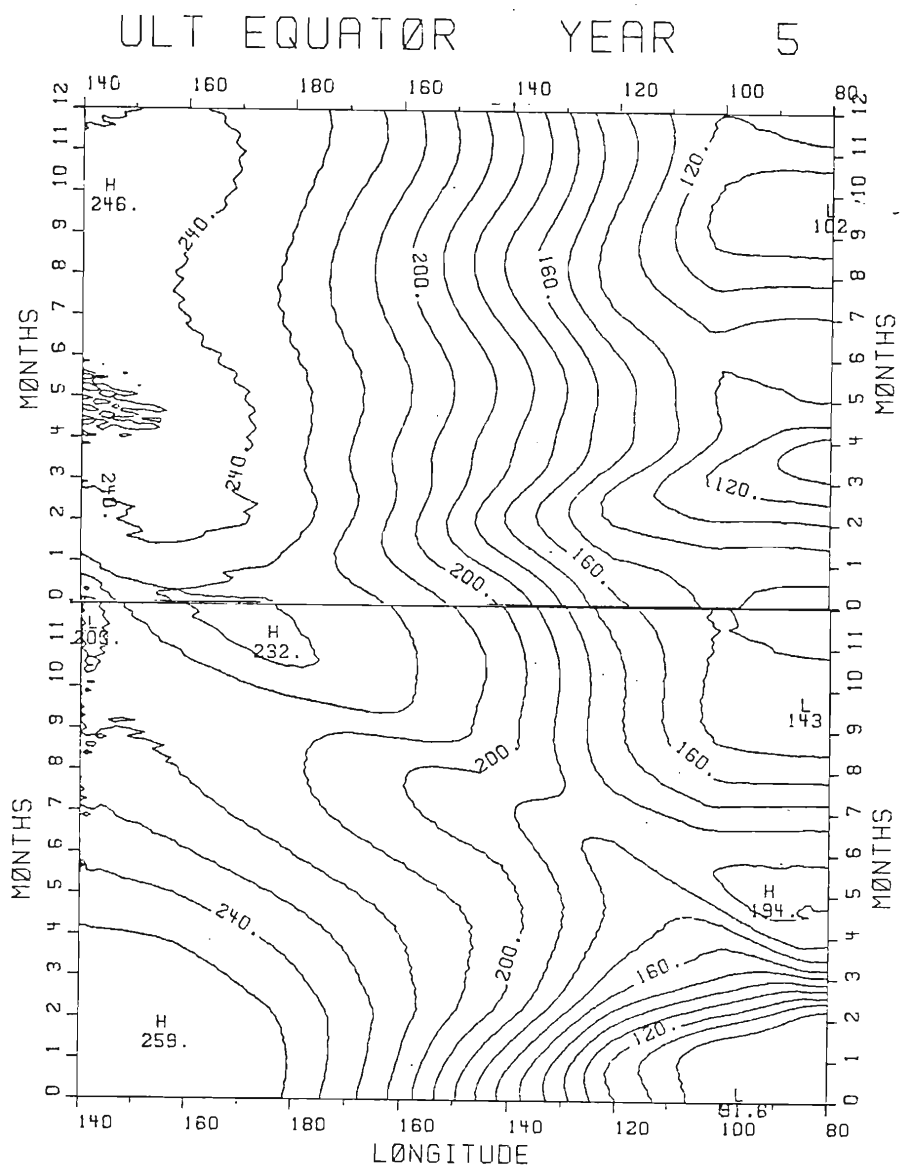

Fig. 33. The x-t section of upper layer thickness along equator during years 4 and 5 of Case 1. The internal Kelvin wave excited by the wind relaxation west of 140°W reaches the eastern boundary near month 2.

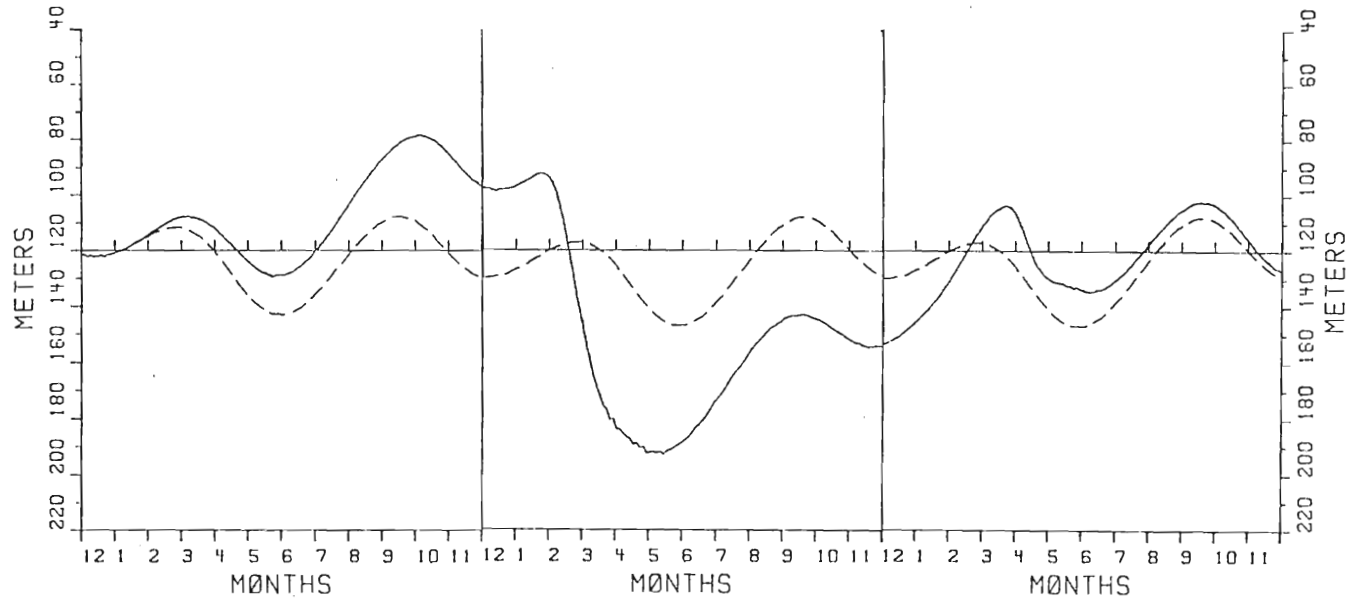

Fig Fig. 34. Time series of upper layer thickness at the eastern boundary during years 3, 4, and 5, and 5 of Case 1. The dashed line is the long-term seasonal value given by the numerical solutionolution (Fig. 23). The difference between the initial and final values in year 3 of the seasonaleasonal solution is caused by remnants of the initial spin-up transients.

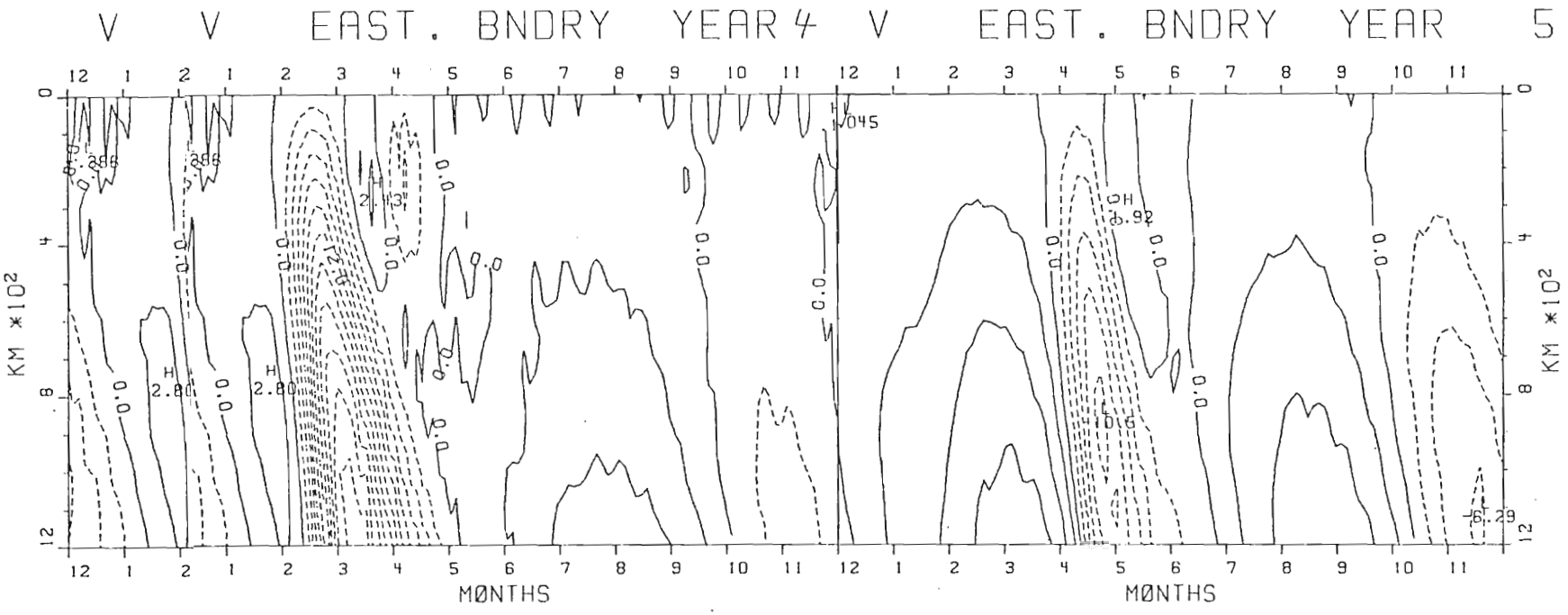

Fig. Fig. 35. The y-t section of meridional velocity component during years 4 and 5 of Case 1. The distae distance south of the equator is plotted along the ordinate. The contour interval is 2 cm sec^{-1}. Dc^{-1}. Dashed lines indicate poleward flow.

The incidence of the Kelvin wave onto the eastern boundary creates Rossby waves. The propagation of the Rossby waves away from the boundary broadens the region of poleward flow near the equator (Fig. 36 c-e); this feature is representative of the large offshore scale of the warming observed during El Niño.

Thus far, most of the described features have been aspects which were modelled by the earlier simulations (Hurlburt, et al., 1976; McCreary, 1976, 1977). Let us now examine the model event beyond the onset time scale in order to see if such a model can continue to account for observed features during El Niño.

The pycnocline reaches its maximum depth at the eastern boundary in early June and, subsequently, begins to return to its long-term position (Fig. 34). Throughout the rest of the year, the pycnocline appears to be strongly influenced by the seasonal cycle. However, Fig. 31 shows that even if we disregard the seasonal effect, the model pycnocline rises during the next four months. This is a result of the Rossby wave which was excited simultaneously with the Kelvin wave at the time of the wind relaxation. Since the Rossby wave propagates westward, the leading edge initiates upwelling, while the trailing edge halts the motion. After reflection from the western boundary, this upwelling response can propagate rapidly across the basin as a Kelvin wave. Although the effects of this wave are not nearly as dramatic as the downwelling Kelvin wave, this upwelling event causes the pycnocline to shallow by about 20 meters.

Between June and October of year 4, the pycnocline at the eastern meters.

Between June and October of year 4, the pycnocline at the eastern boundary rises by about 50 meters (Figs. 33, 34). The poleward flow

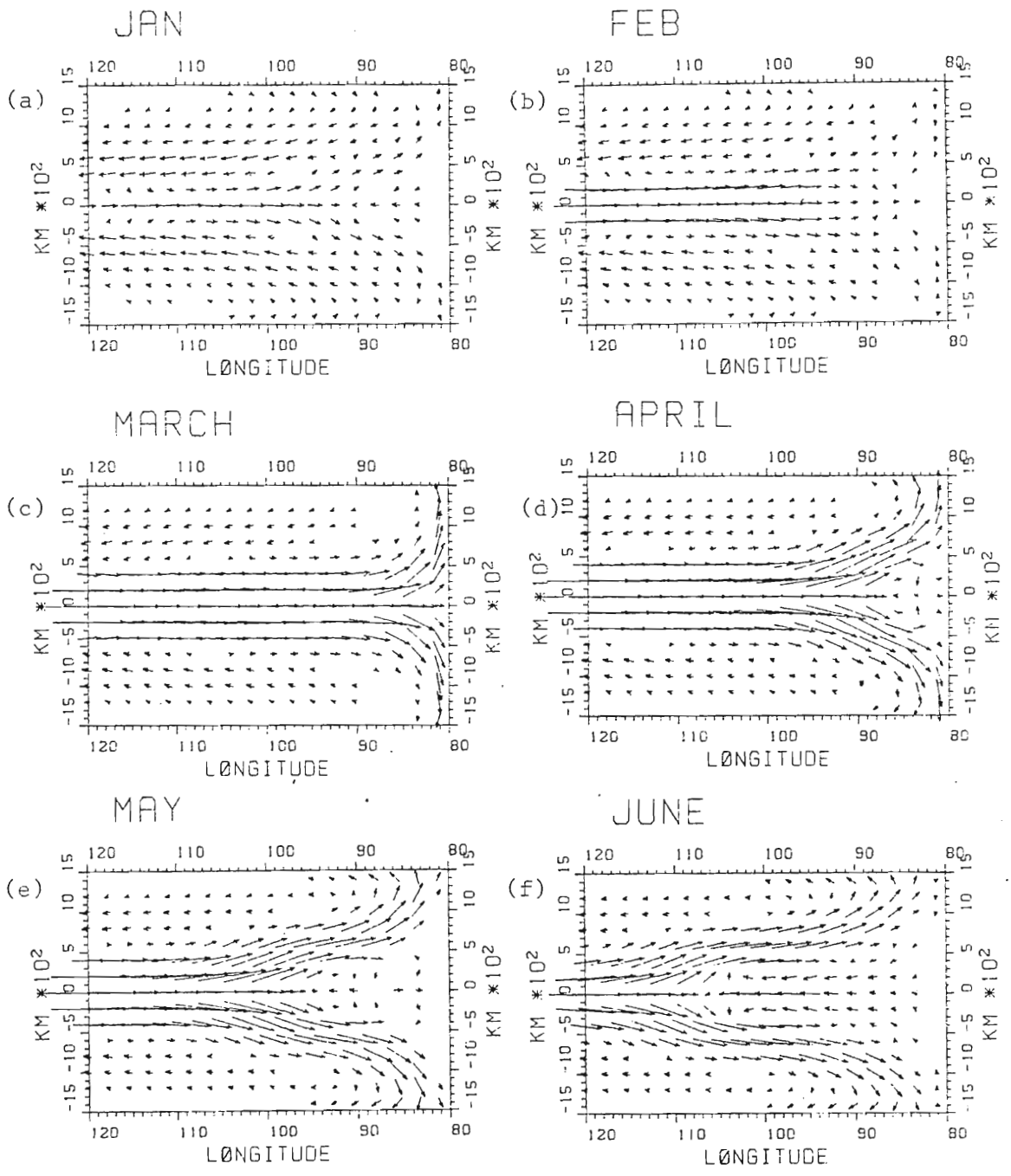

Fig. 36. Velocity vectors east of 120°W during year 4 of Case 1. The vectors, which are not situated on computational grid points, are evaluated at the mid-point of each month. The magnitude of the vectors

Fig. 36. Velocity vectors east of 120°W during year 4 of Case 1. The vectors, which are not situated on computational grid points, are evaluated at the mid-point of each month. The magnitude of the vectors can be determined using Fig. 32.

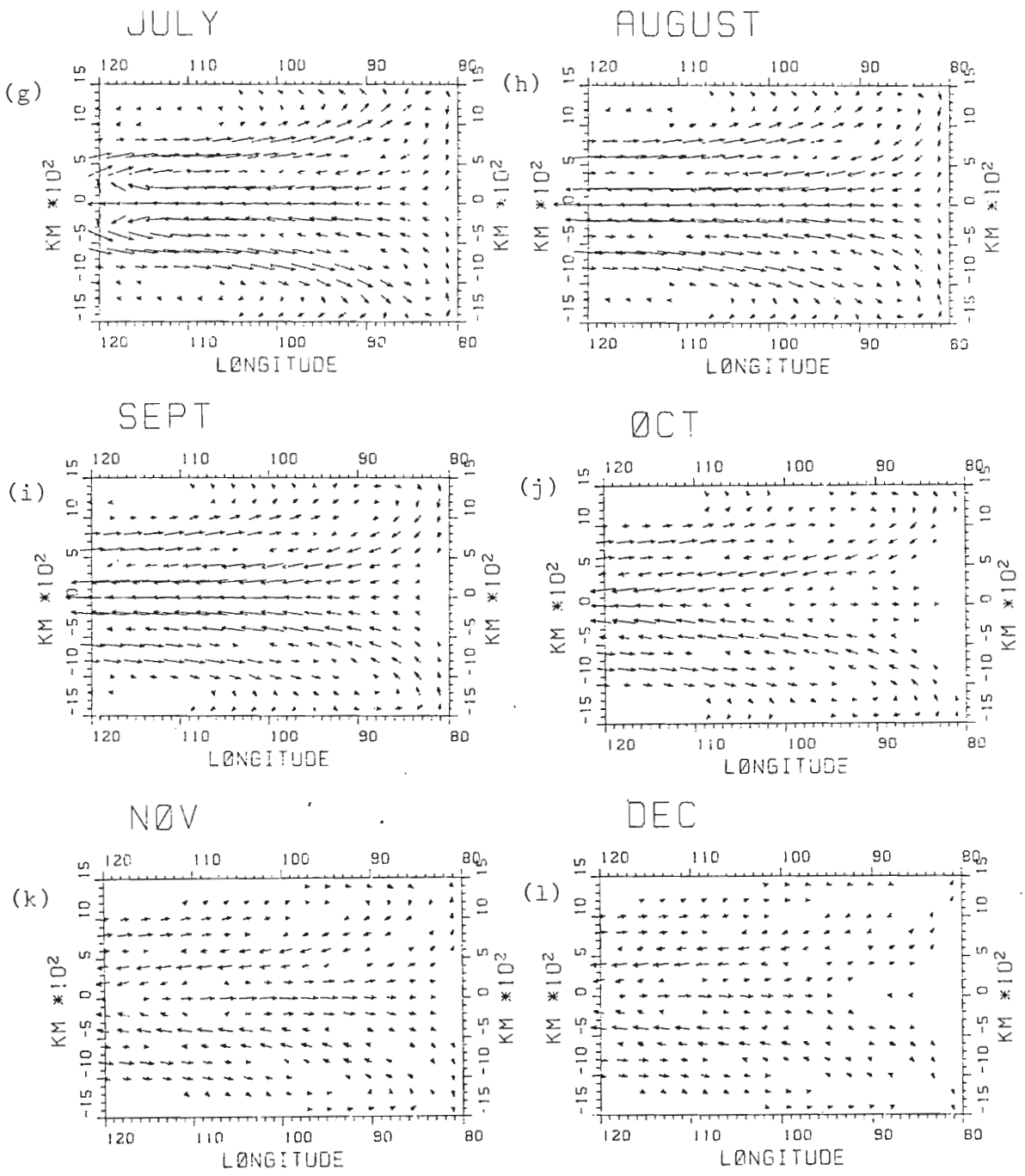
JULY
(g)
AUGUST
(h)
SEPT
(i)
ØCT
(j)
NØV
(k)
DEC
(l)
KM *10²
LØNGITUDE
120
110
100
90
80
15
10
5
0
-5
-10
-15

Fig. 36.

Fig. 36.

along the eastern boundary is replaced by weak equatorward flow (Fig. 35). Although the pycnocline remains well below its normal seasonal value, a certain semblance of the seasonal condition is reestablished. The numerical solution during the second half of year 4 is consistent with the quiescent period reported by Wooster and Guillen (1974) and Zuta, et al., (1974). During this period it was observed that, although warm water anomalies persisted, the normal seasonal cycle had a significant effect. If, however, the seasonal increase of the Southeast Trades is anomalously weak during the Southern Hemisphere summer, the thermocline might remain far below its normal seasonal depth.

The model response at the western boundary is much different than the eastern boundary solution (Fig. 33). Throughout most of the El Niño year, the only wave that can affect the western boundary is the low amplitude Rossby wave excited by the relaxation of the wind stress. The single exception to this statement occurs if there is a significant component of the relaxation at the western boundary, in which case the trailing edge of the Kelvin wave is initiated there. But since a Kelvin wave directly generated at a western boundary opposes the direct forcing of the wind stress, only a weak response can be generated at that boundary. The essential concepts of this situation can be seen in Fig. 3, which is the spin-up case for the linear uniform wind. Note that the response at the western boundary is much less than the initial response at the eastern boundary.

The model thermocline depth returns rapidly to near normal values after the arrival of the large amplitude Rossby wave, which was initia-

The model thermocline depth returns rapidly to near normal values after the arrival of the large amplitude Rossby wave, which was initia-ted at the eastern boundary (Fig. 33). This wave, which is responsible

for the initial downwelling along the eastern boundary, arrives at the western boundary very nearly one year after the initial relaxation of the wind stress.

The response of the model pycnocline depth at the western boundary is consistent with observations of sea level reported by Wyrtki (1979) for the 1972 and 1976 El Niño events. Wyrtki suggests that the rapid response of sea level (after a year-long decline) is caused by the intensification of the trade winds. Such a response, however, is not consistent with the linear nature of the El Niño event. McCreary (1976) showed that the relaxation phase of El Niño could be modelled by imposing an eastward wind stress to an ocean at rest. Given that the time scales of the relaxation phase and reintensification period of the wind stress are comparable (Wyrtki, 1979), the directly forced effects at the western boundary should be qualitatively similar in both cases; we should expect a slow direct response at the western boundary during the return to normal conditions as well. Hence, the rapid response at the western boundary is consistent with the effects of a large amplitude wave such as the incoming Rossby wave excited at the eastern boundary.

The large amplitude Rossby wave responsible for the downwelling also produces a dramatic effect on the interior velocity field. The wave causes the eastward current at the equator to reverse and flow strongly to the west (Fig. 32). The only observational evidence of the current field associated with El Niño is Wyrtki's indirect analysis showing that the North Equatorial Countercurrent intensified during El Niño events (particularly during the latter half of the year). It is showing that the North Equatorial Countercurrent intensified during El Niño events (particularly during the latter half of the year). It is difficult to compare the model results with this observation because the

model does not include asymmetrical boundary or forcing effects. More sophisticated modelling will be required in order to realistically compare the off-equatorial response to observations. However, an increase in the strength of the Countercurrent is not inconsistent with the effects of a first latitudinal mode Rossby wave that induces a strong westward flow at the equator. The meridional profile of the wave is such that the zonal current reverses direction between the equator and the region of the Countercurrent. During future El Niño events, current meter records from equatorial moorings should be able to record the flow reversal. This is probably the most effective way to determine whether this Rossby wave, which is of such importance to the model event, plays an important role in the real El Niño.

Finally, we examine the return to normal conditions during year 3 of the model El Niño. The strengthening of the trade winds west of 140°W induces a response which is qualitatively similar to the relaxation phase. An equatorial Kelvin wave is excited and propagates eastward. This Kelvin wave produces an upwelling response which, as before, is most intense at the eastern boundary (Figs. 33, 34). The duration of the upwelling response is shortened by the incidence of the Kelvin wave emanating from the western boundary (Figs. 31, 33). This Kelvin wave was generated by the reflection of the large amplitude Rossby wave near the end of year 4. The combined effects of the nearly simultaneous arrival of the downwelling Kelvin wave and the recently induced upwelling response tend to cancel at the eastern boundary. The remainder of the year at the eastern boundary is characterized by a gradual return ing response tend to cancel at the eastern boundary. The remainder of the year at the eastern boundary is characterized by a gradual return to normal conditions (Fig. 31).

The model El Niño event does not produce the second peak in sea level which is frequently observed during major El Niño events. Therefore, it is interesting to inquire whether a difference in the timing between the relaxation and re-strengthening phases might produce such a response. Hence, Case 2 is designed to examine the solution at the eastern boundary for an event in which the relaxed winds remain at anomalously low values for a longer period than in Case 1.

The intensification of the winds prior to the relaxation phase is identical for both Cases 1 and 2. At the start of year 4, the winds are decreased in the exact manner as Case 1, except that the relaxation takes place over a one month period instead of two months. The wind remains at low values until month 3.5 of year 5, at which time they are increased as in the standard El Niño run. Hence the difference in the duration of anomalously low winds between Cases 2 and 1 is 4.5 months. The response at the eastern boundary is shown in Fig. 37. The downwelling Kelvin wave reaches the eastern boundary prior to the upwelling event, and the double peak in pycnocline depth is observed. The second warming event is rapidly terminated by the upwelling Kelvin wave, which produces shallower thermocline depths at the eastern boundary during the remainder of the year.

The differences in the time scales of the relaxations between Cases 1 and 2 produce negligible differences in the zonal velocity field in year 4, (Figs. 38, 32). The duration of the downwelling or upwelling period is governed by the time required for a Kelvin wave to cross the anomalously forced regions, which in this case is approximately two
period is governed by the time required for a Kelvin wave to cross the anomalously forced regions, which in this case is approximately two
months. Hence, only relaxations which occur over time scales smaller

(a)

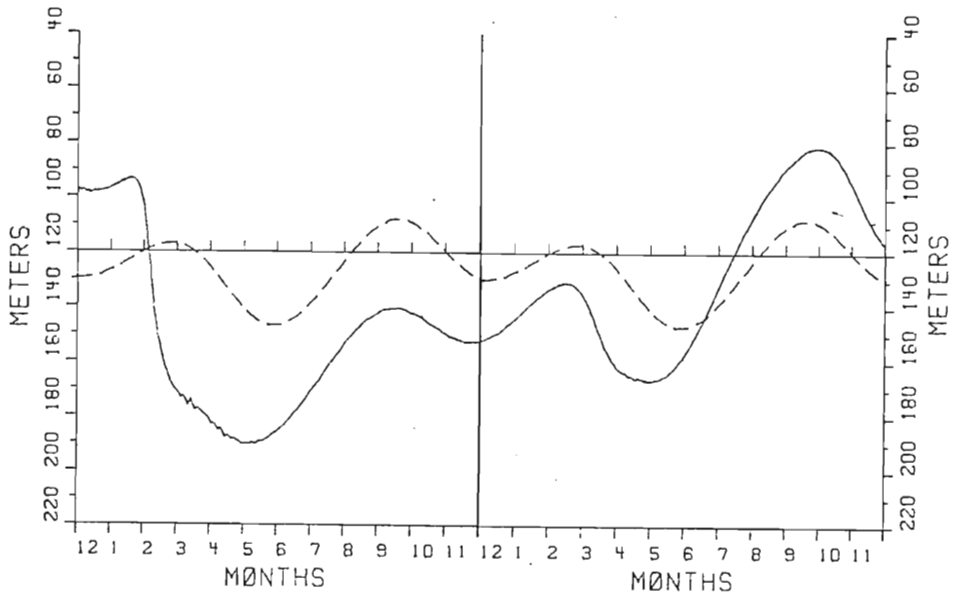

(b)

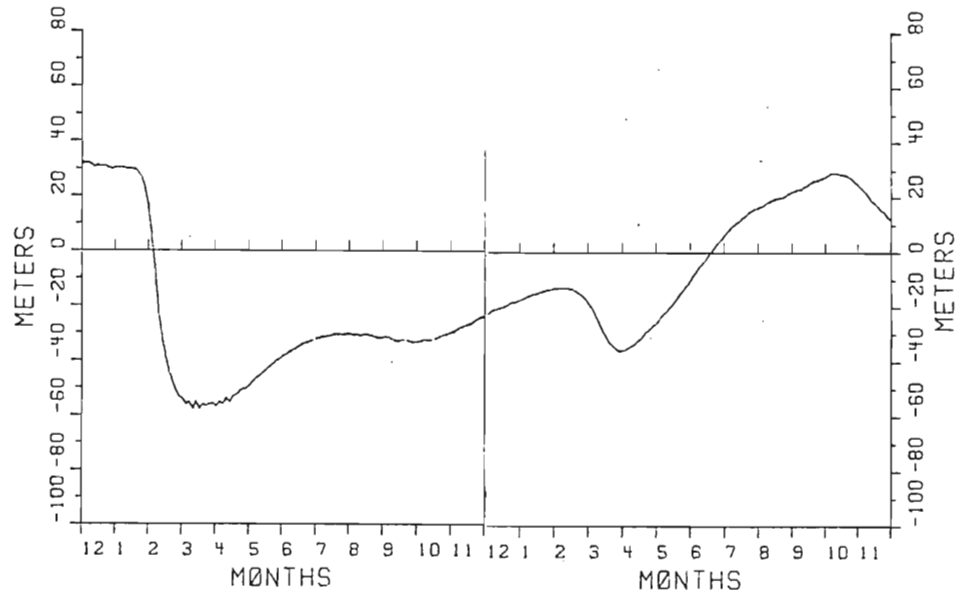

Fig. 37. (a) Time series of upper layer thickness and (b) departure of ULT from long-term seasonal value during years 4 and 5 of Case 2. The dashed line in (a) is the average seasonal solution. The relaxation of the wind is similar to Case 1 except that the time scale for the relaxation is one month. The mean wind is increased to its normal value at month 3.5 in year 5.

2. The dashed line in (a) is the average seasonal solution. The relaxation of the wind is similar to Case 1 except that the time scale for the relaxation is one month. The mean wind is increased to its normal value at month 3.5 in year 5.

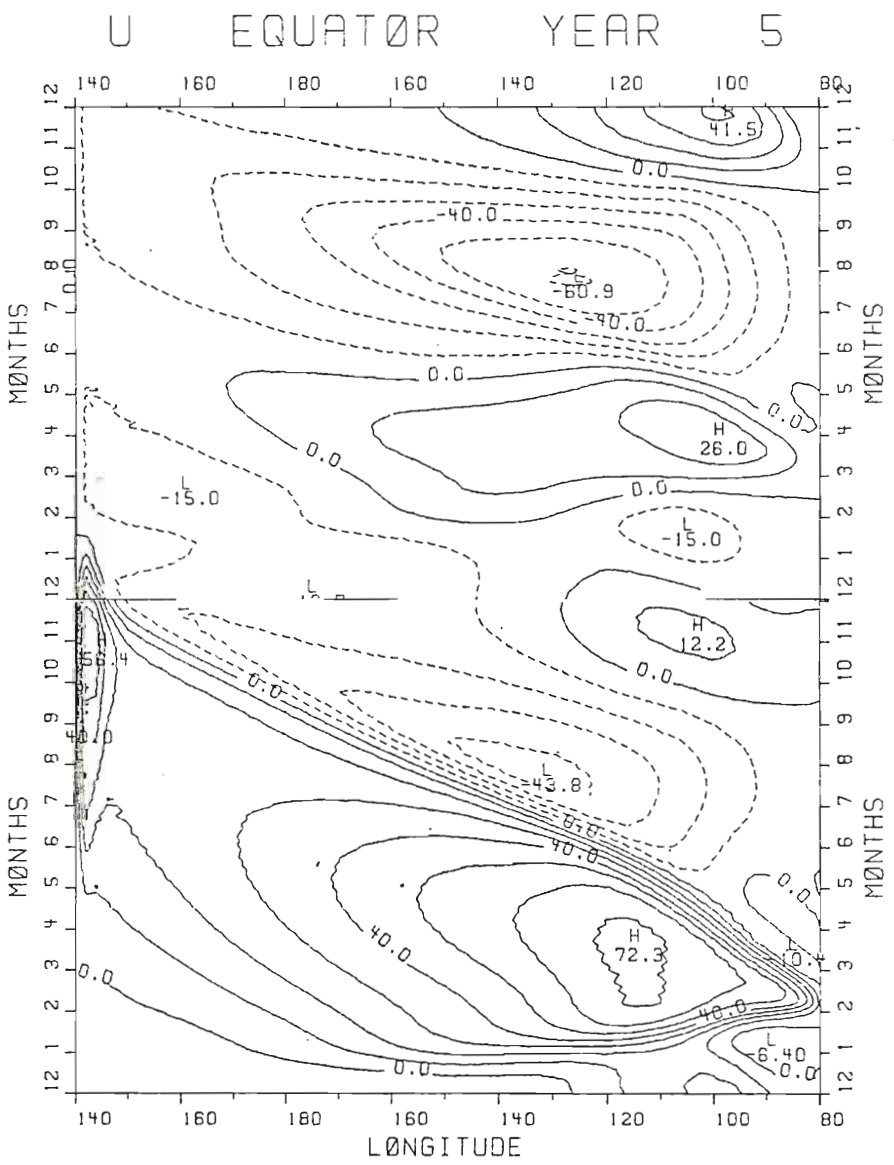

Fig. 38. The x-t section along the equator for the zonal velocity component during years 4 and 5 of Case 2. The contour interval is 10 cm sec^{-1}.

than two months will produce results similar to an instantaneous relaxation. For an event in which the winds change on a longer time scale than two months, the time scale of the relaxation is a parameter of the problem.

Case 3 is an El Niño event in which the time between the relaxation phase and the reintensification period is shorter than in Case 1. Cases 3 and 1 are identical except that the decrease of the trade winds is delayed by two months, and the relaxation of the winds take place over a one month period. The corresponding El Niño events are quickly terminated by the upwelling response induced by the re-strengthening of the wind (Fig. 39). The pycnocline rises to levels that are much shallower than the normal seasonal values. This anomalously cold period is ended by the incidence of the downwelling Kelvin wave; conditions are very quickly returned to normal values.

In Case 4, an El Niño event is examined in which there is no intensification of the wind field prior to the weakening of the trades. The magnitude of the relaxation is the same as in the standard El Niño event; hence the mean wind west of 140°W decreases linearly to zero during the first two months of year 4. The winds are maintained at these low values throughout the remainder of the model integration. Although the zonal velocity during year 4 is not as intense as in Case 1 (Figs. 32, 40a), the induced Kelvin wave front produces pycnocline depth anomalies at the eastern boundary which are larger than those found in any of the experiments (Fig. 40b). Even without the prior intensification of the wind stress, there is sufficient potential in the mean thermo-
of the experiments (Fig. 40b). Even without the prior intensification of the wind stress, there is sufficient potential in the mean thermo-
cline slope to induce a major El Niño event. This is provided, of

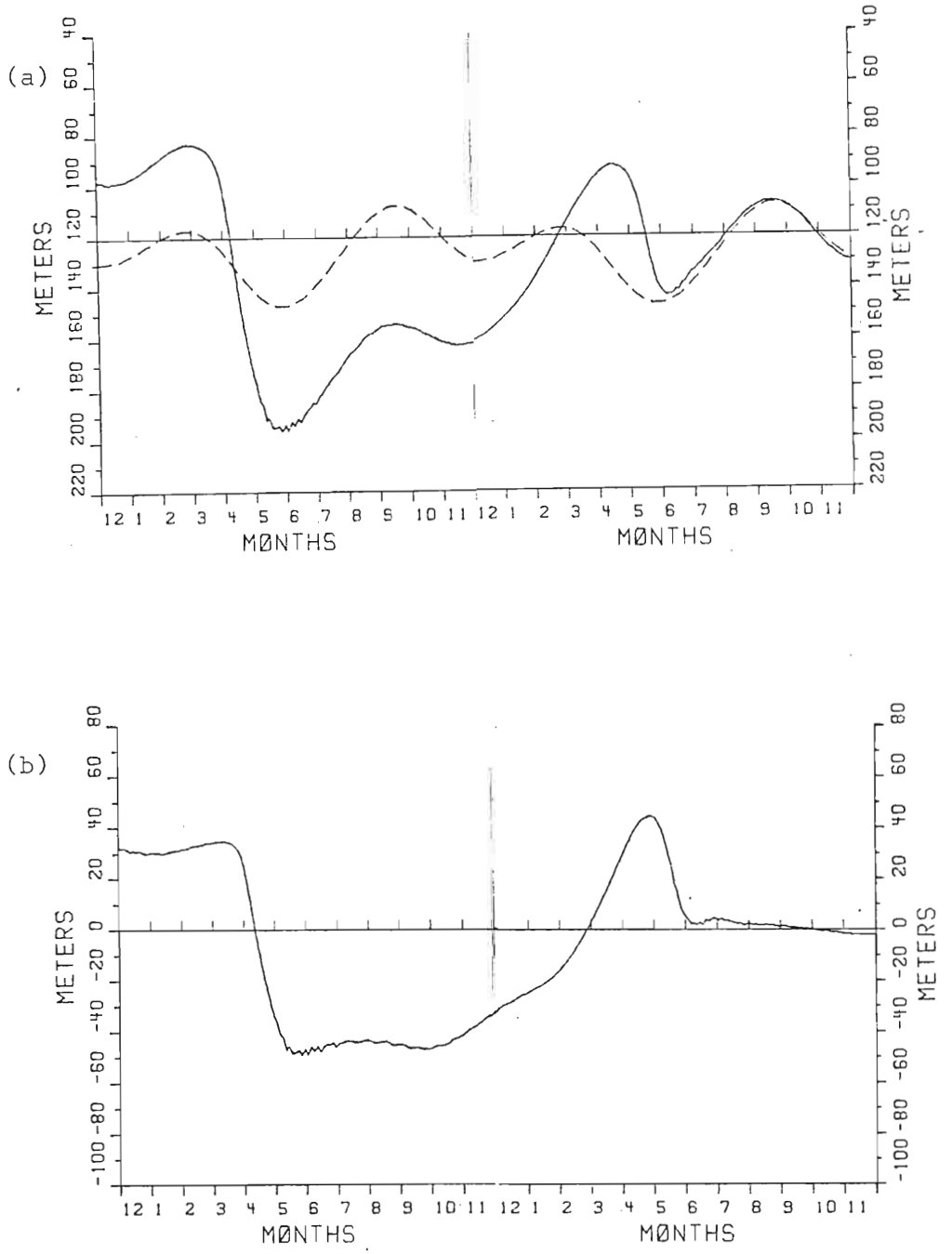

Fig. 39. Same as Fig. 37 except solution is for Case 3. The relaxation of the wind is the same as in Case 2 but delayed 2 months. The return to normal winds at the beginning of year 5 is the same as in Case 1.

relaxation of the wind is the same as in Case 2 but delayed 2 months. The return to normal winds at the beginning of year 5 is the same as in Case 1.

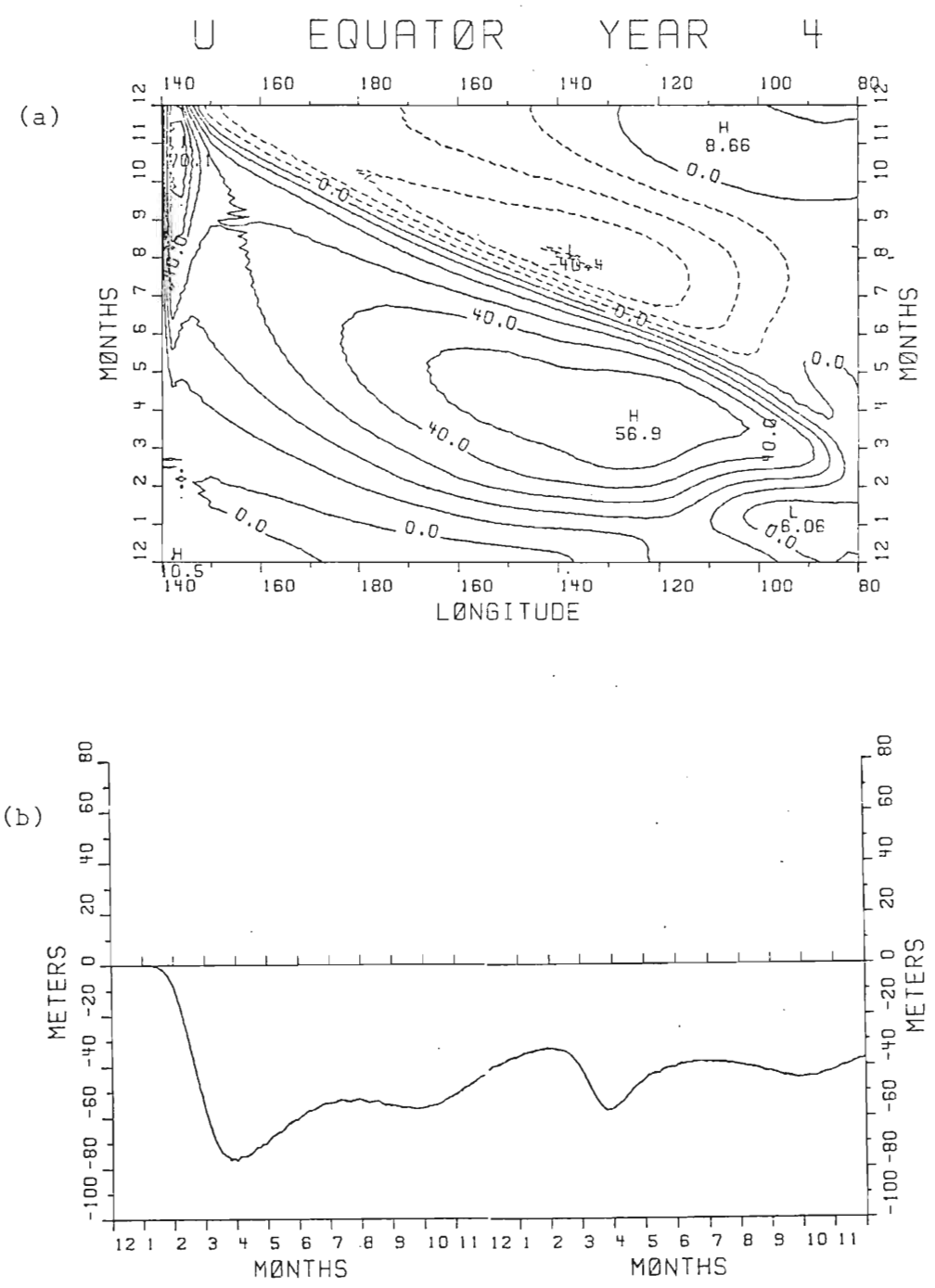

Fig. 40. (a) The x-t section along the equator for the zonal velocity component during year 4 of Case 4. The contour interval is 10 cm sec^{-1}. (b) Time series of departure of ULT from long-term seasonal solution during years 4 and 5 of Case 4. Solution is evaluated at eastern boundary.

velocity component during year 4 of Case 4. The contour interval is 10 cm sec^{-1}. (b) Time series of departure of ULT from long-term seasonal solution during years 4 and 5 of Case 4. Solution is evaluated at eastern boundary.

course, that the winds relax to much lower values than in the previous experiments.

The final case is identical to Case 1 except that the linear version of the numerical model is utilized. A comparison of Figs. 40-43 with 31-33 reveals that although the dynamics of the El Niño event are essentially linear, important modifications are induced by nonlinearities. The most important nonlinear effect is wave-dispersion which is caused both by the field acceleration term $u\frac{\partial u}{\partial x}$ amd by the variation of the layer thickness. As was observed in the numerical experiments by Hurlburt, et al. (1976), nonlinear wave dispersion causes the downwelling Kelvin wave to steepen, thereby producing a very rapid downwelling event. Also, in the linear version, the downwelling Rossby wave arrives at the western boundary around month 8 of the fourth year instead of at the end of the year (Fig. 42). Moreover, as in the seasonal simulation, the nonlinear model produces a response which more closely resembles the observations during El Niño.

The above numerical experiments provide further theoretical support for Wyrtki's hypothesis as to the initiating mechanism of El Niño, i.e., it is a remotely forced event caused by the relaxation of the equatorial trade winds in the central and western Pacific Ocean. The numerical simulations are able to account not only for the onset phase of El Niño, but also for a number of the observed longer time scale features. These include such features as the slow response of the western boundary during El Niño, the rapid return to normal conditions at the western boundary, and the mysterious occurrence of the successive El Niño events.

ing El Niño, the rapid return to normal conditions at the western boundary, and the mysterious occurrence of the successive El Niño events.

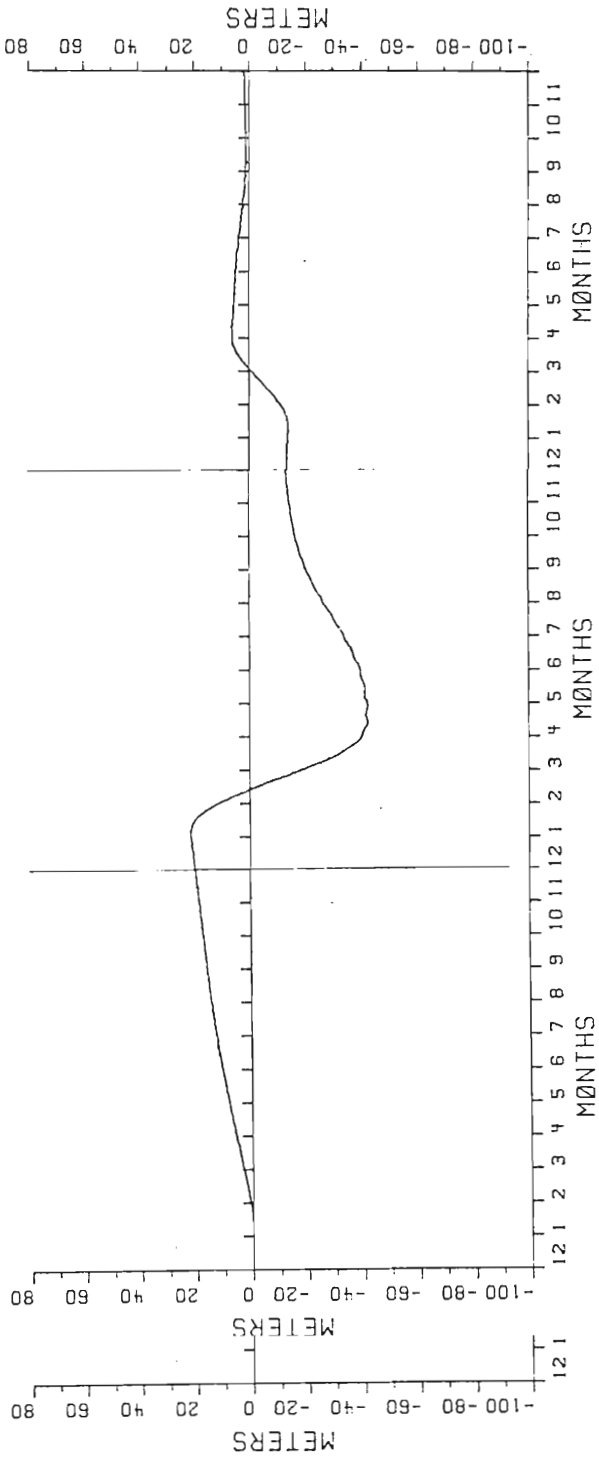

Fi Fig. 41. Time series of the departure of the ULT from the long-term linear, seasonal solutiosolution during years 3, 4 and 5 of Case 5. This solution is the linear version of Case 1 (Fig. 3(Fig. 31).

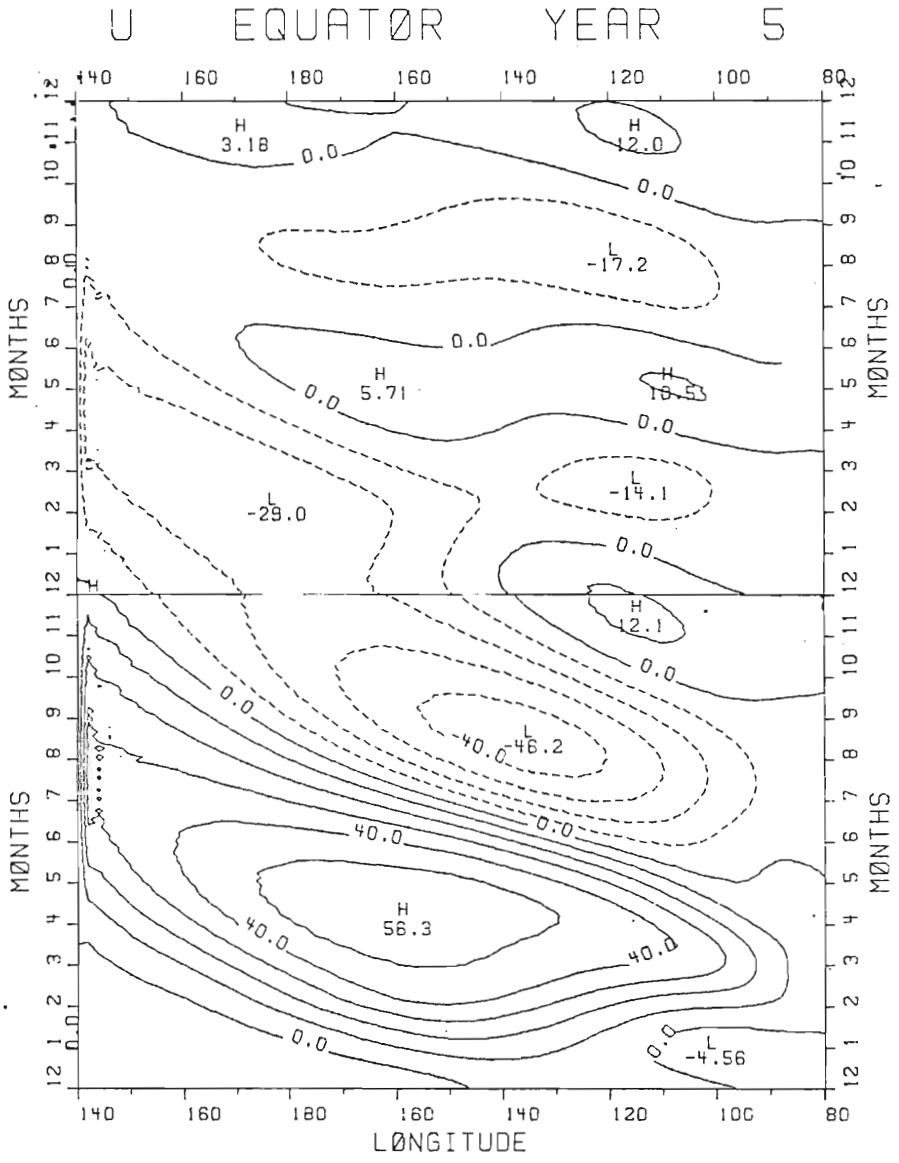

Fig. 42. Same as in Fig. 32 except for Case 5, the linear solution.

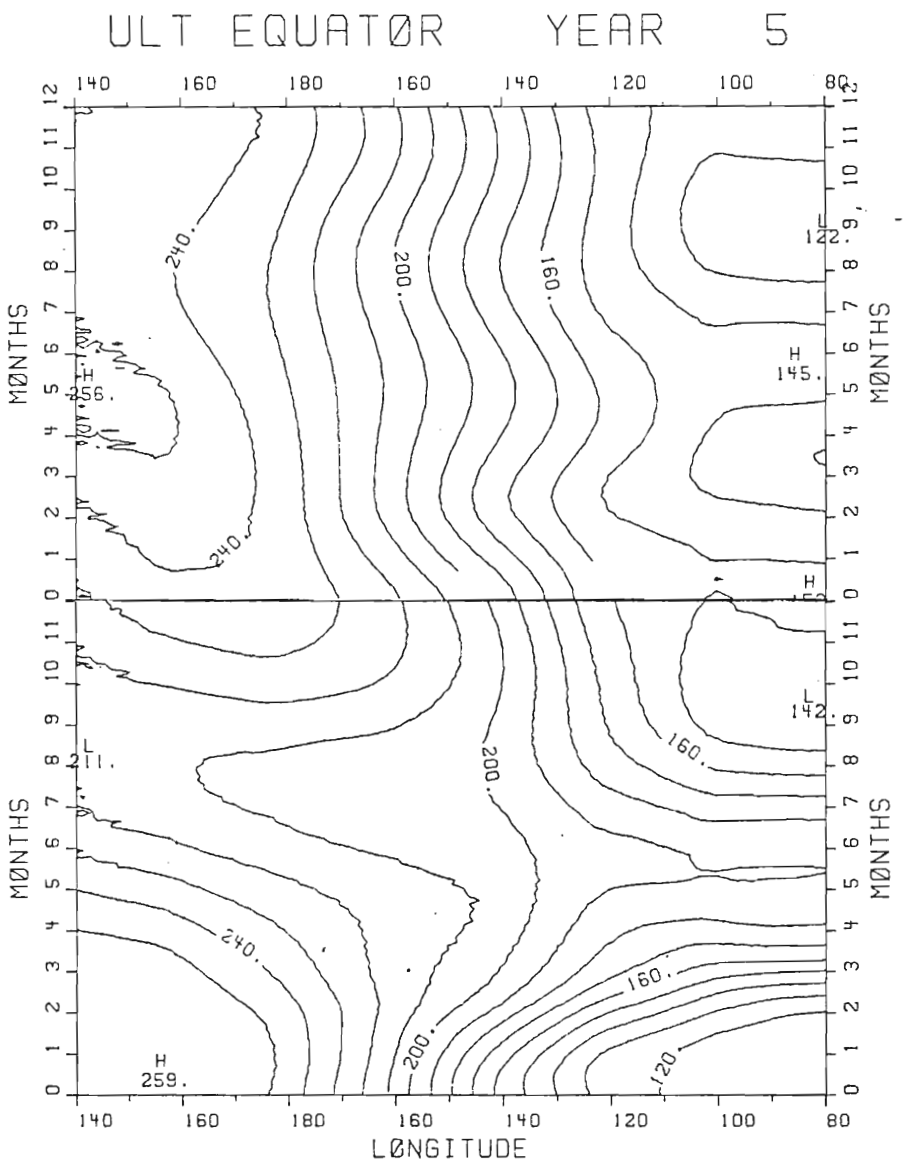

Fig. 43. Same as in Fig. 33 except for Case 5, the linear solution.

It is recognized that the model equations for this section are the simplest possible representation of the equatorial Pacific circulation which can examine equatorial wave dynamics. Future numerical simulations of El Niño should include such features as the effects of the mean current field; a more realistic boundary configuration and forcing distribution; bottom topography; thermodynamics; and thermohaline mixing. However, the essential aspects of equatorial wave dynamics will still be present in these more sophisticated modelling efforts. Hence, the dynamical scenarios of El Niño in this work are offered as an attempt to understand the fundamental physics of the El Niño event. It is hoped that they will be useful not only as an aid in the interpretation of more complicated models of El Niño but also as a starting point in the examination of the observations of this complex event.

7. SUMMARY, CONCLUSIONS AND CRITIQUE

The objective of this work was to examine the fundamental dynamics of the equatorial response to variable zonal winds whose time scales range from a few months to several years. This would allow us to examine certain aspects of the seasonal variability and the El Niño phenomenon in the equatorial Pacific. A nonlinear, reduced-gravity numerical model was used for the calculations; the rectangular model basin realistically represented the size of the tropical Pacific Ocean.

The model equations were the nonlinear, shallow water wave equations on an equatorial β-plane. Since attention was focused on the fundamental dynamics of the excitation and reflection of equatorially trapped waves, such features as the effects of the mean flow, bottom topography and a realistic meridional profile of the zonal wind stress were neglected.

Even such a simple model produced a complicated solution when it was forced by time-variable winds. Hence, as an aid in the interpretation of the numerical solutions, analytic expressions for the vertical motion of the model interface were derived. The expressions, which are applicable only along the equator, include the effects of equatorially trapped Kelvin waves, first latitudinal mode Rossby waves and the directly forced response due to a wind stress represented as a body force in the upper layer. The linear form of the numerical model was used to determine some of the unknown parameters of the analytical model,

force in the upper layer. The linear form of the numerical model was used to determine some of the unknown parameters of the analytical model,

such as the magnitudes of the generated waves and the reflection coefficients for these waves at the eastern and western boundaries. Solutions were obtained for two types of wind stress distribution: 1) a wind which is uniform across the basin and 2) a wind stress patch case in which the wind has the shape of a rectangular pulse. The advantage of deriving an expression for the latter distribution is that an arbitrary wind stress shape may be represented by a sum of these patches. No meridional variation of the wind stress was assumed. A variety of experiments were conducted in order to demonstrate the accuracy of both the linear numerical model and the analytic expressions.

Prior to examining the seasonal variability of equatorial Pacific, the analytic model was used to study certain aspects of the fundamental behavior of the equatorial response to time-variable winds. It was shown that for the uniform case, the amplitude and the phase of the response depend upon a single non-dimensional paramter. The parameter is proportional to the ratio of the length of the basin to the wavelength of the free equatorial Kelvin wave. It was also shown that, for any frequency less than the inertial, the maximum amplitude of the vertical motion of the interface occurs at the eastern boundary. The value of the parameter for which there is a maximum response was also determined.

Both the numerical and the analytical models were used to test the hypothesis of Meyers (1979b) that the large semi-annual component of the vertical motion of the thermocline in the eastern equatorial Pacific is due to the effects of remote forcing. Using Meyers' analysis of the vertical motion of the thermocline in the eastern equatorial Pacific is due to the effects of remote forcing. Using Meyers' analysis of the long-time seasonal and mean winds, the nonlinear model duplicated the

observed seasonal motion of the thermocline in the eastern equatorial Pacific. Subsequently, the analytical expressions were used to show that the semi-annual component of the thermocline motion at the eastern boundary can be caused by equatorially trapped Kelvin waves excited between 180° and 120°W.

Finally, the nonlinear numerical model was used to examine the dynamics of the El Niño event. Previous numerical simulations El Niño examined only the onset phase of the event, i.e., the first several months. These experiments supported the hypothesis of Wyrtki (1975) that El Niño is initiated by the relaxation of the wind stress in the central and western Pacific Ocean. It was generally believed that an explanation of the longer time scale observations of El Niño required the inclusion of more sophisticated dynamical mechanisms than could be included in simple first baroclinic-mode models. To test this hypothesis, the nonlinear model was initialized with the long-term seasonal solution. Subsequently, anomalous winds which are representative of the forcing during El Niño, were applied. The model integrations extended for three years in order to examine the entire El Niño event.

On the basis of the model integration it is concluded that even the longer time scale aspects of El Niño may be accounted for by the concepts of equatorial wave dynamics. The model is able to represent a number of the features observed during El Niño events.

During the onset phase of El Niño, the model thermocline in the eastern Pacific rapidly deepens by approximately 100 meters. It remains below its normal seasonal position throughout the El Niño year, although eastern Pacific rapidly deepens by approximately 100 meters. It remains below its normal seasonal position throughout the El Niño year, although a gradual return towards normal values occurs during the second half of

the year. Concurrently, the height field at the western boundary responds very slowly to the relaxation of the equatorial winds, i.e., the upper layer thickness gradually decreases throughout the El Niño year. However, at the end of the year, the thermocline deepens rapidly to its normal position. Thus, downwelling response is caused by the incidence of the gravest mode Rossby wave which was generated at the eastern boundary by the reflection of the downwelling Kelvin wave. The subsequent reflection of this large amplitude Rossby wave from the western boundary initiates a Kelvin wave which continues to propagate the downwelling response. Hence, the nature of the solution at the eastern boundary during the first half of the year following a major El Niño event depends upon the relative positions of the downwelling Kelvin wave and the upwelling Kelvin wave initiated by the re-strengthening of the trades. If the winds in the central and western Pacific remain weak for more than a year, then a second El Niño event may occur because the downwelling Kelvin wave arrives prior to the upwelling wave. However, if the duration of the anomalously weak winds is less than about one year, the eastern boundary is characterized by anomalously shallow thermocline depths. Anomalous conditions during the first half of the year following an El Niño event are terminated quickly by the arrival of either the downwelling or the upwelling Kelvin wave.

The numerical model used in these calculations is a very simple representation of the baroclinic circulation in the equatorial Pacific. The model does not include such features as the mean flow, realistic basin geometry, bottom topography, a realistic meridional profile of the wind stress, thermohaline mixing and thermodynamics. In addition, only

one vertical mode has been examined; this excludes the process by which the low order modes may be established.

The inclusion of these processes will permit the examination of several important topics which we could not address in this study. For example, it is essential to examine the effects of the mean currents (particularly, the Undercurrent) on the equatorially trapped waves. The work of McPhaden and Knox (1979) and Philander (1979b) are important initial steps toward this aim. However, numerical simulations with sufficient vertical resolution to model adequately the Undercurrent are required for a more complete study of this topic. Such models may be able to examine also the mechanisms by which the gravest baroclinic mode equatorial waves can be established. It is also important to examine the causes for the meridional asymmetries associated with the El Niño event. To what extent are the asymmetric effects governed by the shape of the basin or the distribution of the forcing? The effects of bottom topography on the reflection of equatorial waves and on the poleward-propagating coastal Kelvin waves is another topic deserving of attention. Additionally, the modifications to the equatorial waves caused by island chains which cross the equator is an interesting topic. For example, it is not known what effects the Gilbert Island chain, which extends from 3°N to 3°S at approximately 175°E, may exert on the low frequency equatorial waves examined in this study. Finally, numerical models which realistically include the effects of thermodynamics, thermohaline mixing and can predict sea surface temperatures are also very necessary.

Although the model used in the present study is a very simple one, and can predict sea surface temperatures are also very necessary.

Although the model used in the present study is a very simple one, the goal of this research was an examination of the fundamental equator-

ial dynamics associated with the effects of equatorially trapped waves excited by time-variable winds. The ability of the model to reasonably account for a number of observed time-dependent features suggests that low frequency equatorially trapped waves play a fundamental role in the dynamics of the equatorial ocean.

APPENDIX

LIST OF SYMBOLS

a	distance from the western boundary of the westernmost edge of wind-stress patch
A	horizontal eddy viscosity coefficient
C_K, C_R	speeds of Kelvin wave and the first latitudinal mode Rossby wave, respectively
d	width of wind-stress patch
g	acceleration due to gravity
g'	reduced gravity, $g(\rho_2 - \rho_1)/\rho_2$
h	upper layer thickness
h'	departure of upper layer thickness from its initial value
H	initial thickness of upper layer
H_n	equivalent depth of n-th vertical mode
k	wavenumber
L	zonal extent of model basin, same as L_x
L_x, L_y	dimensions of model basin in the zonal and meridional directions, respectively
P	pressure
P_n	amplitude of vertical mode for pressure
R_E, R_W	reflection coefficient at eastern and western boundaries, respectively
T	period, $2\pi/\omega$
	respectively
T	period, $2\pi/\omega$

T_i	period of inertial oscillation
u, v, w	zonal, meridional and vertical components of velocity
W_I	amplitude of direct interior response due to a zonal wind
W_K, W_R	amplitudes of Kelvin and Rossby waves generated at western and eastern boundaries, respectively
W_{IK}, W_{IR}	amplitudes of Kelvin and Rossby waves generated at the edges of a wind stress patch, respectively
x, y, z	tangent plane, Cartesian coordinates: x positive upward, y positive northward and z positive upward
α	dimensionless parameter given by $\omega L/C_K$
β	meridional derivative of Coriolis parameter
$\Delta\rho$	difference in density between upper and lower layers
∇_h^2	horizontal Laplacian operator
λ_n	speed of internal Kelvin wave for the n-th baroclinic mode
ω	frequency, $2\pi/T$
ϕ	phase of the vertical motion of the pycnocline with respect to the forcing
ρ_1, ρ_2	densities of upper and lower layers, respectively
τ^x, τ^y	zonal and meridional components of wind-stress, respectively

REFERENCES

Adamec, D. and J.J. O'Brien, 1978: The seasonal upwelling in the Gulf of Guinea due to remote forcing. J. Phys. Oceanogr., 8, 1050-1060.

Allen, J.S., 1975: Coastal trapped waves in a stratified ocean. J. Phys. Oceanogr., 5, 300-324.

Anderson, D.L.T. and P.B. Rowlands, 1976a: The Somali Current response to the southwest monsoon. J. Mar. Res., 34, 395-417.

Anderson, D.L.T. and P.B. Rowlands, 1976b: The role of inertia-gravity and planetary waves in the response of a tropical ocean to the incidence of a Kelvin wave on a boundary. J. Mar. Res., 34, 295-312.

Barnett, T.P., 1977: An attempt to verify some theories of El Niño. J. Phys. Oceanogr., 7, 633-647.

Barnett, T.P., 1978: The role of the oceans in the global climate system. In Climate Change, ed. by John Gribbin. Cambridge University Press.

Beer, T., 1978: Tropical waves. Geophys. and Space Phys. Rev., 16, 567-582.

Bjerknes, J., 1961: El Niño study based on analysis of ocean surface temperatures, 1935-1957. Bull. Inter-Amer. Trop. Tuna Comm., 5, 217-303.

Bjerknes, J., 1966a: Survey of El Niño 1957-58 in its relations to tropical Pacific meteorology. Bull. Inter-Amer. Trop. Tuna Comm., 12, 25-86.

Bjerknes, J., 1966b: A possible response to the atmospheric Hadley circulation to equatorial anomalies of ocean temperature. Tellus, 18, 820-829.

Bjerknes, J., 1969: Atmospheric teleconnections from the equatorial Pacific. Mon. Wea. Rev., 97, 163-172.

Pacific. Mon. Wea. Rev., 97, 163-172.

129

Bjerknes, J., 1972: Large-scale atmospheric response to the 1964-65 Pacific equatorial warming. J. Phys. Oceanogr., 2, 212-217.

Cane, M.A., 1979: The response of an equatorial ocean to simple wind stress patterns: I. Model formulation and analytic results. J. Mar. Res., 37, 233-352.

Cane, M.A., and E.S. Sarachik, 1976: Forced baroclinic ocean motions, I. The linear equatorial unbounded case. J. Mar. Res., 34, 629-665.

Cane, M.A., and E.S. Sarachik, 1977: Forced baroclinic ocean motions, II. The linear equatorial bounded case. J. Mar. Res., 35, 395-432.

Cane, M.A., and E.S. Sarachik, 1977: Forced baroclinic ocean motions, III. The linear equatorial basin case. J. Mar. Res., 37, 355-398.

Caviedes, C., 1975: El Niño 1972: Its climatic, ecological, human and economic implications. Geograph. Rev., 65, 493-509.

Cox, M.D., 1976: Equatorially trapped waves and the generation of the Somali Current. Deep Sea Res., 23, 1139-1152.

DeWitt, P.W. and A. Leetmaa, 1978: A simple Ekman-type model for predicting thermocline displacements in the tropical Pacific. J. Phys. Oceanogr., 8, 811-817.

Gill, A.E., 1975: Models of equatorial currents. Num. Models Ocean Cir., National Academy of Science, 181-203.

Gill, A.G., and A.J. Clarke, 1974: Wind-induced upwelling, coastal currents and sea-level changes. Deep-Sea Res., 21, 325-345.

Grammeltvedt, A., 1969: A survey of finite-difference schemes for the primitive equations for a barotropic fluid. Mon. Wea. Rev., 97. 384-404.

Hickey, B., 1975: The relationship between fluctuations in sea level, wind stress and sea surface temperature in the Equatorial Pacific, J. Phy. Oceanogr., 5, 460-475.

Holton, J.R., 1975: The dynamic meteorology of the stratosphere and mesosphere. Met. Monographs, 15(37).

Hurlburt, H.E., J.C. Kindle and J.J. O'Brien, 1976: A numerical simulation of the onset of El Niño. J. Phys. Oceanogr., 6, 621-631.

Hurlburt, H.E. and J.D. Thompson, 1976: A numerical model of the Somali Current. J. Phys. Oceanogr., 6, 646-664.

Hurlburt, H.E. and J.D. Thompson, 1976: A numerical model of the Somali Current. J. Phys. Oceanogr., 6, 646-664.

Ichiya, T., and J. Peterson, 1963: The anomalous rainfall of the 1957-58 winter in the equatorial central Pacific arid area. J. Meteor. Soc. Japan, 41, 172-182.

Julian, P.R. and R.M. Chervin, 1978: A study of the southern oscillation and Walker circulation phenomenon. Mon. Wea. Rev., 106, 1433-1451.

Katz, E.J., R. Belevitsch, J. Bruce, V. Budnov, J. Cochrane, W. Duing, P. Hisard, H.-V. Lass, J. Miencke, A. DeMesquita, L. Miller and A. Rybnikov, 1977: Zonal pressure gradient along the equatorial Atlantic. J. Mar. Res., 35, 293-307.

Knauss, J.A., 1964: Equatorial current systems. In: The Sea: Ideas and observations on progress in the study of the seas. Vol. 2: 235-252, Interscience, New York, 554 p.

Lighthill, M.J., 1969: Dynamic response of the Indian Ocean to the onset of the Southwest Monsoon. Phil. Trans. Roy. Soc., London, A., 265, 45-92.

Lin, L.B., and H. Hurlburt, 1978: Maximum simplification of nonlinear Somali Current dynamics. In Monsoon Dynamics, ed. by M.J. Lighthill, Cambridge University Press, Cambridge, England (in press).

Matsuno, T., 1966: Quasi-geostrophic motions in the equatorial area. J. Meteor. Soc. Japan, II, 44, 25-43.

McCreary, J.P., 1976: Eastern tropical ocean response to changing wind systems: With application to El Niño. J. Phys. Oceanogr., 6, 632-645.

McCreary, J.P., 1977: Eastern ocean response to changing wind systems. Ph.D. Dissertation, University of California, San Diego.

McKee, W.D., 1973: The wind driven equatorial circulation in a homogeneous ocean. Deep Sea Res., 20, 889-899.

McPhaden, M.J. and R.A. Knox, 1979: Equatorial Kelvin and inertia-gravity waves in zonal shear flow. J. Phys. Oceanogr., 9, 263-277.

Meyers, G., 1975: Seasonal variation in transport of the Pacific North Equatorial Current relative to the wind field. J. Phys. Oceanogr., 5, 442-449.

Meyers, G., 1979a: On the annual Rossby wave in the tropical North Pacific Ocean. J. Phys. Oceanogr., 9, 653-662.

Meyers, G., 1979a: On the annual Rossby wave in the tropical North Pacific Ocean. J. Phys. Oceanogr., 9, 653-662.

Meyers, G., 1979b: Annual variation of the slope of the 14°C isotherm along the equator in the Pacific Ocean. J. Phys. Oceanogr., 9, (in press).

Moore, D., 1968: Planetary-gravity waves in an equatorial ocean. Ph.D. Thesis, Harvard University.

Moore, D.W., and S.G.H. Philander, 1977: Modelling of the tropical oceanic circulation, The Sea, VI, ed. by E.D. Goldberg, I.N. McCave, J.J. O'Brien and J.H. Steele, 319-362, John Wiley & Sons, New York.

Moore, D.W., P. Hisard, J. McCreary, J. Merle, J.J. O'Brien, J. Picaut, J.M. Verstraete, and C. Wunsch, 1978: Equatorial adjustment in the eastern Atlantic. Geophys. Res. Let., 5, 637-640.

Namias, J., 1976: Some statistical and synoptic characteristics associated with El Niño. J. Phys. Oceanogr., 6, 130-138.

O'Brien, J.J. and H.E. Hurlburt, 1974: Equatorial jet in the Indian Ocean: Theory. Science, 184, 1075-1077.

Philander, S.G.H., 1978: Forced ocean waves. Rev. Geophys. Space Phys., 16, 15-46.

Philander, S.G.H., 1979a: Variability of the tropical oceans, to appear in Dynamics of Atmosphere and Ocean.

Philander, S.G.H., 1979b: Equatorial waves in the presence of the equatorial undercurrent. J. Phys. Oceanogr., 9, 154-162.

Quinn, W.H., 1974: Monitoring and predicting El Niño invasions. J. Appl. Meteor., 13, 825-404.

Quinn, W.H., and W. Burt, 1970: Prediction of abnormally heavy precipitation over the equatorial Pacific dry zone. J. Appl. Meteor., 9, 20-28.

Semtner, A. and Holland, 1979: Numerical simulation of the equatorial ocean circulation. Part I: A basic case in turbulent equilibrium. Submitted for publication.

Taft, B., and J. Jones, 1974: Measurements of the Equatorial Undercurrent in the eastern Pacific. Progress in Oceanography, Vol. 6, Pergamon Press, 47-110.

Tsuchiya, M., 1974: Variations of the surface geostrophic flow in the eastern intertropical Pacific Ocean. Fishing Bull., 72, 1075-1086.

Wang, D.P., 1975: Coastal trapped waves in a baroclinic ocean. J. Phys. Oceanogr., 5, 325-333.

Weare, B.C., A.R. Novato, and R.G. Newell, 1975: Empirical orthogonal analysis of Pacific sea surface temperature. J. Phys. Oceanogr., 6 671-678 —

Weare, B.C., A.R. Novato, and R.G. Newell, 1975: Empirical orthogonal analysis of Pacific sea surface temperature. J. Phys. Oceanogr., 6, 671-678.

White, W.B., 1977: Annual forcing of baroclinic Rossby waves in the tropical North Pacific Ocean. J. Phys. Oceanogr., 7, 50-61.

Wooster, W.S., and O. Guillen, 1974: Characteristics of El Niño in 1972. J. Mar. Res., 32, 387-404.

Wunsch, C., 1977: Response of an equatorial ocean to a periodic monsoon. J. Phys. Oceanogr., 7, 797-811.

Wunsch, C., and A.E. Gill, 1976: Observations of equatorially trapped waves in Pacific sea level variations. Deep Sea Res., 23, 371-390.

Wyrtki, K., 1973: Teleconnections in the equatorial Pacific. Science, 180, 66-68.

Wyrtki, K., 1974: Sea level and the seasonal fluctuations of the equatorial currents in the western Pacific Ocean. J. Phys. Oceanogr., 4, 91-103.

Wyrtki, K., 1975a: El Nino - The dynamic response of the equatorial Pacific Ocean to atmospheric forcing. J. Phys. Oceanogr., 5, 572-584.

Wyrtki, K., 1975b: Fluctuations of the dynamic topography in the Pacific Ocean. J. Phys. Oceanogr., 5, 450-459.

Wyrtki, K., 1977: Sea level during the 1972 El Niño. J. Phys. Oceanogr., 7, 779-787.

Wyrtki, K., 1979: The response of sea surface topography to the 1976 El Niño. Submitted to J. Phys. Oceanogr.

Wyrtki, K., and G. Meyers, 1976: The trade wind field over the Pacific Ocean. J. Appl. Met., 15, 698-704.

Wyrtki, K., G. Meyers, D. McClain, and W. Patzert, 1977: Variability of the thermal structure in the central equatorial Pacific Ocean, Hawaii Inst. Geophys. Rep. Hig-77-1, 32 pp., 43 figs.

Yanai, M. And T. Maruyama, 1966: Stratispheric wave disturbances propagating over the equatorial Pacific. J. Meteor. Soc. Japan., 44, 291-294.

Yoshida, K., 1959: A theory of the Cromwell Current (The Equatorial Undercurrent) and of the equatorial upwelling - An interpretation in a similarity to a coastal circulation. J. Oceanogr. Soc. Japan, 15(4), 159-170.

Zuta, S., D.B. Enfield, J. Voldivia, P. Lagos, and C. Clondin, 1974: Physical aspects of the 1972-73 El Niño phenomenon. IOC El Niño 15(4), 159-170.

Zuta, S., D.B. Enfield, J. Voldivia, P. Lagos, and C. Clondin, 1974: Physical aspects of the 1972-73 El Niño phenomenon, IOC El Niño Workshop.

VITA

John C. Kindle was born September 3, 1947 in St. Louis, Missouri. In 1969, he graduated with a B.S. in Physics from the University of Dayton. He was awarded the M.S. in Physical Oceanography from New York University in 1971. He began his graduate study in the Department of Oceanography at Florida State University in the fall of 1971.